

ASYMMETRIC POROUS MATERIALS FROM NON-EQUILIBRIUM BLOCK
COPOLYMER SELF-ASSEMBLY FOR SEPARATION, CATALYSIS, AND
ENERGY STORAGE APPLICATIONS

A Dissertation

Presented to the Faculty of the Graduate School
of Cornell University

In Partial Fulfillment of the Requirements for the Degree of
Doctor of Philosophy

by

Sarah Aline Hesse

August 2019

© 2019 Sarah Aline Hesse

ASYMMETRIC POROUS MATERIALS FROM NON-EQUILIBRIUM BLOCK
COPOLYMER SELF-ASSEMBLY FOR SEPARATION, CATALYSIS, AND
ENERGY STORAGE APPLICATIONS

Sarah Aline Hesse, Ph. D.

Cornell University 2019

Block copolymer (BCP) self-assembly (SA) thermodynamics have been used to structure-direct organic/inorganic materials into periodic mesoscopic structures with 5-100 nm length scales for applications in energy conversion and storage, catalysis, and separations. While these materials typically possess high surface areas, quick access to these surfaces remains challenging due to slow transport through the small pores. Nature has found a way to combine high surface area with fast transport by creating asymmetric structures as exemplified by the human lung. However, engineering such asymmetric structures remains difficult, as it typically requires working away from equilibrium.

The SNIPS (SA+NIPS) process combines BCP SA with an industrially-proven membrane fabrication process called non-solvent induced phase separation (NIPS). The resulting asymmetric polymeric membranes have a periodically ordered mesoporous top surface layer with high pore density and narrow pore size distribution atop a graded porous support structure with low resistance to flow – combining high selectivity with high flux. The periodically ordered top surface layer is a direct result of BCP SA. The highly permeable graded porous support structure is a direct result of the NIPS-process.

In this thesis, BCPs are used to structure-direct (in)organic nanoparticles (NPs) into asymmetric membrane structures *via* the SNIPS process. Subsequent high temperature processing results in asymmetric porous inorganic materials in the form of

oxides, nitrides, and carbons. As in conventional SNIPS derived polymer membranes, the structures have a mesoporous top surface with high pore density which merges into a porous support structure with continuous graded porosity and large macrovoids at the bottom. Furthermore, the walls of the substructure are mesoporous, providing a hierarchical pore structure and contributing to the surface area.

Chapters 2 and 3 of this dissertation explore under which conditions carbon NP precursors (phenol-formaldehyde derived resols) can successfully be structure directed *via* SNIPS and converted into graphitic carbons. Using scattering and imaging techniques, early formation stages of the resulting membranes are investigated allowing property tuning of the final asymmetric materials with respect to e.g. achievable periodic order of the pores in the top surface layer and porosity profiles of the substructure.

In chapter 4, asymmetric carbon membranes together with inorganic sol NP derived asymmetric titanium nitride (TiN) membranes are synthesized, characterized, and tested as electrochemical double-layer capacitors (EDLCs). These tests demonstrate that the asymmetric materials exhibit state-of-the-art power densities and competitive energy densities – a result of the BCP- and SNIPS-derived asymmetric membrane structures combining high surface area with fast transport of ions.

It is expected that the knowledge gained from studying these first asymmetric inorganic materials can be used to introduce other functional materials into the SNIPS process. Furthermore, first successful results of asymmetric carbon and nitride structures in an energy application suggest that asymmetry in the pore size distribution of a porous material may not only be attractive to separation applications, but may also be worth exploring in other energy storage and conversion as well as catalysis applications.

BIOGRAPHICAL SKETCH

Sarah was born in Siegen, Germany, as the first of two children of Gabriele and Bernhard Hesse. When Sarah was very young, her family moved to the San Francisco Bay Area, California, where her brother, David Maximilian, was born a few years later. Sarah's family maintained close ties to Germany and in some years even traveled up to seven times between Germany and the US. This frequent traveling has remained a welcome constant in Sarah's life.

Sarah's family was one of the first families of the German International School of Silicon Valley, a school which combines both the German and California curricula. Sarah was part of the first graduating class of nine students in 2009.

After receiving her acceptance letter from UC Berkeley, Sarah began her undergraduate studies at UC Berkeley in the Fall of 2009. Sarah entered UC Berkeley undeclared. Even in high school her interests were vast ranging from math and physics to the humanities. At some point she even considered majoring in music or the arts as Sarah always actively participated in extracurricular activities such as musical theatre, ballet and tap dancing, painting, singing, playing violin, and piano. She was given the chance to both perform in the orchestra as well as a solo artist at e.g. musical fundraising events with the motto "to Kids from Kids" to grant holiday wishes to children without parents.

However, after taking elementary chemistry courses, she decided that a B.S. in Chemistry was the major she wanted to pursue. Later on, she also decided to pursue a B.A. in German. While exempt from taking the elementary German language courses, she took many culture, literature, and linguistics courses, and finally also wrote her thesis on the "Opportunities and challenges of an international education using the German International School of Silicon Valley as an example".

It was at UC Berkeley that Sarah discovered her passion for research. What intrigued her most were labs which were interdisciplinary and bridged between fields. As an undergraduate in the College of Chemistry, Sarah conducted research in the Mechanical Engineering lab of Professor Liwei Lin under supervision of Dr. (now Professor) Ryan D. Sochol in the field of microfluidics developing a multi-stage mixing process of microbeads/cells, while enabling visualization during each fluidic step. She enjoyed the interdisciplinary nature of the research, employing engineering methods to fabricate PDMS-based microfluidic devices and using the chemistry underlying the bonding effects for the microchannels to optimize processes for biological applications.

At the same time, she completed research under supervision of Dr. Suzaynn Schick, where she studied the fundamental chemistry of smoke, engineering systems to investigate smoke in a research setting, and translating the findings into the clinical setting to probe adverse health effects of smoke on real patients.

These research opportunities sparked her interest to pursue graduate studies at a research university. In the Fall of 2013, Sarah started her graduate studies as a PhD student in Chemistry at Cornell University. After a chance encounter with Professor Ulrich Wiesner at a bus stop and subsequently talking to him about his research and group, Sarah joined the Wiesner group on October 24th, 2013 with a quick email exchange. “YES! Count me in...” was responded to with “You won’t regret it. Uli”.

It was the interdisciplinary nature of the Wiesner lab in Materials Science and Engineering that particularly sparked her interest. Scientists from various disciplines across Cornell and other universities and institutes come together and while the basis is polymer science, we delve into bioseparations, and catalysis/energy, tools for cancer imaging, etc. Her research project was centered around making polymer-derived

membranes for energy applications. This research was very different from her previous undergraduate research. However, the great mentorship of Professor Wiesner and the positive collaboration with advanced graduate student Joerg Werner helped her quickly get on her feet.

Sarah particularly enjoyed being exposed to each part of the experimental process from the project design, to the polymer synthesis and characterization, and the materials synthesis and characterization. The long and sleepless nights preparing for beamtime at the Cornell High Energy Synchrotron Source will forever be engraved in her memory, as will the countless runs back and forth between Materials Science and Chemistry. On some days she walked upwards of 30,000 steps (according to her phone) – a result of research exercise, not fitness exercise.

While her own research was more synthesis and characterization focused, Kevin Fritz of the Suntivich group, helped her take the final steps to test the performance of her materials. This really brought her research experience full-circle due the positive collaboration and also experimental outcomes. Participating in conferences and discussing research, ideas, and field leaders was also an integral part of her time at Cornell.

Apart from research, Sarah was also soon entrusted with the group's purchasing card and for many years served as the group's safety manager. She also took on the role of mentor to both undergraduate and master's students. These roles helped her grow both scientifically as well as from a leadership perspective.

While studying, after talking to Dr. Richard Walroth at one of the Chemistry Graduate and Post-doc Seminars, Sarah realized she wanted to play a more active role in the graduate and professional student community. Initially representing the Chemistry

and Chemical Biology department as a field representative in the Graduate and Professional Student Assembly, she was later elected to the executive committee, which represents the graduate and professional student voices in the context of the entirety of Cornell University. She served a year as Vice President for Communications and later served as Vice President for Operations. Sarah cherishes these experiences, not only because they were a balance to her life as a graduate student researcher and allowed her to gain further leadership experiences, but also because she met people from so many backgrounds and from various disciplines across the university.

The work in the following pages of this dissertation describes the focus of her PhD research.

Dedicated to my family, especially my mother, Gabriele, and father, Bernhard, and my brother David Maximilian. Dedicated also to my mentors, friends, and collaborators who made this work possible.

Vielen Dank!

ACKNOWLEDGMENTS

I would like to acknowledge my PhD advisor, Professor Ulrich B. Wiesner, for accepting me into his lab with the October 24th, 2013 email “You won’t regret it. Uli”, and for providing funding, research space, research guidance, and allowing me much freedom to conduct my studies.

I would also like to thank my other committee members, Professor Francis J. DiSalvo and Professor Lara A. Estroff, for helpful discussions, and in the case of Professor DiSalvo, for also allowing me to use his lab space and join his group meetings. A special thank you to Professor Phillip J. Milner for agreeing to serve as the proxy for my B exam.

A big thank you is also owed to the Wiesner group. In particular, I would like to thank Dr. Jörg G. Werner, who was my mentor when I started in the Wiesner group. I would also like to thank Dr. Kwan W. Tan, Dr. Spencer W. Robbins, Dr. Hiroaki Sai, Dr. Peter A. Beaucage, Dr. Yibei Gu, Dr. Yusuke Hibi, Dr. Ethan M. Susca, Dr. Rachel M. Dorin, Dr. Yuk Mun Li, Dr. Katharine W. Oleske, Dr. Katherine P. Barteau, Dr. Qi Zhang, R. Paxton Thedford, Fei Yu, Dana V. Chapman, Joshua A. Hinckley, Lilly Tsauro, for collaborations and discussions. I would also like to thank the undergrads I mentored: Katherine Estoque, Amar Shah, and Connor Smith.

Thank you also to my collaborators in the Suntivich group, in particular Professor Jin Suntivich, Kevin Fritz, and the master’s student I mentored, Yichen Yan.

I would also like to thank Dr. Ryo Wakabayashi, and Dr. Leilah Krounbi for their help in the DiSalvo labs.

For training and constant support with the many instruments across Cornell’s campus, I would like to thank in particular Malcolm Thomas (CCMR, SEM), Philip

Carubia (CCMR, furnaces), Dr. Mark Pfeifer (CCMR, XRD) Anthony Condo (CCMR, GPC), Dr. Arthur Woll (CHESS), and Dr. Detlef Smilgies (CHESS).

Thank you also to Dolores Dewbury and Pat Hine for always having an open ear and also helping with the administrative aspects of things.

I would also like to extend a thank you to my friends in the membrane community, in particular Professor Jamie Hestekin.

A big thank you to the friends I made through the Graduate and Professional Student Assembly, in particular Dean for Academic and Student Affairs Professor Jan Allen and Dr. Richard Walroth.

Thank you also to my neighbors at home, in particular Jim Herold, Roger Whitney, Shirley and James Mori. I also want to thank the friends I made at Cornell and in Ithaca, in particular Dr. Roselynn Cordero and Sue Hamilton.

And finally, I am and forever will be grateful to my parents, Gabriele and Bernhard, and my brother David Maximilian, and the rest of the family, for their never-ending support, encouragement, and love in this journey. You were the light and the strength that allowed me to walk this far on this journey. Thank you!

A special thank you also to the two furballs in my life, Sissi (cat) and Fiffi (dog). I feel instantly happier when you're around. Thank you for keeping me company while I wrote parts of this dissertation.

TABLE OF CONTENTS

ABSTRACT	III
BIOGRAPHICAL SKETCH	V
DEDICATION	IX
ACKNOWLEDGMENTS	X
TABLE OF CONTENTS	XII
LIST OF FIGURES	XIII
LIST OF TABLES	XXII
LIST OF ABBREVIATIONS	XXIII
CHAPTER 1	1
INTRODUCTION	1
REFERENCES	7
CHAPTER 2	12
ONE-POT SYNTHESIS OF HIERARCHICALLY MACRO- AND MESOPOROUS CARBON MATERIALS WITH GRADED POROSITY	12
<i>Abstract</i>	12
<i>Main Text</i>	13
<i>Acknowledgements</i>	23
APPENDIX A	24
<i>Detailed Experimental Procedure</i>	28
REFERENCES	30
CHAPTER 3	34
BLOCK COPOLYMER SELF-ASSEMBLY DERIVED ASYMMETRIC POROUS CARBON MATERIALS FROM NON-EQUILIBRIUM PROCESSES.....	34
<i>Abstract</i>	34
<i>Introduction</i>	35
<i>Experimental Section</i>	38
<i>Results and Discussion</i>	43
<i>Conclusions</i>	63
<i>Acknowledgements</i>	64
APPENDIX B.....	65
REFERENCES	78
CHAPTER 4	83
ASYMMETRIC PORE ARCHITECTURE IMPROVES MASS TRANSPORT AND INTERNAL AREA UTILIZATION OVER CONVENTIONAL UNIFORM PORE ARCHITECTURES.....	83
<i>Abstract</i>	83
<i>Main Text</i>	84
<i>Acknowledgements</i>	99
<i>Author Contributions</i>	100
APPENDIX C.....	101
<i>Experimental Section</i>	113
REFERENCES	126
CHAPTER 5	133
CONCLUSION	133
REFERENCES	136

LIST OF FIGURES

<p>Figure 1.1. Asymmetric structure of the human respiratory system (top row) compared to an engineered asymmetric membrane demonstrating how larger length scale structures and pores continuously evolve into smaller length scale ones (bottom row) and vice versa.4</p>	4
<p>Scheme 2.1. CGM-C fabrication process: A solution consisting of ISV and resols in a 7:3 wt% DOX:THF mixture is cast onto a glass slide, evaporated for a specific amount of time to induce a concentration gradient, and plunged into a DI water bath, which converts the concentration into a structural gradient. Resols are cross-linked at 90 °C and subsequently carbonized at 1100 °C. The BCP decomposes during carbonization leading to shrinkage of the structure and mesoporosity (right inset). 15</p>	15
<p>Figure 2.1. SEM images of an organic-polymeric hybrid membrane cast from a 12 wt% polymer and resols (2:1 wt ratio) solution and evaporated for 33 sec. (a) 30 μm sponge-like cross-section of the as-cast membrane. (b) Cross-section of the upper part at higher magnification. The top surface is shown in the inset of (b), indicating mesoporosity through the top layer. (c) Cross-sectional image of the same membrane post-90 °C cross-linking. (d) Top part of the cross-section at higher magnification. The top surface is shown in the inset, indicating a closed surface after curing of the hybrid membrane..... 16</p>	16
<p>Figure 2.2. SEM images of a graded, hierarchically porous carbon material (CGM-C) after heat-treatment at 1100 °C. (a) Full cross-section demonstrating the graded macroporosity. (b) Top surface with homogeneous mesoporosity. (c) Cross-section of the mesoporous top part of the carbon membrane at higher magnification. (d) Cross-section of the macroporous bottom part of the carbon membrane showing the hierarchical macro/mesoporosity..... 17</p>	17
<p>Figure 2.3. (a) BJH pore size distribution of the carbonized material (1100 °C) cast from a 12 wt% polymer and resols (2:1 wt ratio) solution and evaporated for 33 sec. (b-d) Characterization results of materials obtained under identical processing conditions but from 33 sec (black) and 45 sec (red) evaporation times, respectively: (b) Raman spectra for carbonized samples (1100 °C) with D- and G-bands; (c) TGA curves of these membranes; (d) SAXS curves of carbonized materials (1100 °C). 18</p>	18
<p>Figure 2.4. SEM images of the membrane cast from 12 wt% polymer and resol (2:1 wt ratio) solution evaporated for 45 sec at different processing stages. (a) 23 μm thick sponge-like cross-section of the as-cast membrane; Inset shows the top surface with mesostructural features and low porosity. (b) Cross-section of the same membrane post-90°C cross-linking. Inset shows the smooth top surface without significant structural features. (c) Cross-section of the carbonized (1100 °C) material; Insets show top surface with homogenous mesoporous features (left) and macroporous bottom part (right) demonstrating hierarchical macro/mesoporosity..... 20</p>	20
<p>Figure 2.5. (a,b) SEM images of graded, hierarchically porous carbon membranes containing Ni (a) and Pt (b) NPs (900 and 1100 °C carbonization temperatures, respectively). Insets show mesoporous parts at higher magnification with dispersed large Ni and small Pt NPs. (c) XRD data of the carbonized membranes with Ni (top) and Pt (middle) NPs. For comparison, the XRD pattern of the carbonized membrane without metal NPs is shown on the bottom. (d) TEM image of a mesoporous part of the</p>	

carbonized membrane exhibiting well-dispersed Pt NPs in the mesopores.	21
Figure S2.1. SEM images of membranes cast from 12 wt% polymer and resols (2:1 wt ratio) solutions evaporated for 33 sec and immersed in a non-solvent deionized water bath overnight. (a,b) cross section and surface structure of membrane at as-cast stage, (c,d) cross section and surface structure at the post-90 °C cross-linking stage. The membranes did not carbonize (no materials could be recovered after pyrolysis at 1100 °C), most likely because the resols were dissolved out during overnight immersion in the DI water bath.	24
Figure S2.2. SEM images of the cross-section and top surface (inset) of the neat ISV terpolymer membrane (i.e. without resols) cast from a 12 wt% ISV solution evaporated for 45 sec.	25
Figure S2.3. SEM images of the carbonized film cast from a 12 wt% polymer - resols solution (2:1 wt ratio) and completely dried for approximately 2.5 mins before immersion in water. Disordered mesoporosity without macroporosity is evident in this film.	26
Figure S2.4. Nitrogen sorption isotherms of a carbonized membrane (1100 °C) cast from a 12 wt% polymer and resol solution (2:1 wt ratio) and evaporated for 33 sec.	26
Figure S2.5. Copy of Figure 5 with labeled nickel and platinum nanoparticles.	27
Figure 3.1. Schematic Representation of Chemical Components and CNIPS Process Pathways. Typically a 2:1 weight ratio of ISV and resols in a 7:3 ratio (by weight) of DOX:THF were cast onto a glass slide. The starting solutions were prepared by either a “simultaneous” or a “consecutive method” as indicated. The solutions were evaporated for a specific amount of time to induce a concentration gradient, and plunged into a DI water bath whereby the polymer was precipitated, converting the concentration gradient into a structural gradient. The resulting asymmetric membranes were subjected to a series of heat-treatments to crosslink the resols (130 °C) and carbonize the system (900 °C). The BCP decomposes during carbonization leading to shrinkage and additional mesoporosity.	44
Figure 3.2. Small-angle x-ray scattering patterns of solutions of (a) parent ISV, (b) simultaneous method ISV+resols (2:1 ISV:resols by weight), (c) consecutive method ISV+resols (2:1 ISV:resols by weight), (d) selected pattern of consecutive method at 19 weight% ISV+resols (2:1 ISV:resols by weight). All solutions were 7:3 DOX:THF (by weight). Tick marks indicate expected peak positions for a body-centered cubic (BCC) lattice relative to the observed primary peak. The (a) ISV concentrations and (b, c, d) ISV+resols concentrations are reported with each trace.	46
Figure 3.3. Selected in situ GISAXS patterns of solutions of (a) 10 wt% ISV, (b) 10 wt% ISV+resols simultaneous method (2:1 ISV:resols by weight), (c) 10 wt% ISV+resols consecutive method (2:1 ISV:resols by weight) cast and evaporated for various times. The two images boxed in red (a) 40 s and (c) 22 s were indexed in (d) and (e), respectively. All solutions were 7:3 DOX:THF (by weight). Spot markings in (d) and (e) correspond to those expected for a SC lattice with the (001) plane parallel to the surface and lattice parameters of 38 nm and 39.5 nm, respectively.	49
Figure 3.4. SEM characterization of membranes prepared from (a) 9.9 wt% ISV, (b) 10 wt% ISV+resols (2:1 ISV:resols weight ratio) and <i>via</i> the simultaneous method, and (c) 10	

wt% ISV+resols (2:1 ISV:resols weight ratio) and *via* the consecutive method. The solutions were in 7:3 DOX:THF, cast, and evaporated for (a) 45 s on a RT (~20 °C) substrate, or (b+c) 40 s on a 30 °C substrate, respectively. All films were cast at low relative humidity (<30 %) and plunged into a RT (~20 °C) nonsolvent DI water bath. Micrographs from top to bottom respectively show top surface, cross-section, bottom surface, and a zoomed-in image from the macroporous region of the membrane. Scale bars are the same in all rows as indicated on the left. 56

Figure 3.5. Top surface (top rows) and cross-section (bottom rows) SEM characterization of (a) as-made and (c) corresponding carbonized membranes prepared via the simultaneous method from an 11 wt% ISV+resols (2:1 ISV:resols weight ratio) solution in 7:3 DOX:THF. SEM characterization of (b) as-made and (d) corresponding carbonized membranes prepared via the consecutive method from a 10 wt% ISV+resols (2:1 ISV:resols weight ratio) solution in 7:3 DOX:THF. The films were cast at the same height. However, with increased evaporation time from 20 to 40s (left to right), more solvent evaporates, producing denser and thus thinner thickness membranes. The films were cast at low relative humidity (<30 %) onto a 30 °C heated substrate, and allowed to evaporate for various amounts of time (20-40 s, as indicated) before being plunged into a RT (~20 °C) nonsolvent DI water bath. Scale is the same for all rows as indicated by scale bars on the left side. 59

Figure 3.6. Characterization of carbon materials carbonized from membranes which were obtained from 11 wt% ISV+resols (2:1 ISV:resols weight ratio) solutions in 7:3 DOX:THF prepared *via* the simultaneous method, cast onto a 30 °C heated substrate, allowed to evaporate at low relative humidity conditions (<30 %) for 40 s before being plunged into a RT (~20 °C) nonsolvent DI water bath, dried, cross-linked at 130 °C for <24 h, and carbonized. The temperature profile for the carbonizing step was first heating at a rate of 1 °C min⁻¹ to 600 °C. The temperature was held at 600 °C for 3h before being further ramped at 5 °C min⁻¹ to 900 °C, where it was held for 3 h before being allowed to cool back to room temperature. (a)-(g) Scanning electron micrographs: (a)-(c) Top surface images at different magnifications, (d) full asymmetric cross-section, (e) mesoporous middle part of cross-section, (f) higher magnification mesoporous middle part of cross-section, (g) macroporous bottom. (h) Nitrogen sorption isotherms of the carbonized material. (i) BJH derived pore size distribution of the final carbonized membrane material. 60

Figure 3.7. Characterization of carbon material carbonized from membranes which were obtained from 10 wt% ISV+resols (2:1 ISV:resols weight ratio) solutions in 7:3 DOX:THF prepared *via* the consecutive method, cast onto a 30 °C heated substrate, allowed to evaporate at low relative humidity conditions (<30 %) for 40 s before being plunged into a RT (~20 °C) nonsolvent DI water bath, dried, cross-linked at 130 °C for <24 h, and carbonized. The temperature profile for the carbonizing step was first heating at a rate of 1 °C min⁻¹ to 600 °C. The temperature was held at 600 °C for 3h before being further ramped at 5 °C min⁻¹ to 900 °C, where it was held for 3 h before being allowed to cool to room temperature. (a)-(g) Scanning electron micrographs: (a)-(c) Top surface at different magnifications, (d) full asymmetric cross-section, (e) mesoporous middle part of cross-section, (f) higher magnification mesoporous middle part of cross-section, (g) macroporous bottom. (h) Nitrogen sorption isotherms of the carbonized material. (i) BJH

derived pore size distribution of the final carbonized material. 61

Figure S3.1. Complete small-angle x-ray scattering (SAXS) patterns of solutions of (a) parent ISV, (b) simultaneous method ISV+resols (2:1 ISV:resols by weight), and (c) consecutive method ISV+resols (2:1 ISV:resols by weight). All solutions were 7:3 DOX:THF (by weight). Tick marks indicate expected peak positions for a body-centered cubic (BCC) morphology relative to the observed primary peak. The (a) ISV concentrations and (b, c) ISV+resols concentrations are reported next to each trace, ranging from about 1 wt% to 20 wt%. (d) provides a table consistent in color coding to wt% dependent traces in a-c with the corresponding d spacings, where applicable. Light gray text marks spacings given for traces which were analyzed assuming a BCC lattice but do not show evidence of BCC ordering. These values are given merely as a reference to indicate expected lattice spacings based solely off of the primary peak..... 65

Figure S3.2. Complete *in situ* GISAXS patterns of (a) 7.9 wt% and (b) 10 wt% solutions of parent ISV terpolymer in 7:3 DOX:THF solutions cast and evaporated for varying amounts of time as indicated. The two images boxed in red in (a) and (b) were indexed in (c) and (d), respectively. Patterns were indexed to an SC lattice with the (001) plane parallel to the surface and lattice parameters of 39.5 nm and 38 nm for (c) and (d), respectively..... 67

Figure S3.3. Complete *in situ* GISAXS patterns of (a) 8.0 wt%, (b) 10 wt%, (c) 12 wt%, (d) 15 wt% ISV+resols (2:1 ISV:resols weight ratio) in 7:3 DOX:THF solutions prepared *via* the simultaneous method, cast, and evaporated for varying times as indicated. Some disordered structure is evidenced by broad amorphous rings. No long-range order is evident from these diffractograms. 68

Figure S3.4. Complete *in situ* GISAXS patterns of (a) 8.0 wt%, (b) 10 wt%, (c) 13 wt%, and (d) 15 wt% ISV+resols (2:1 ISV:resols weight ratio) in 7:3 DOX:THF solutions prepared *via* the consecutive method, cast, and evaporated for varying amounts of time as indicated. The images boxed in red in (a), (b), (c), and (d) are indexed in figure S5 (a), (b), (c), and (d), respectively. 69

Figure S3.5. Selected *in situ* GISAXS patterns from Figure S4 of (a) 8.0 wt%, (b) 10 wt%, (c) 13 wt%, and (d) 15 wt% ISV+resols (2:1 ISV:resols weight ratio) in 7:3 DOX:THF solutions prepared *via* the consecutive method cast and evaporated for 31 s, 22 s, 13 s, 21 s, respectively. Patterns for (a), (b), and (c) were indexed to an SC lattice with the (001) plane parallel to the surface and lattice parameters of 40.5 nm, 39.5 nm, 39.5 nm, respectively. The pattern of the 15 wt% ISV+resols sample evaporated for 21 s was best indexed by a BCC lattice with the (110) plane parallel to the film surface and a lattice parameter of 58 nm. 70

Figure S3.6. Top surface (top row) and cross-section (bottom row) SEM characterization of 9.9 wt% ISV in 7:3 DOX:THF, evaporated on a RT (~20 °C) substrate at low relative humidity (<30%) for 30 s (left column) and 45 s (right column), and subsequently plunged into a RT (~20 °C) nonsolvent DI water bath. 71

Figure S3.7. Top surface (top rows) and cross-section (bottom rows) SEM characterization of (a) 10 wt% and (b) 15 wt% ISV+resols (2:1 ISV:resols weight ratio) in 7:3 DOX:THF solutions cast via the consecutive method on a room temperature (~20 °C) substrate under low (<30 %) relative humidity, and allowed to evaporate for various

amounts of times. The films were plunged into a RT ($\sim 20\text{ }^{\circ}\text{C}$) nonsolvent DI water bath. 71

Figure S3.8. Top surface (top rows) and cross-section (bottom rows) SEM characterization of (a) 10 wt% and (b) 15 wt% ISV+resols (2:1 ISV:resols weight ratio) in 7:3 DOX:THF solutions cast *via* the consecutive method on a substrate heated to $30\text{ }^{\circ}\text{C}$ under low ($<30\%$) relative humidity, and allowed to evaporate for various amounts of time. The films were plunged into a RT ($\sim 20\text{ }^{\circ}\text{C}$) nonsolvent DI water bath. 72

Figure S3.9. Top surface (top rows) and cross-section (bottom rows) SEM characterization of a 10 wt% ISV+resols (2:1 ISV:resols weight ratio) in 7:3 DOX:THF solution cast via the simultaneous method on (a) a RT ($\sim 20\text{ }^{\circ}\text{C}$) and (b) a substrate heated to $30\text{ }^{\circ}\text{C}$ under low ($<30\%$) relative humidity, and allowed to evaporate for various amounts of time. The films were plunged into a RT ($\sim 20\text{ }^{\circ}\text{C}$) nonsolvent DI water bath. 72

Figure S3.10. Top surface (top rows) and cross-section (bottom rows) SEM characterization of a 10 wt% ISV in 7:3 DOX:THF solution cast *via* the consecutive method under high relative humidity ($\sim 70\%$) on (a) a RT ($\sim 20\text{ }^{\circ}\text{C}$) and (b) a substrate heated to $30\text{ }^{\circ}\text{C}$, and allowed to evaporate for various amounts of time. The films were plunged into a RT ($\sim 20\text{ }^{\circ}\text{C}$) non-solvent DI water bath. 73

Figure S3.11. Top surface (top row) and cross-section (bottom row) SEM characterization of a 10 wt% ISV+resols (2:1 ISV:resols weight ratio) in 7:3 DOX:THF solution prepared *via* the consecutive method and cast at low ($<30\%$) relative humidity on a $30\text{ }^{\circ}\text{C}$ substrate and dipped into a RT ($\sim 20\text{ }^{\circ}\text{C}$) (left), a $40\text{ }^{\circ}\text{C}$ (middle), and a $4\text{ }^{\circ}\text{C}$ (right) DI water bath. 74

Figure S3.12. FFT analysis of SEM images of the top surface of the membranes for (a) ISV membrane, (b) ISV+resols (2:1 ISV:resols weight ratio) derived membrane from simultaneous method as-made (pink), or stirred in DI water overnight (green), (c) ISV+resols (2:1 ISV:resols weight ratio) derived membrane from consecutive method as-made (red), or stirred in DI water overnight (blue). Cubic ordering is only evident for ISV and ISV+resols consecutive method derived membranes. Tick marks indicate expected peak positions for a 2D square lattice. q^* positions yield pore-to-pore distances of 39 nm (black) for the ISV membrane, as well as 32 nm (red) and 40 nm (blue) for as-made membrane and a membrane stirred overnight in the DI water bath. 74

Figure S3.13. SEM characterization of (a) as-made and (b) $130\text{ }^{\circ}\text{C}$ heat-treated membranes obtained *via* the simultaneous method from an 11 wt% ISV+resols (2:1 ISV:resols weight ratio) solution. SEM characterization of (c) as-made and (d) $130\text{ }^{\circ}\text{C}$ heat treated membranes obtained *via* the consecutive method from a 10 wt% ISV+resols (2:1 ISV:resols weight ratio) solution. The evaporation time for all membranes was 40 s. From top to bottom: Top surface, cross-section, enlarged cross-section of mesoporous top surface, enlarged mesopores in the walls of the macroporous pockets towards the bottom membrane region, and bottom surface. Membranes were cast onto a $30\text{ }^{\circ}\text{C}$ substrate at low relative humidity ($<30\%$), and dipped into a RT ($\sim 20\text{ }^{\circ}\text{C}$) nonsolvent DI water bath. 75

Figure S3.14. Thermogravimetric analysis (TGA) of $130\text{ }^{\circ}\text{C}$ heat-treated ISV (red) and

ISV+resols (2:1 ISV:resols weight ratio) hybrid membranes from both the simultaneous (blue) and consecutive (green) methods. 76

Figure S3.15. Top surface (top rows) and cross-section (bottom rows) SEM characterization of (a) as-made and (b) carbonized membranes cast from 15 wt% ISV+resols (2:1 ISV:resols weight ratio) solution made *via* the consecutive method and allowed to evaporate for two different times, as indicated. Membranes were cast at low relative humidity (<30%), onto 30 °C substrates, and plunged into RT (~20 °C) nonsolvent DI water bath. 77

Figure 4.1. Asymmetric structures used for high flux/accessibility are common in nature. In this work, we utilize this concept to improve internal transport in porous materials. (a) The asymmetric structure of the respiratory system: air flows from the trachea ($\varnothing \sim 1.5$ -2.5 cm) to the bronchi ($\varnothing < 1.5$ cm) to the smaller bronchioles ($\varnothing \sim 1.0$ cm) and ends up in the alveoli ($\varnothing < 0.2$ mm). (b) The asymmetric structure of the engineered material: reactants (e.g., liquids, ions, and gases) can travel from large macropores ($\varnothing \sim 60$ μm) to smaller macropores ($\varnothing \sim 0.5$ μm), and finally to mesopores ($\varnothing \sim 10$ nm). 85

Figure 4.2. Schematic representation of SNIPS process and heat-treatment. The casting solutions, consisting of the ISV terpolymer mixed with either TiO₂ sol NPs or resols, was cast onto glass slides to form ~200-400 μm thick films. After allowing the films to partially evaporate to induce an ISV+additive concentration gradient, they were plunged into a DI water bath, precipitating the polymer and converting the concentration gradient into an asymmetric composite structure. The resulting membranes were dried at RT and 130 °C. The ISV+resols hybrids were heated to 900 °C in inert atmosphere (N₂) leading to ISV decomposition and resulting in graphitic carbon. The ISV+TiO₂ hybrids were heat-treated in air (400 °C). This led to polymer decomposition and formation of freestanding anatase titanium (IV) oxide. The oxide was then subjected to heat-treatment in ammonia (600 °C) to form TiN. A second heat-treatment in ammonia (865 °C) led to TiN superconductors. Photographs of the materials at each synthetic step are shown at the bottom. 86

Figure 4.3. Characterization of asymmetric TiN and carbon. SEM characterization of (a-g) asymmetric TiN: (a) and (b) two different types of asymmetric TiN cross-sections; (c) the top ~150 nm mesoporous part of the cross-section; (d), (e) the mesoporous top surface; (f) the bottom surface showing macropores; (g) the mesoporous wall. SEM characterization of (h-n) asymmetric carbon: (h), (i) two different types of asymmetric carbon cross-sections; (j) the top ~150 nm mesoporous part of the cross-section; (k), (l) the mesoporous top surface; (m) the bottom surface showing macropores; (n) the mesoporous wall. (o) XRD pattern of TiN. Blue tick marks indicate expected peak positions and relative intensities for cubic TiN (Fm-3m, space group # 230, ICSD #00-038-1420). (p) Nitrogen sorption isotherms of TiN (blue) and carbon (black) materials. (h) BJH derived pore size distributions of the TiN (blue) and carbon (black) materials. . 89

Figure 4.4. Electrochemical characterization of asymmetric TiN and gyroidal mesoporous TiN. Cyclic voltammograms for asymmetric TiN (blue) and mesoporous TiN (green) at (a) 50 mV s⁻¹ and (b) 5 V s⁻¹. (c) Chronoamperometry starting from the open circuit voltage to 0.01 V vs. RHE showing enhanced ion diffusion in asymmetric TiN. (d) Scan rate dependence of specific capacitance for asymmetric TiN (blue) and mesoporous TiN (green) showing improved surface accessibility for asymmetric TiN.

Error bars represent the standard deviation of three independent trials. All results were collected in Ar-saturated 0.1 M HClO₄. 93

Figure 4.5. Capacitor performance benchmark and comparison of scan-rate dependent capacitance retention. (a) Ragone plot comparing energy storage performance of gyroidal mesoporous TiN, asymmetric TiN, and asymmetric carbon. Literature examples include LaMnO_{3+δ} (◇³⁹), MnO₂ (▣⁴⁰, *⁴¹, △⁴², ◇⁴³), carbon nanotubes (⊗⁴⁴, ⊗⁴⁵), graphene (×⁴⁶, +⁴⁷), N-doped carbon (◇³), and titanium carbide (◇⁴⁸). (b) Scan rate dependence of capacitance retention for superconducting asymmetric TiN, asymmetric carbon, asymmetric TiN, and gyroidal mesoporous TiN. All results were collected in Ar-saturated 0.1 M HClO₄. 95

Figure 4.6. Characterization of asymmetric TiN superconductor. SEM characterization of: (a) ~ 50 μm thick asymmetric cross-section; (b) the mesoporous top surface part of the cross-section; (c),(d) the mesoporous top surface; (e) bottom surface with macropores; (f) mesoporous wall. (g) XRD pattern: Blue tick marks indicate expected peak positions and relative intensities for cubic TiN (ICSD #00-038-1420). (h) Temperature dependent conductivity measurements. TiN is a nitride that was exposed to air for a longer period of time than the pristine TiN. (i) Temperature-dependent magnetization from 2.2 to 5 K for superconducting TiN membrane with an onset T_c of 3.8 K. 97

Figure S4.1. Characterization *via* SEM of the cross-section, top surface, and bottom surface of the (a) As-made ISV+TiO₂ hybrid, (b) As-made ISV+resols hybrid, (c) ISV+TiO₂ hybrid treated to 130 °C, (d) ISV+resols hybrid treated to 130 °C, and (e) XRD of the 130 °C ISV+TiO₂ hybrid. 102

Figure S4.2. Characterization of asymmetric TiO₂ following heat-treatment to 400 °C in air. (a) ~60 μm cross-section SEM showing asymmetry. (b) Higher magnification SEM of the top mesoporous part of the cross-section. (c) SEM of the mesoporous top surface. (d) Higher magnification top surface SEM. (e) SEM of macroporous bottom surface. (f) Higher magnification SEM of the mesoporous wall. (g) XRD pattern of asymmetric TiO₂. Red tick marks correspond to anatase TiO₂ (I41/amd, space group #141, ICSD # 01-070-7348). (h) Nitrogen sorption isotherm. (i) BJH derived pore size distribution of asymmetric TiO₂. 103

Figure S4.3. Full characterization of the asymmetric TiN and carbon materials for which the cross-sections are shown in panels (4.3a) and (4.3h) in Figure 4.3 in the main text. (a-f) SEM characterization of the asymmetric TiN from Figure 4.3a; (a) ~60 μm asymmetric cross-section; (b) High magnification SEM of the top mesoporous part of the cross-section; (c) Mesoporous top surface. (d) Higher magnification top surface SEM; (e) Macroporous bottom surface; (f) Higher magnification SEM of the mesoporous wall. (g-l) SEM characterization of asymmetric carbon from Figure 4.3h: (g) ~8 μm asymmetric cross-section SEM; (h) Higher magnification SEM of the top ~150 nm mesoporous top part of the cross-section; (i) Mesoporous top surface; (j) Higher magnification top surface SEM; (k) Macroporous bottom surface; (l) Higher magnification SEM of the mesoporous wall. (m) XRD pattern of asymmetric TiN. Blue tick marks indicate expected peak positions and relative intensities for cubic TiN (Fm-3m, space group # 230, ICSD #00-038-1420), while red tick marks indicate tetragonal anatase anatase TiO₂ (I41/amd, space group #141, ICSD # 01-070-7348). (n) Nitrogen sorption isotherm of the asymmetric

carbon. (h) BJH derived pore size distribution of the asymmetric carbon..... 104

Figure S4.4. Characterization of BCP SA directed alternating gyroidal mesoporous TiN treated to 600 °C in ammonia. (a) Low magnification SEM of the cross-section. (b) Higher magnification SEM of the top surface. (c) High magnification SEM of the cross-section. (d) Small-angle x-ray scattering with tick marks indicating the expected peak positions for the q^{214} space group of the alternating gyroid structure. (e) XRD pattern with blue tick marks indicating expected peak positions and relative intensities for cubic TiN (ICSD #00-038-1420). (f) Nitrogen sorption isotherms. (g) BJH derived pore size distribution..... 105

Figure S4.5. Asymmetric TiN (a,c,e) and alternating gyroidal mesoporous TiN (b,d,f) cyclic voltammograms normalized by (a,b) electrode area, (c,d) electrode mass, and (e,f) surface area. All results were collected in Ar-saturated 0.1 M HClO₄ electrolyte. Scan rates shown: 1 V s⁻¹, 2 V s⁻¹, 3 V s⁻¹, 4 V s⁻¹, and 5 V s⁻¹..... 106

Figure S4.6. Scan rate dependence of gravimetric capacitance for asymmetric TiN (blue) and alternating gyroidal mesoporous TiN (green). Error bars represent the standard deviation of three independent measurements. All results were collected in Ar-saturated 0.1 M HClO₄ electrolyte. 107

Figure S4.7. Electrochemical characterization of asymmetric TiN and alternating gyroidal mesoporous TiN without iR compensation. Cyclic voltammograms for asymmetric TiN (blue) and gyroidal mesoporous TiN (green) at (a) 50 mV s⁻¹ and (b) 5 V s⁻¹. (c) Scan rate dependence of specific capacitance for asymmetric TiN (blue) and gyroidal mesoporous TiN (green) showing improved surface accessibility for asymmetric TiN. (d) Scan rate dependence of gravimetric capacitance for asymmetric TiN (blue) and gyroidal mesoporous TiN (green). Error bars represent the standard deviation of three independent measurements. All results were collected in Ar-saturated 0.1 M HClO₄ electrolyte. 108

Figure S4.8. Superconducting TiN cyclic voltammograms normalized by (a) electrode area, and (b) electrode mass. (c) Scan rate dependence of gravimetric capacitance for superconducting TiN. Error bars represent the standard deviation of three independent measurements. All results were collected in Ar-saturated 0.1 M HClO₄ electrolyte..... 109

Figure S4.9. (a) Cyclic voltammograms for asymmetric carbon at 1 V s⁻¹, 2 V s⁻¹, 3 V s⁻¹, 4 V s⁻¹, and 5 V s⁻¹. (b) Scan rate dependent gravimetric and specific capacitance for asymmetric carbon. Error bars represent the standard deviation of three independent measurements. All results were collected in Ar-saturated 0.1 M HClO₄ electrolyte..... 109

Figure S4.10. Ragone Plot normalized by (a) mass and (b) electrode area comparing alternating gyroidal mesoporous TiN (green), asymmetric TiN (blue), and asymmetric carbon (black) with select literature results..... 110

Figure S4.11. XRD patterns at various steps in the processing on the way to asymmetric TiN with superconducting properties. From bottom to top: (purple) amorphous ISV/oxide hybrid heat-treated to 130 °C. (red) Freestanding asymmetric oxide heat-treated to 400 °C in air. Red tick marks indicate the expected peak positions and relative intensities for tetragonal anatase (TiO₂) (ICSD 01-070-7348). (yellow) Freestanding asymmetric superconducting TiN heat-treated to 865 °C in ammonia. Blue tick marks indicate expected peak positions and relative intensities for cubic TiN (ICSD 00-038-

1420). 111

Figure S4.12. Photograph of bonded asymmetric TiN prior to conductivity measurement
..... 112

LIST OF TABLES

Table 3.1. Summary of in situ GISAXS pattern analysis for different solution concentrations indicating suggested BCP film surface lattices and corresponding lattice spacings.	51
Table 3.2. Summary of experiments conducted to elucidate optimized experimental conditions for obtaining ordered top surfaces in membranes cast via the S/CNIPS process.	54
Table S4.1. Surface area and pore volume of various asymmetric materials as measured via nitrogen sorption.	101
Table S4.2. Lattice parameters and crystal size results of asymmetric materials as determined <i>via</i> XRD.	101

LIST OF ABBREVIATIONS

BCP	– Block copolymer
SA	– Self-assembly
NIPS	– Non-solvent induced phase separation
SNIPS	– Self-assembly and non-solvent induced phase separation
ISV	– Poly(isoprene)- <i>block</i> -poly(styrene)- <i>block</i> -poly(4-vinylpyridine)
ISO	– Poly(isoprene)- <i>block</i> -poly(styrene)- <i>block</i> -poly(ethylene oxide)
NP	– Nanoparticle
Resols	– Phenol formaldehyde resols
TiO ₂	– Titania
TiN	– Titanium nitride
SEM	– Scanning electron microscopy
SAXS	– Small-angle x-ray scattering
GISAXS	– Grazing incidence small-angle x-ray scattering
XRD	– X-ray diffraction
FFT	– Fast Fourier transform

CHAPTER 1

INTRODUCTION

Porous nanomaterials can find a wide variety of applications from separations to catalysis to energy conversion and storage.¹⁻³ One powerful platform for creating such porous structures revolves around the thermodynamics of block copolymer (BCPs) self-assembly (SA).⁴ These BCPs consist of chemically distinct polymers or blocks which are covalently bound to one another. While usually chemically distinct polymers would form two distinct phases, leading to macrophase separation, BCPs are hindered from undergoing this process due to the covalent linkage between the blocks. Instead, they microphase separate. A high level of control can be exercised over the chain lengths, interactions, and volume fractions that dictate the size and morphology of the BCP self-assembled structures.⁴⁻⁷ In thermodynamic equilibrium, these mesoscopic, ordered structures have length scales of their periodicity on the order of 5-100 nm.⁴

While BCPs are themselves already highly versatile and functional materials, they are also chemically compatible with a host of organic and inorganic additives such as metal-oxide sol gel additives and ceramic precursors. By using the BCPs as structure-directing agents for these additives, a wide variety of mesostructured materials has been created.⁸⁻¹² In order to employ BCPs as the structure-directing agents for organic or inorganic materials, a favorable and selective interaction between the additive and one of the blocks is required in the form of e.g. hydrogen bonding. Additionally, when using nanoparticles, the radius of gyration of the nanoparticles must be smaller than the radius of gyration of the attracting block.¹³ By changing the BCPs, additives, or ratio between the two, the morphology, periodicity, and chemistry of the resulting composites can be

tuned controllably.¹⁴

After removal of the BCP, e.g. by high temperature processing, nanoporous and mesostructured functional materials can be realized. These functional materials come, for example, in the form of ceramics, metals, or transition metal oxides, dependent on the respective additives.¹⁵⁻¹⁷ In the recent work by Werner *et al.* an amphiphilic triblock terpolymer – poly(isoprene)-*block*-poly(styrene)-*block*-poly(ethylene oxide) (ISO) was used to structure direct organic phenol formaldehyde resols.¹⁸ The hydrophilic PEO block was used to mix with hydrophilic phenol formaldehyde resols. After heat-treatment of the resulting hybrid, porous gyroidal carbons were obtained. The porous mesostructured carbons were later used as one component of a three-dimensional (3D) all-solid state nanobattery.^{19,20} Robbins *et al.* used a similar ISO triblock terpolymer to structure-direct metal oxide additives.²¹ A series of heat-treatments under different environments resulted first in ordered, porous transition metal oxides and finally in nitrides, the latter of which were superconducting at low temperatures.

Nanostructured porous materials typically have high surface areas, but quickly accessing these high surface areas remains challenging due to slow transport through small pores. Looking towards nature for inspiration may help to overcome this challenge since nature has found a way of combining high surface area and fast transport by creating asymmetric structures. The human lung is one such clear example. The human cardiovascular system, and a tree's root or branch system also exemplify this concept where large diameter structures continuously evolve into small diameter structures and *vice versa*. Even though this concept of asymmetry is ubiquitous in nature, engineering such asymmetric porous structures into synthetic materials remains difficult, as it typically involves working away from the well-studied equilibrium-based structure formation

mechanisms as exemplified, *e.g.* by BCP SA.

In order to find a solution to this challenge, one area to look at is the polymer membrane field, where recently BCP SA has been combined with a process to generate asymmetric ultrafiltration membranes.²² The so-called SNIPS (SA + NIPS) process combines BCP SA with a process called non-solvent induced phase separation (NIPS).^{22–24} The NIPS process is an industrially-proven, scalable non-equilibrium process that generally results in asymmetric porous structures with a porosity gradient along the film normal and which possess low resistance to flow. However, NIPS-derived structures typically lack high selectivity due to poor control over the pore size distribution. This is where BCP SA becomes interesting. By combining BCP SA and NIPS, asymmetric structures can be created that possess a mesoporous top surface layer with high density and narrowly size-dispersed mesopores atop a highly permeable porous substructure. In this substructure pores continuously evolve along the film normal from small mesopores into macrovoids toward the membrane bottom. The BCP SA dictates the structure of the mesoporous top surface layer, which when tuned controllably, can have a high pore density and narrow pore size distribution. Thus, these engineered asymmetric porous SNIPS membranes combine both high selectivity and high flux, similar to nature's lung structure.

In the SNIPS process, a BCP solvent system consistent of typically two or three distinct solvents is cast onto a glass slide using a doctor blade. The solvents in the resulting film are allowed to evaporate. During the evaporation process, a concentration gradient develops. After a certain amount of time, the film with such a concentration gradient is plunged into a non-solvent whereby the solvent is rapidly exchanged for a non-solvent, typically water, a process which precipitates the polymer and leads to a

porous polymeric structure. The initial concentration gradient is responsible for the final asymmetric pore structure in the final membrane. While initially diblock copolymers, in particular PS-*block*-P4VP, were used, the method has since been expanded to include triblock terpolymers with improved mechanical stability.^{22–24} Subsequent studies probed the formation and performance of these membranes, and also diversified the library of BCP materials that can undergo the SNIPS process.^{25–30}

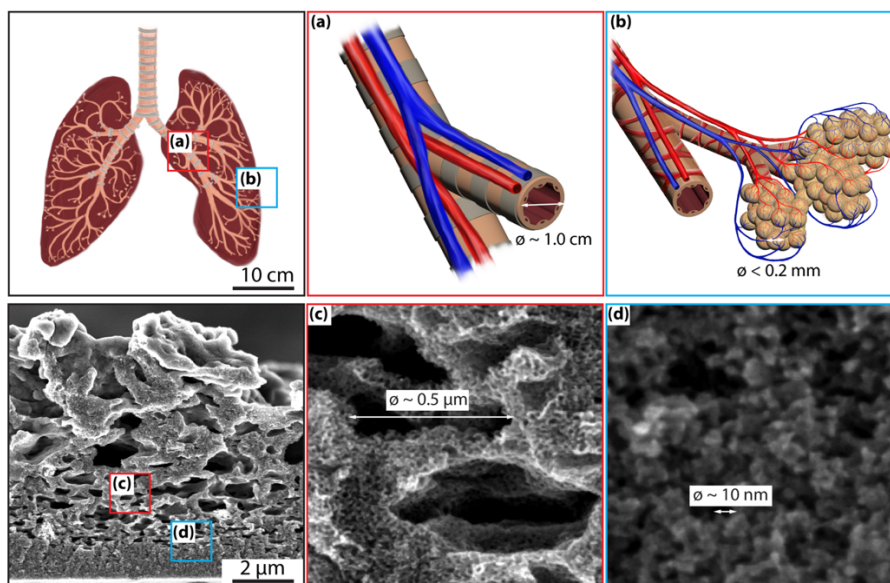


Figure 1.1. Asymmetric structure of the human respiratory system (top row) compared to an engineered asymmetric membrane demonstrating how larger length scale structures and pores continuously evolve into smaller length scale ones (bottom row) and vice versa.

The focus of this dissertation is the use of BCP SA to structure-direct organic and inorganic additives into asymmetric porous structures employing the SNIPS process. These asymmetric polymer and additive hybrid structures are subsequently heat-treated into various inorganic materials. By immediately incorporating the additives into the SNIPS process, tedious etching and backfilling procedures can be avoided. The resulting freestanding asymmetric porous inorganic structures (Figure 1.1 bottom row) exhibit a similar structural asymmetry as their polymeric SNIPS-derived counterparts. Figure 1.1 shows such an asymmetric porous inorganic membrane. The membrane is pictured

upside down from how it is obtained, *i.e.* the bottom is pointing upward and the mesoporous top surface is at the bottom, in order to depict the similarities between this asymmetric structure and the asymmetric structure of the lung. In the case of the lung (Figure 1.1 top row) large-diameter bronchi branch into smaller diameter bronchioles (Figure 1.1a), ending in high surface area alveoli (Figure 1.1b). This combines fast transport with large surface area. Similarly in the engineered system (Figure 1.1 bottom row), the macroporous support structure is highly accessible due to the large macrovoids. These macroporous voids evolve into smaller macropores (Figure 1.1c). In turn, these macropores finally evolve into mesopores (Figure 1.1d). Additionally, the walls of the macrovoids are themselves mesoporous, a structural hierarchy which contributes to large surface area (Figure 1.1c).

The second and third chapters of this thesis focus on the early formation stages of such asymmetric hybrid structures. The workhorse for these studies is a poly(isoprene)-*block*-poly(styrene)-*block*-poly(4-vinylpyridine) (ISV) triblock terpolymer which serves as the structure-directing polymer for the carbon precursor, phenol formaldehyde resols.³¹ Such carbon material are particularly interesting due to their chemical stability, high temperature resistance, conductivity, and compatibility with the BCP SA process.^{18,32-34} Scattering and imaging techniques are employed to probe under which conditions the resols can be successfully structure-directed to achieve, for example, periodic order of the pores in the membrane top surface layer. Variations in solution preparation result in different solution ordering as probed via small-angle x-ray scattering. These differences translate into different morphologies of the membrane top surfaces as exemplified *via in situ* grazing incidence small-angle x-ray scattering. Furthermore, these differences translate into different membrane top surfaces in the hybrid membranes and

final asymmetric porous structures after thermal processing. Dependent on the fabrication process, the porosity profiles of the substructure of these asymmetric membranes may also be tuned.

In the fourth chapter, asymmetric carbon and titanium nitride materials are synthesized, characterized, and finally tested as electrochemical double-layer capacitors (EDLCs). Carbon materials are the material of choice for EDLCs, although titanium nitride recently has been shown to have favorable performance.^{19,35} The titanium nitrides are also generated by using the ISV triblock terpolymer as structure-directing agent, yet instead of using organic precursors (resols) as in the case of the carbons, sol-gel derived titanium dioxide nanoparticles (NPs) are mixed in the membrane dope. It has previously been shown that hydrophilic metal oxide NPs hydrogen bond to the hydrophilic block.^{17,36,37} Subsequent heat treatment in air of the hybrid structures results in metal oxide materials which can be further treated in ammonia to result in titanium nitride, a superconductor at low temperatures. Transition metal nitrides possess high electrical conductivity, chemical stability, and low temperature superconductivity. Titanium nitride in particular has been shown to have favorable electrochemical properties. The tests performed demonstrate that the asymmetric materials exhibit state-of-the-art power densities and competitive energy densities. These properties result from the asymmetric structure of the porous materials, which combin both high surface area and fast ion transport. We expect that the advantageous properties of these materials and the tunability and scalability of the process by which they are made will allow them to find use in energy conversion and storage, catalysis, and separation applications.

REFERENCES

1. Rolison, D. R. *et al.* Multifunctional 3D nanoarchitectures for energy storage and conversion. *Chem. Soc. Rev.* **38**, 226–52 (2009).
2. Tappan, B. C., Steiner, S. A. & Luther, E. P. Nanoporous metal foams. *Angew. Chem. Int. Ed. Engl.* **49**, 4544–65 (2010).
3. Jackson, E. A. & Hillmyer, M. A. Nanoporous membranes derived from block copolymers: From drug delivery to water filtration. *ACS Nano* **4**, 3548–3553 (2010).
4. Bates, F. S. & Fredrickson, G. H. Block Copolymer Thermodynamics: Theory And Experiment. *Annu. Rev. Phys. Chem.* **41**, 525–557 (1990).
5. Floudas, G. *et al.* Poly(ethylene oxide-b-isoprene) diblock copolymer phase diagram. *Macromolecules* **34**, 2947–2957 (2001).
6. Cochran, E. W., Garcia-Cervera, C. J. & Fredrickson, G. H. Stability of the gyroid phase in diblock copolymers at strong segregation. *Macromolecules* **39**, 2449–2451 (2006).
7. Fredrickson, G. H. & Bates, F. S. Dynamics of Block Copolymers: Theory and Experiment. *Annu. Rev. Mater. Sci.* **26**, 501–550 (2003).
8. Warren, S. C., Disalvo, F. J. & Wiesner, U. Nanoparticle-tuned assembly and disassembly of mesostructured silica hybrids. *Nat. Mater.* **6**, 156–161 (2007).
9. Templin, M. *et al.* Organically modified aluminosilicate mesostructures from block

- copolymer phases. *Science (80-.)*. **278**, 1795–1798 (1997).
10. Orilall, M. C. & Wiesner, U. Block copolymer based composition and morphology control in nanostructured hybrid materials for energy conversion and storage: solar cells, batteries, and fuel cells. *Chem. Soc. Rev.* **40**, 520–535 (2011).
 11. Stefik, M., Guldin, S., Vignolini, S., Wiesner, U. & Steiner, U. Block copolymer self-assembly for nanophotonics. *Chem. Soc. Rev.* **44**, 5076–5091 (2015).
 12. Hoheisel, T. N., Hur, K. & Wiesner, U. B. Block copolymer-nanoparticle hybrid self-assembly. *Progress in Polymer Science* (2015).
doi:10.1016/j.progpolymsci.2014.10.002
 13. Warren, S. C. *et al.* Ordered mesoporous materials from metal nanoparticle-block copolymer self-assembly. *Science (80-.)*. **320**, 1748–1752 (2008).
 14. Werner, J. G., Johnson, S. S., Vijay, V. & Wiesner, U. Carbon-sulfur composites from cylindrical and gyroidal mesoporous carbons with tunable properties in lithium-sulfur batteries. *Chem. Mater.* **27**, 3349–3357 (2015).
 15. Susca, E. M. *et al.* Self-Assembled Gyroidal Mesoporous Polymer-Derived High Temperature Ceramic Monoliths. *Chem. Mater.* **28**, 2131–2137 (2016).
 16. Warren, S. C. *et al.* A silica sol-gel design strategy for nanostructured metallic materials. *Nat. Mater.* **11**, 460–467 (2012).
 17. Lee, J. *et al.* Direct access to thermally stable and highly crystalline mesoporous transition-metal oxides with uniform pores. *Nat. Mater.* **7**, 222–228 (2008).

18. Werner, J. G., Hoheisel, T. N. & Wiesner, U. Synthesis and characterization of gyroidal mesoporous carbons and carbon monoliths with tunable ultralarge pore size. *ACS Nano* **8**, 731–43 (2014).
19. Werner, J. G., Rodríguez-Calero, G. G., Abruña, H. D. & Wiesner, U. Block copolymer derived 3-D interpenetrating multifunctional gyroidal nanohybrids for electrical energy storage. *Energy Environ. Sci.* **11**, 1261–1270 (2018).
20. Werner, J. G., Rodríguez-calero, G. G., Abruña, H. D. & Wiesner, U. Block Copolymer Derived Multifunctional Gyroidal Monoliths for 3-D Electrical Energy Storage Applications. *arXiv:1706.02134 [physics.chem-ph]* (2017). doi:10.1039/C7EE03571C
21. Robbins, S. W. *et al.* Block copolymer self-assembly-directed synthesis of mesoporous gyroidal superconductors. *Sci. Adv.* **2**, (2016).
22. Peinemann, K. V., Abetz, V. & Simon, P. F. W. W. Asymmetric superstructure formed in a block copolymer via phase separation. *Nat. Mater.* **6**, 992–6 (2007).
23. Phillip, W. A. *et al.* Tuning structure and properties of graded triblock terpolymer-based mesoporous and hybrid films. *Nano Lett.* **11**, 2892–900 (2011).
24. Dorin, R. M. *et al.* Designing block copolymer architectures for targeted membrane performance. *Polymer (Guildf)*. **55**, 347–353 (2014).
25. Dorin, R. M. *et al.* Solution Small-Angle X-ray Scattering as a Screening and Predictive Tool in the Fabrication of Asymmetric Block Copolymer Membranes. *ACS Macro Lett.* **1**, 614–617 (2012).

26. Zhang, Q., Li, Y. M., Gu, Y., Dorin, R. M. & Wiesner, U. Tuning substructure and properties of supported asymmetric triblock terpolymer membranes. *Polymer (Guildf)*. **107**, 398–405 (2016).
27. Li, Y. M. *et al.* Effect of humidity on surface structure and permeation of triblock terpolymer derived SNIPS membranes. *Polymer (Guildf)*. **126**, 368–375 (2017).
28. Zhang, Q. *et al.* Dynamically Responsive Multifunctional Asymmetric Triblock Terpolymer Membranes with Intrinsic Binding Sites for Covalent Molecule Attachment. *Chem. Mater.* **28**, 3870–3876 (2016).
29. Gu, Y., Dorin, R. M., Tan, K. W., Smilgies, D. M. & Wiesner, U. In Situ Study of Evaporation-Induced Surface Structure Evolution in Asymmetric Triblock Terpolymer Membranes. *Macromolecules* **49**, 4195–4201 (2016).
30. Gu, Y., Dorin, R. M. & Wiesner, U. Asymmetric organic-inorganic hybrid membrane formation via block copolymer-nanoparticle co-assembly. *Nano Lett.* **13**, 5323–5328 (2013).
31. Hesse, S. A., Werner, J. G. & Wiesner, U. One-pot synthesis of hierarchically macro- and mesoporous carbon materials with graded porosity. *ACS Macro Lett.* **4**, 477–482 (2015).
32. Bansal, R. C., Donnet, J. B. & Stoeckli, F. *Active Carbon*. Marcel Dekker: New York (1988). doi:10.1002/jctb.280480214
33. Yang, R. T. *Adsorbents: fundamentals and applications*. Wiley-Interscience: New York (2003). doi:10.1016/S1351-4180(04)00383-6

34. Gaffney, T. R. Porous solids for air separation. *Curr. Opin. Solid State Mater. Sci.* **1**, 69–75 (1996).
35. Fritz, K. E., Beaucage, P. A., Matsuoka, F., Wiesner, U. & Suntivich, J. Mesoporous titanium and niobium nitrides as conductive and stable electrocatalyst supports in acid environments. *Chem. Commun.* **53**, 7250–7253 (2017).
36. Robbins, S. W., Sai, H., Disalvo, F. J., Gruner, S. M. & Wiesner, U. Monolithic gyroidal mesoporous mixed titanium-niobium nitrides. *ACS Nano* **8**, 8217–8223 (2014).
37. Docampo, P. *et al.* Control of solid-state dye-sensitized solar cell performance by block-copolymer-directed tio₂ synthesis. *Adv. Funct. Mater.* **20**, 1787–1796 (2010).

CHAPTER 2

ONE-POT SYNTHESIS OF HIERARCHICALLY MACRO- AND MESOPOROUS CARBON MATERIALS WITH GRADED POROSITY¹

Abstract

Hierarchically porous materials are becoming increasingly important in catalysis, separation and energy applications due to their advantageous diffusion and flux properties. Here we present the synthesis of hierarchically macro- and mesoporous carbon materials with graded porosity from a one-pot fabrication route. Organic-polymeric hybrids of a carbon precursor and poly(isoprene)-*block*-poly(styrene)-*block*-poly(4-vinylpyridine) with graded porosity are obtained *via* co-assembly and non-solvent induced phase separation. The membranes were carbonized at temperatures as high as 1100 °C with simultaneous decomposition of the block copolymer. The carbon materials show an open nanoporous top surface with narrow pore-size distribution that opens up into a graded macroporous support with increasing macropore size along the film normal and mesoporous walls, providing for highly accessible porosity with a large surface area of over 500 m²g⁻¹. Further, we expand the direct synthesis process to form well-dispersed metal nanoparticles (such as nickel and platinum) on the graded, hierarchically porous carbon materials. Our one-pot synthesis offers a facile approach to graded macro- and mesoporous carbons.

¹ Reprinted with permission from Hesse, S. A., Werner, J. G., Wiesner, U.: One-Pot Synthesis of Hierarchically Macro- and Mesoporous Carbon Materials with Graded Porosity, ACS Macro Lett. 4, 477-482 (2015). Copyright 2015 American Chemical Society.

Main Text

Mesoporous materials have been used for a wide range of applications including biomedical implants, water filtration, and energy devices, due to their high surface areas and pore volumes. In particular mesoporous inorganic materials such as carbon, metal, and metal oxide materials have been employed for energy conversion and storage applications, as well as catalysis and separation.¹⁻⁹

In order to increase the accessibility of mesoporous materials and to promote diffusion and materials flux for both gases and liquids, hierarchical meso- and macroporosity has been demonstrated to be advantageous. Furthermore, graded macroporosity featuring a continuous increase in pore size along at least one direction, can combine high material flux with good separation resolution in membrane applications.^{10,11} Graded porosity has also shown promise in minimizing mass transport resistance to either liquids or gases as well as increasing catalyst utilization and power density in fuel cell electrode materials.^{12,13}

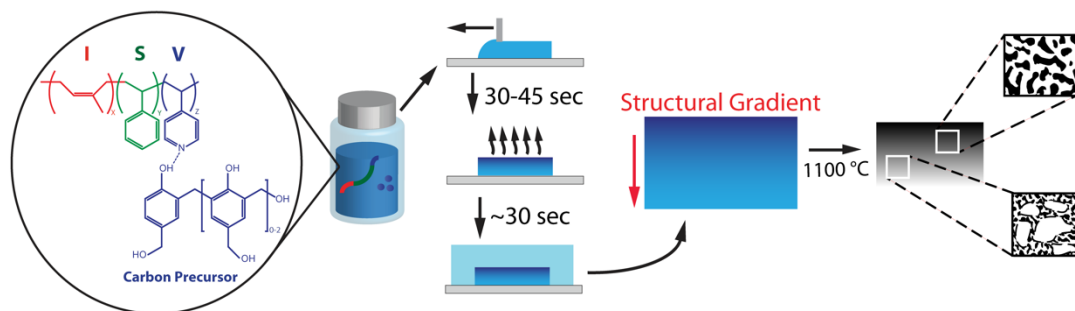
Combining the synthesis of inorganic materials with polymer fabrication techniques in soft- or hard-templating processes opens the door to facile scalability and compatibility with role-to-role processing for low-cost large area fabrication. Numerous ordered mesoporous carbons from block copolymer (BCP) soft-templating have been reported with pore sizes of below 15 nm for Pluronics templates and up to 40 nm with high molar mass BCPs. Surface areas range from 150 to 1000 m²/g, dependent on pore size, carbonization temperature and microporosity.¹⁴⁻¹⁹ Only few hierarchical macro- and mesoporous carbons have been reported using one-pot hydrothermal synthesis or spinodal decomposition.^{20,21} Recently, BCPs have been used for the fabrication of graded, hierarchically macro- and mesoporous polymer membranes with ordered features on the

nanoscale *via* the self-assembly and non-solvent induced phase separation (SNIPS) process.^{10,11,22-24} These SNIPS casted polymeric membranes have been utilized as sacrificial polymeric hard-templates for the synthesis of carbon, metal, and metal oxide materials with graded macro- and mesoporosity (Cornell Graded Materials: CGM), however, hard-templating approaches are often lengthy and tedious.²⁵ Here, we demonstrate the first direct one-pot synthesis of graded macro- and mesoporous carbon material (CGM-C).

The CGM-Cs exhibit an open nanoporous surface with narrow pore size distribution on top of a macroporous substructure with graded macroporosity toward the bottom. The macroporous carbon substructure consists of mesoporous walls. This hierarchical porosity leads to easily accessible high surface area of over 500 m² g⁻¹, which is within the typically observed range for mesoporous carbons.¹⁶ Furthermore, we expand the process to form well-dispersed metal nanoparticles (NPs) such as nickel and platinum on the CGM-C.

CGM-Cs were obtained using co-assembly and non-solvent induced phase separation of poly(isoprene)-*block*-poly(styrene)-*block*-poly(4-vinylpyridine) (ISV) and phenol-formaldehyde resols. The ISV terpolymer employed here had a molar mass of 103 kg/mol, a polydispersity index (PDI) of 1.11, and weight fractions of 25%, 57%, and 18% for poly(isoprene) (PI), poly(styrene) (PS) and poly(4-vinylpyridine) (P4VP), respectively.¹⁰ Phenol-formaldehyde resols with a molar mass of less than 500 g/mol were used as thermally cross-linkable carbon precursor.¹⁹

ISV terpolymer and carbon precursor were dissolved (2:1 by weight) in a 1,4 dioxane (DOX) to tetrahydrofuran (THF) mixture (7:3 by weight) as an overall



Scheme 2.1. CGM-C fabrication process: A solution consisting of ISV and resols in a 7:3 wt% DOX:THF mixture is cast onto a glass slide, evaporated for a specific amount of time to induce a concentration gradient, and plunged into a DI water bath, which converts the concentration into a structural gradient. Resols are cross-linked at 90 °C and subsequently carbonized at 1100 °C. The BCP decomposes during carbonization leading to shrinkage of the structure and mesoporosity (right inset).

12 wt% solution (8 wt% with respect to the ISV polymer).

Terpolymer composition and casting conditions were based on our experience with SNIPS-derived ISV membranes and optimized for this system.^{10,22–24} The carbon precursors increase the viscosity of the casting solution, allowing a lower polymer concentration as compared to pure ISV-membrane formation using SNIPS.¹⁰ Hydrophilic carbon precursors attach to the P4VP block *via* hydrogen bonding to the nitrogen of the pyridine ring.^{26,27} The homogeneous solution was cast on glass slides using a doctor blade. After partial evaporation of the solvents for a specific time (*i.e.* 33 sec) inducing a concentration gradient along the film-normal direction, films were plunged into a water bath for non-solvent induced phase separation (NIPS, Scheme 2.1). Precipitation of the glassy PS block induced increasing macroporosity along the concentration gradient from the top to the bottom of the membranes. Short time periods of membranes in the non-solvent water bath (<30 sec) avoided excessive dissolution of the water-soluble phenol-formaldehyde resols. Longer time periods caused the resols to dissipate from the

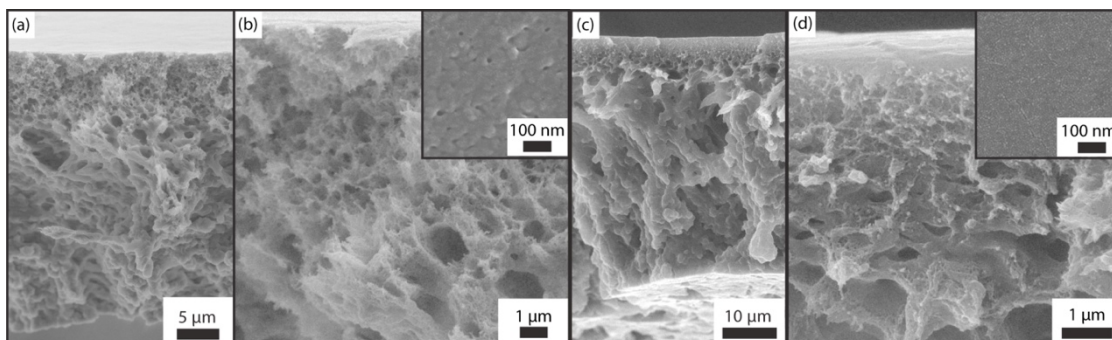


Figure 2.1. SEM images of an organic-polymeric hybrid membrane cast from a 12 wt% polymer and resols (2:1 wt ratio) solution and evaporated for 33 sec. (a) 30 μm sponge-like cross-section of the as-cast membrane. (b) Cross-section of the upper part at higher magnification. The top surface is shown in the inset of (b), indicating mesoporosity through the top layer. (c) Cross-sectional image of the same membrane post-90 $^{\circ}\text{C}$ cross-linking. (d) Top part of the cross-section at higher magnification. The top surface is shown in the inset, indicating a closed surface after curing of the hybrid membrane.

membranes, thereby significantly decreasing the carbon yield during the carbonization process. As such, immersing membranes in a water bath overnight yielded membrane structures similar to the ones described here, but did not allow for carbonization (Figure S2.1). The ISV-resols hybrid membranes were subsequently dried, and further cured at 90 $^{\circ}\text{C}$. The curing step (cross-linking of the resols) is essential to provide a stable structure upon carbonization.

Figure 2.1a shows the 30 μm thick cross-section of a dried ISV-resols membrane with graded macroporosity. A few microns thick mesoporous layer (enlarged in Figure 2.1b) sits on top of a macroporous support layer with increasing macropore size from top to bottom. For comparison, Figure S2.2 provides a cross-sectional and top surface SEM image of a pure ISV-membrane (*i.e.* without resols) cast from a 12 wt% ISV solution and evaporated for 45 sec. The organic-polymeric hybrid and neat ISV terpolymer membranes exhibit similar cross-sectional structures. The top surface of the as-cast hybrid, however, shows only some degree of mesoporosity without order (inset in

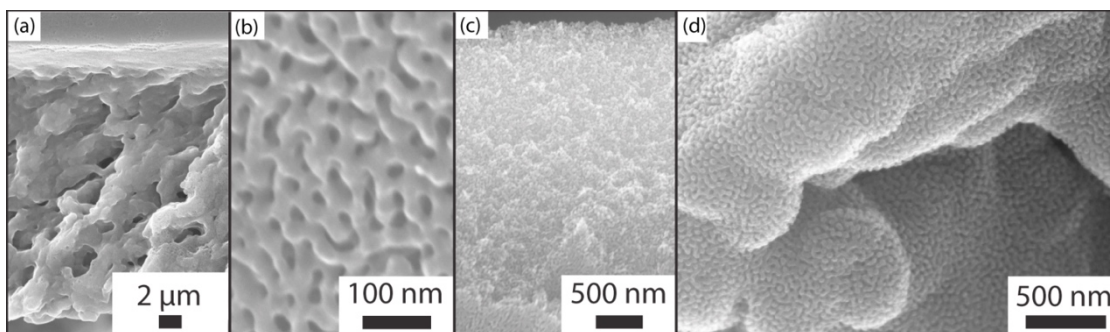


Figure 2.2. SEM images of a graded, hierarchically porous carbon material (CGM-C) after heat-treatment at 1100 °C. (a) Full cross-section demonstrating the graded macroporosity. (b) Top surface with homogeneous mesoporosity. (c) Cross-section of the mesoporous top part of the carbon membrane at higher magnification. (d) Cross-section of the macroporous bottom part of the carbon membrane showing the hierarchical macro/mesoporosity.

Figure 2.1b), very different to the square packing of mesopores in the neat ISV terpolymer membrane. After curing of the resols at 90 °C the structure remains asymmetric and porous (Figure 2.1c+d). However, the walls of the cured hybrid appear to be smoother, and the top surface of the film exhibits no porosity (Figure 2.1d). We speculate that this is due to the mobility of the resols and polymer at the elevated temperature that causes a decrease in surface roughness during curing.

The cured organic-polymeric hybrid membranes were carbonized at 1100 °C under inert atmosphere (nitrogen flow). The phenol-formaldehyde resols further condense and carbonize at higher temperatures (>600 °C) while the triblock terpolymer decomposes, thereby forming graded carbon materials with hierarchical porosity (CGM-C, Figure 2.2). The overall structure is well maintained despite significant shrinkage of the membranes during carbonization that is due to the considerable amount of ISV terpolymer that decomposes between 300 and 400 °C (Figure 2.3c). Carbonized materials are more fragile than the as-cast and post-90 °C membranes, but maintain their

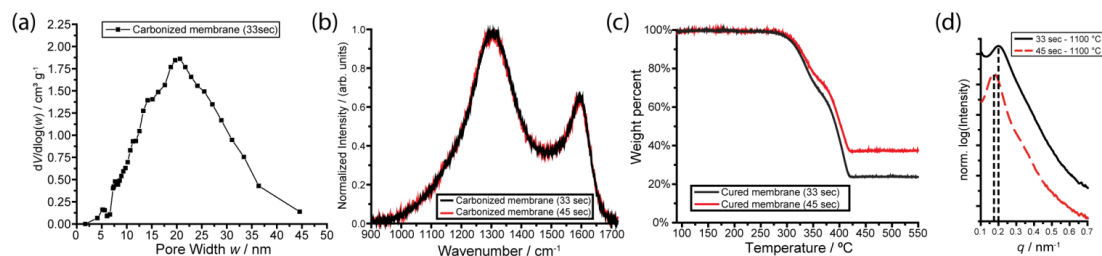


Figure 2.3. (a) BJH pore size distribution of the carbonized material (1100 °C) cast from a 12 wt% polymer and resols (2:1 wt ratio) solution and evaporated for 33 sec. (b-d) Characterization results of materials obtained under identical processing conditions but from 33 sec (black) and 45 sec (red) evaporation times, respectively: (b) Raman spectra for carbonized samples (1100 °C) with D- and G-bands; (c) TGA curves of these membranes; (d) SAXS curves of carbonized materials (1100 °C).

monolithic shape. The cross-section in Figure 2.2a of a carbonized membrane shows graded macroporosity with a 2-3 μm thick mesoporous layer (enlarged in Figure 2.2c) on top of a 20 μm macroporous substructure. The top surface of the carbonized membrane shows network-like mesoporosity with homogenous pore sizes of about 12-14 nm (Figure 2.2b). An important feature of this carbonized material is that the walls of the macropores are in turn mesoporous (Figure 2.2d), constituting the structural hierarchy with simultaneous macropore gradation from top to bottom. Analysis of the nitrogen adsorption isotherm (Figure S2.4) according to the Brunauer-Emmett-Teller (BET) theory yielded a surface area of $547 \text{ m}^2\text{g}^{-1}$.²⁸ The nitrogen sorption isotherms show a typical type-IV curve with H_1 -type hysteresis and sharp capillary condensations above relative pressures of 0.9, with a total mesopore volume of $1.0 \text{ cm}^3 \text{ g}^{-1}$ calculated at a relative pressure of 0.99. The BJH pore size distribution (Figure 2.3a) peaks at 20 nm with a full-width at half-maximum (FWHM) of 19 nm.²⁹

Raman spectra from the graded, hierarchically porous membranes carbonized at 1100 °C corroborate the formation of disordered carbon materials (Figure 2.3b). The typical D-band and G-band appear at 1306 cm^{-1} and 1590 cm^{-1} , respectively.^{30,31} To

illustrate the effects of the non-solvent induced phase separation and the microphase separation of the ISV triblock terpolymer, we also casted a film that was completely dried (evaporation at room temperature for over 2.5 minutes) before immersion in the water bath. Figure S2.3 provides SEM images of the fully dried film after carbonization, cast from the same ISV-resols solution described above. The 15 micron thick carbon film exhibited a disordered, mesoporous network-structure without macroporosity. The dried and cured films did not show any porosity (data not shown). This suggests that the formation of the graded hierarchical porosity is due to the NIPS process, while ISV decomposition of the microphase separated ISV-resols composite most likely contributes to the mesoporosity of the final membranes.

In order to investigate the effect of evaporation time on membrane structure, another membrane was cast from the same solution as above but with a 45 sec evaporation time before plunging into the non-solvent bath. Figure 2.3b provides thermogravimetric analysis (TGA) data of the cured membranes with evaporation times of 33 and 45 sec in black and red, respectively. Both curves show the same qualitative shape, with the onset temperature for terpolymer decomposition at 300 °C and full decomposition at 420 °C. The phenol-formaldehyde resin left at the final temperature comprised 20 wt% and 35 wt% of the original hybrid in the case of 33 and 45 sec evaporation time, respectively. We speculate that the higher ISV-resols concentration after longer evaporation time results in better retention of the resols during the non-solvent plunge, thereby allowing for a higher yield during carbonization. No difference in graphitization was observable from Raman spectroscopy between the two CGM-Cs obtained from different evaporation times (Figure 2.3b).

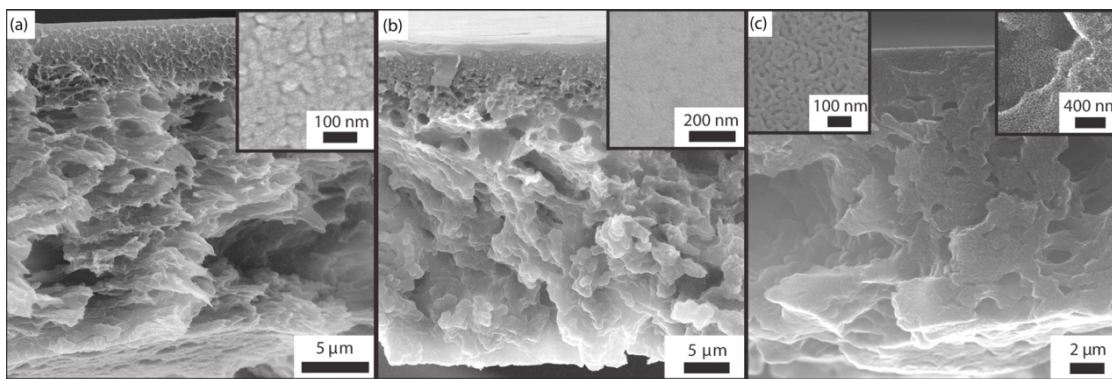


Figure 2.4. SEM images of the membrane cast from 12 wt% polymer and resol (2:1 wt ratio) solution evaporated for 45 sec at different processing stages. (a) 23 μm thick sponge-like cross-section of the as-cast membrane; Inset shows the top surface with mesostructural features and low porosity. (b) Cross-section of the same membrane post-90°C cross-linking. Inset shows the smooth top surface without significant structural features. (c) Cross-section of the carbonized (1100 °C) material; Insets show top surface with homogenous mesoporous features (left) and macroporous bottom part (right) demonstrating hierarchical macro/mesoporosity.

Small-angle X-ray scattering (SAXS) traces of the carbonized membranes

(1100 °C) reveal correlation lengths of the disordered mesostructure of 32 nm and 36 nm for evaporation times of 33 and 45 sec, respectively (Figure 2.3c). This result is consistent with the TGA data, as longer evaporation times allow more resols to be incorporated in the membrane, which causes less shrinkage during pyrolysis. Membranes before carbonization did not show any peaks in SAXS (data not shown), most likely due to the low electron density contrast between the phases in the ISV-resols hybrids.

Figure 2.4 depicts SEM images of a membrane that was cast with an evaporation time of 45 sec. While the membrane appears denser (e.g. see 23 μm thick cross-section in Figure 2.4a), the overall features of the membrane are similar to those after only 33 sec evaporation time shown in Figure 2.1. This is expected as the increased evaporation time causes a decrease of solvent content at the time of NIPS. The top surface and cross-sectional structural features evolve in a similar way during curing at 90 °C (Figure 2.4b) and

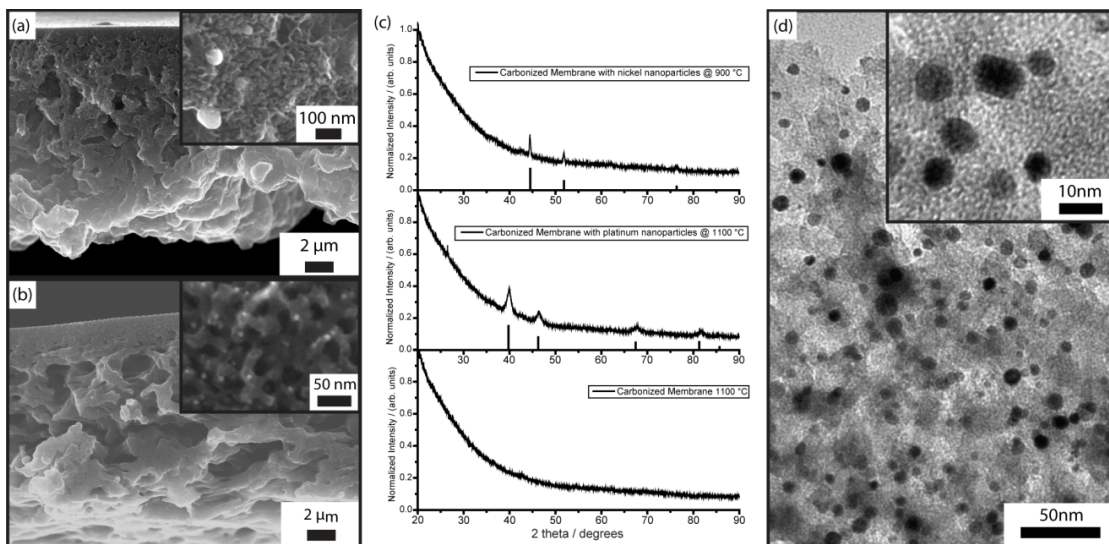


Figure 2.5. (a,b) SEM images of graded, hierarchically porous carbon membranes containing Ni (a) and Pt (b) NPs (900 and 1100 °C carbonization temperatures, respectively). Insets show mesoporous parts at higher magnification with dispersed large Ni and small Pt NPs. (c) XRD data of the carbonized membranes with Ni (top) and Pt (middle) NPs. For comparison, the XRD pattern of the carbonized membrane without metal NPs is shown on the bottom. (d) TEM image of a mesoporous part of the carbonized membrane exhibiting well-dispersed Pt NPs in the mesopores.

carbonization at 1100 °C (Figure 2.4c) as described above for the membrane with shorter evaporation time. Longer evaporation time leads to a smaller top surface mesopore size of only about 8-10 nm, however (left inset of Figure 2.4c).

In order to further show the versatility of our approach and to increase functionality, we incorporated metal NPs into CGM-Cs. To that end, in addition to terpolymer and carbon precursor, membranes were cast from solutions containing (1,5-cyclooctadiene) dimethyl platinum(II) or bis(cyclopentadienyl) nickel(II) (1:4 or 1:10 ratio to resols by weight, respectively) for the synthesis of well-dispersed platinum or nickel NPs, respectively (Pt/Ni-NPs-on-CGM-C). The metal precursors got reduced during the heat-treatment under inert gas and formed well-dispersed metal NPs on the carbon walls throughout the entire hierarchically porous carbon membrane. Figure 2.5 shows SEM images of the graded NP-on-CGM-Cs after pyrolysis, together with the

corresponding X-ray diffraction patterns (XRD). A marked Figure 2.5 indicating the exact positions of nickel and platinum nanoparticles can be found in the Supporting Information (Figure S52.). The cross-section of Ni-NP-on-CGM-C after carbonization at 900 °C shows graded macroporosity, very similar to the neat carbon membranes. Large nickel NPs with diameters of 50-70 nm are well dispersed in the mesoporous parts of the carbon material (Figure 2.5a inset). The corresponding XRD pattern shows the expected peaks for *fcc* nickel (top of Figure 2.5c, PDF-card 01-073-6826). The average domain size of 40 nm was approximated using the Scherrer equation on the (111), (200), and (220) peaks. The cross-section of Pt-NPs-on-CGM-C is shown in Figure 2.5b. Small NPs are well dispersed on the mesoporous walls (Figure 2.5b inset) throughout the membrane without disrupting the membrane morphology. The broad peaks in the corresponding XRD pattern (middle panel in Figure 2.5c) corroborate formation of small platinum crystallites (PDF-card 01-087-0646) with an average domain size of 3 nm, approximated using the Scherrer equation for the first four peaks. The transmission electron microscopy (TEM) micrograph in Figure 2.5d shows small platinum NPs with diameters ranging from 6 nm to 10 nm well dispersed in the mesoporous parts of the carbonized membrane. The different mean dimensions, as evident from XRD and TEM analysis, indicate the presence of multi-domain NPs. The incorporation of metal NPs was achieved with almost no alteration to the protocol despite the inclusion of a soluble metal precursor to the initial casting solution, demonstrating the versatility of the synthesis protocol.

In conclusion, we reported on a facile one-pot synthesis method to create hierarchically macro- and mesoporous carbon materials with graded porosity (CGM-C). These membranes with a typical thickness of tens of microns possess a nanoporous top

surface with narrow pore size distribution on top of a graded macroporous support structure that in turn exhibits mesoporous walls. This allows for highly accessible porosity with large surface areas. Furthermore, we demonstrated that the direct synthesis can conveniently be expanded to include metal precursors for the fabrication of graded, hierarchically porous carbon structures with well-dispersed metal NPs. Due to the advantageous structural and porosity features we expect that these carbon structures will find use in a variety of applications including energy conversion and storage, catalysis and separation.

Acknowledgements

This project was funded by the National Science Foundation (DMR-1409105). The work made further use of the Cornell Center for Materials Research Shared Facilities, which are supported through the NSF MRSEC program (DMR-1120296). The authors thank Prof. Sol Gruner (Cornell University) for his kind assistance with SAXS measurements.

APPENDIX A

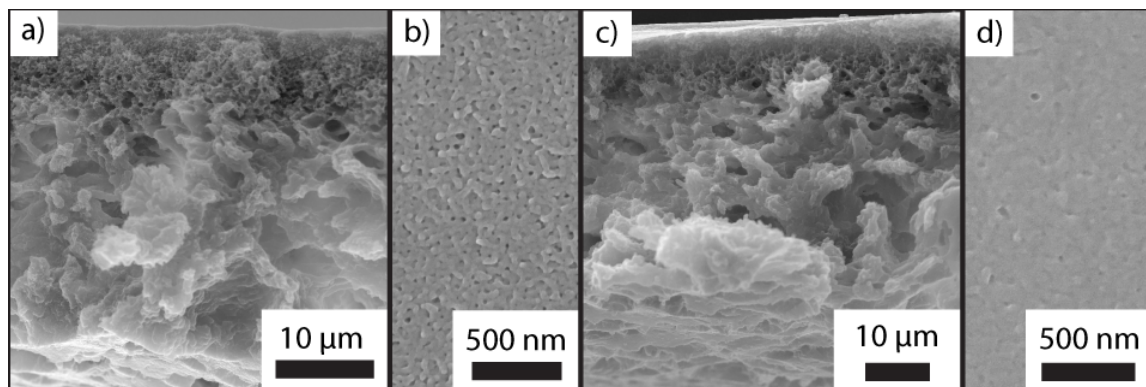


Figure S2.1: SEM images of membranes cast from 12 wt% polymer and resols (2:1 wt ratio) solutions evaporated for 33 sec and immersed in a non-solvent deionized water bath overnight. (a,b) cross section and surface structure of membrane at as-cast stage, (c,d) cross section and surface structure at the post-90 °C cross-linking stage. The membranes did not carbonize (no materials could be recovered after pyrolysis at 1100 °C), most likely because the resols were dissolved out during overnight immersion in the DI water bath.

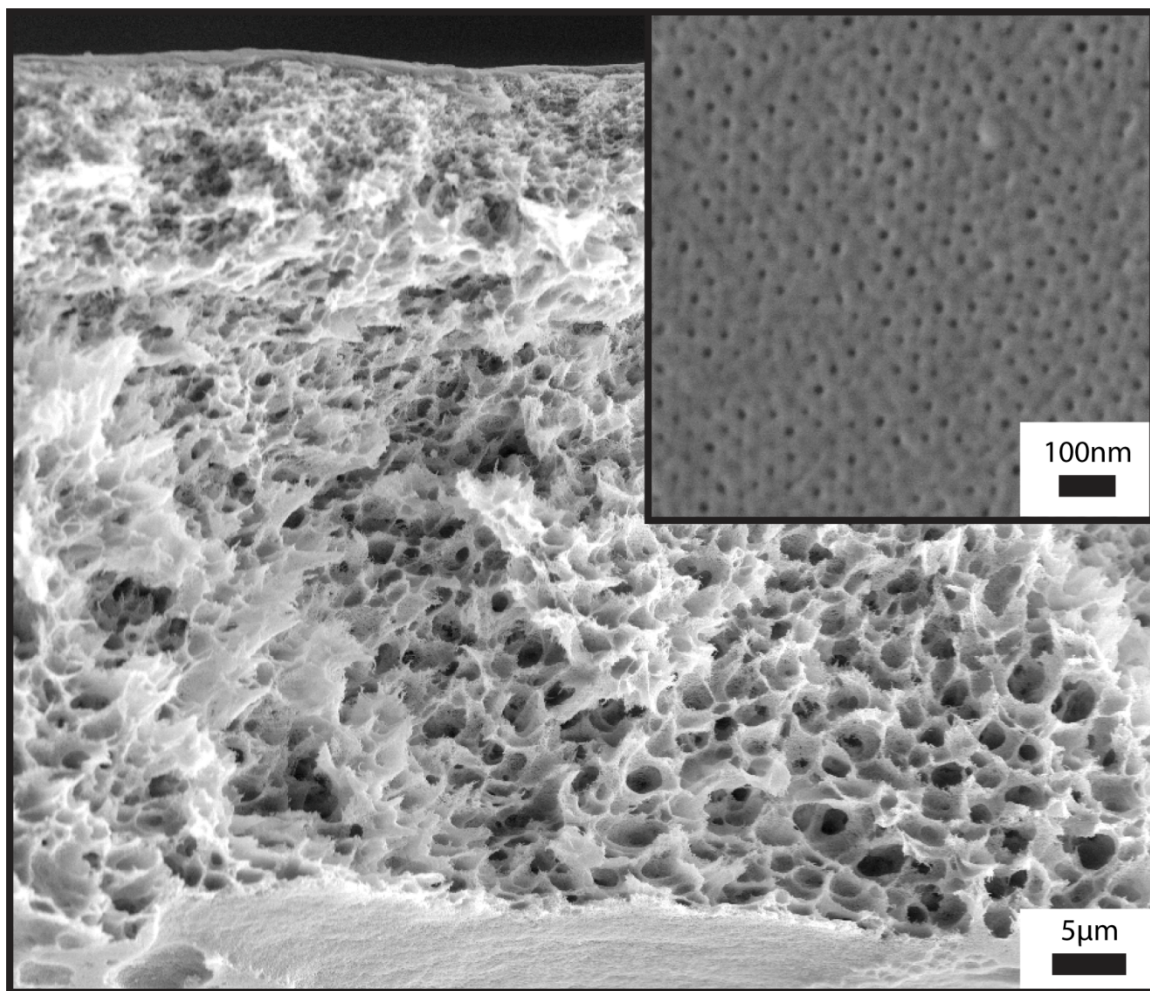


Figure S2.2. SEM images of the cross-section and top surface (inset) of the neat ISV terpolymer membrane (i.e. without resols) cast from a 12 wt% ISV solution evaporated for 45 sec.

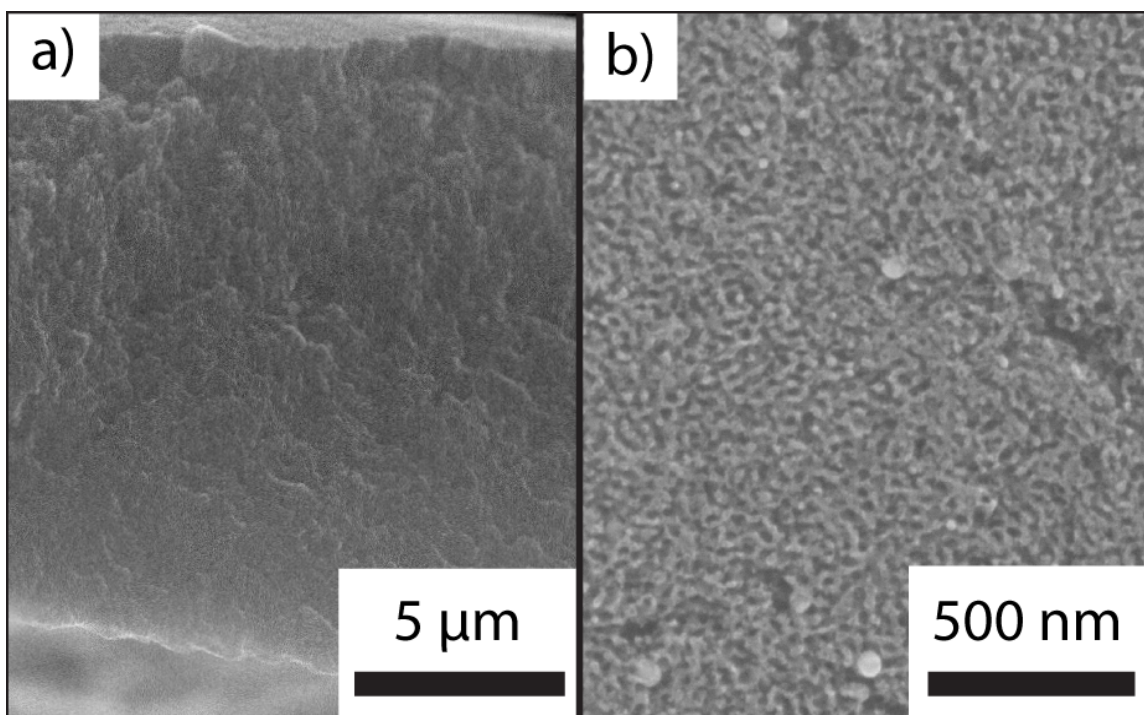


Figure S2.3: SEM images of the carbonized film cast from a 12 wt% polymer - resols solution (2:1 wt ratio) and completely dried for approximately 2.5 mins before immersion in water. Disordered mesoporosity without macroporosity is evident in this film.

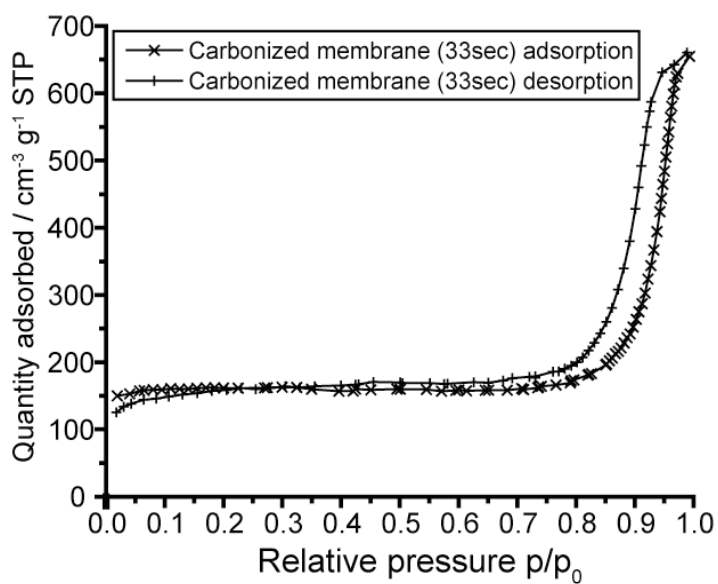


Figure S2.4. Nitrogen sorption isotherms of a carbonized membrane (1100 °C) cast from a 12 wt% polymer and resols solution (2:1 wt ratio) and evaporated for 33 sec.

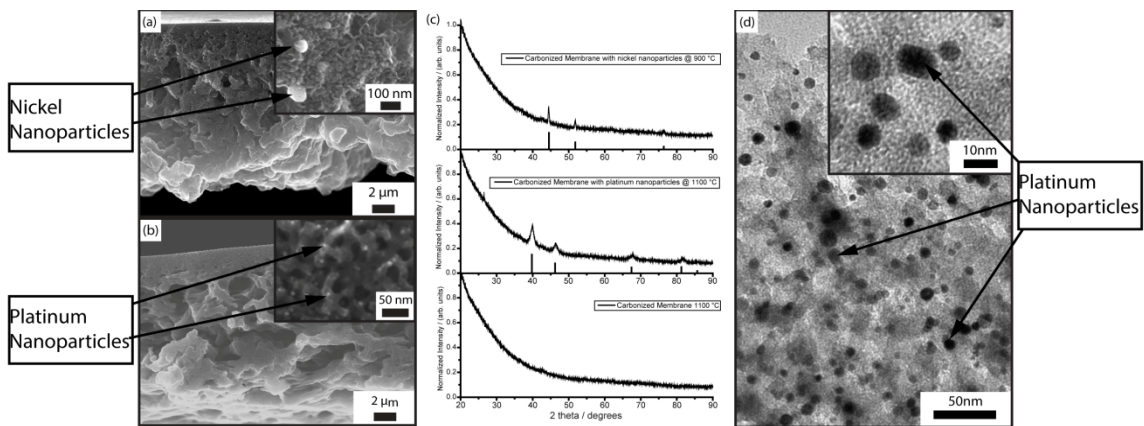


Figure S2.5. Copy of Figure 5 with labeled nickel and platinum nanoparticles.

Detailed Experimental Procedure

Synthesis. The Poly(isoprene)-*block*-poly(styrene)-*block*-poly(4-vinylpyridine) (ISV) triblock terpolymer was synthesized *via* sequential anionic polymerization, as has previously been described.¹⁰ The polymer had an overall molar mass of 103 kg mol⁻¹, a polydispersity index of 1.11, and weight fractions of 25%, 57%, and 18% for poly(isoprene) (PI), poly(styrene) (PS) and poly(4-vinylpyridine) (P4VP), respectively.

Phenol-formaldehyde resols were synthesized with a molar mass of <500 g mol⁻¹ *via* the well-known polymerization of phenol and formaldehyde under basic conditions as previously described.¹⁹ Briefly, phenol, formaldehyde, and sodium hydroxide were combined at 45 °C in a molar ratio of 1:2:0.1 and polymerized at 75 °C. After neutralizing with *para*-toluene sulfonic acid, the resols solution was freeze-dried, dissolved in a 1:1 wt mixture of tetrahydrofuran (THF) and chloroform as a 25 wt% solution and filtered to remove precipitated sodium *para*-toluene sulfonate. The resols were freeze dried again and dissolved as a 25 wt% solution in THF or dioxane (DOX).

Film casting. For the casting solution, ISV and resols were dissolved as a 12 wt% solution with a 2:1 ISV to resols weight ratio, in a 7:3 (by volume) mixture of 1,4-dioxane (DOX) and tetrahydrofuran (THF). The solutions were stirred overnight to dissolve the polymer and subsequently left without stirring for about 2 hours to allow for gas bubbles to dissipate. For the synthesis of nickel nanoparticles on graded, hierarchically porous carbon, bis(cyclopentadienyl) nickel(II) was added to a 14 wt% ISV-resols solution that was stirred over night, with a 1:10 weight ratio of nickel precursor to resols and stirred for two more hours. For the synthesis of platinum nanoparticles on graded, hierarchically porous carbon, (1,5-cyclooctadiene) dimethyl platinum(II) was added to a 12 wt% ISV-resols solution that was stirred over night, with a 1:4 weight ratio of platinum precursor to resols and stirred for three more hours.

To create the organic-polymeric hybrid membranes, the solutions were cast onto a glass slide using a doctor blade (Testing Machines, Inc., K Control Coater) with a gate height of 229-254 μm . Part of the solvent was allowed to evaporate for 33 or 45 sec (see text), followed by plunging the film into the non-solvent bath (deionized water). After about 30 sec, the phase-separated hybrid membrane was removed from the water bath. All membranes were cast at humidity ranging between 40-50%.

Carbonization. The membranes were dried, placed onto graphoil, and heated in

a convection oven to crosslink the resols. The temperature profile was 50 °C for 12 hours, followed by 90 °C for 5 days. The hybrids were carbonized by further heating under inert atmosphere (nitrogen) at 1 °C min⁻¹ to 600 °C for 3 h, then at 5 °C min⁻¹ to 1100 °C for 3 h (900 °C for nickel containing films), and subsequently cooled to room temperature.

Characterization. The ISV triblock terpolymer was characterized with a combination of ¹H-nuclear magnetic resonance (¹H-NMR) spectroscopy using a Varian Mercury spectrometer at 300 MHz and gel permeation chromatography (GPC) on a Waters ambient-temperature GPC at 23 °C (flow-rate 1 mL min⁻¹) with a Waters 2410 differential refractive index (RI) detector.

Scanning electron micrographs were obtained using either a Zeiss LEO 1550 FE-SEM with an in-lens detector and an accelerating voltage of 10-20 kV or a TESCAN MIRA3 LM FE-SEM using an in-lens detector and an accelerating voltage of 5-15 kV. The as-cast and post-90 °C samples were coated with gold-palladium prior to imaging, which accounts for the surface patterning.

Thermogravimetric analysis was conducted on a Q50 TGA from TA instruments under argon flow (90 mL min⁻¹) with a heating rate of 1 °C min⁻¹.

Raman spectroscopy was performed on a Renischaw InVia confocal Raman microscope with backscattering geometry at room temperature using a 785nm or diode laser as excitation source at 50x magnification.

Small-angle X-ray scattering (SAXS) on the membranes was performed on a custom-built lab-sized X-ray line using Cu K α radiation (wavelength 1.5418 Å).

X-ray diffractograms were obtained using a Rigaku Ultima IV multipurpose X-ray diffractometer equipped with a D/teX Ultra detector using Cu K α radiation (40V, 44mA, wavelength 1.5418 Å) in a 2 θ range between 10 and 90 degrees with a speed of 4 degrees min⁻¹.

REFERENCES

1. Rolison, D. R. *et al.* Multifunctional 3D nanoarchitectures for energy storage and conversion. *Chem. Soc. Rev.* **38**, 226–52 (2009).
2. Tappan, B. C., Steiner, S. A. & Luther, E. P. Nanoporous metal foams. *Angew. Chem. Int. Ed. Engl.* **49**, 4544–65 (2010).
3. Orilall, M. C. & Wiesner, U. Block copolymer based composition and morphology control in nanostructured hybrid materials for energy conversion and storage: solar cells, batteries, and fuel cells. *Chem. Soc. Rev.* **40**, 520–535 (2011).
4. Lakes, R. Materials with structural hierarchy. *Nature* **361**, 511–515 (1993).
5. Kresge, C. T., Leonowicz, M. E., Roth, W. J., Vartuli, J. C. & Beck, J. S. Ordered mesoporous molecular sieves synthesized by a liquid-crystal template mechanism. *Nature* **359**, 710–712 (1992).
6. Yang, P. D., Zhao, D. Y., Margolese, D. I., Chmelka, B. F. & Stucky, G. D. Generalized syntheses of large-pore mesoporous metal oxides with semicrystalline frameworks. *Nature* **396**, 152–155 (1998).
7. Joo, S. H. *et al.* Ordered nanoporous arrays of carbon supporting high dispersions of platinum nanoparticles. *Nature* **412**, 169–72 (2001).
8. Warren, S. C. *et al.* Ordered mesoporous materials from metal nanoparticle-block copolymer self-assembly. *Science (80-.)*. **320**, 1748–1752 (2008).
9. Wang, D. W., Li, F., Liu, M., Lu, G. Q. & Cheng, H. M. 3D aperiodic hierarchical

- porous graphitic carbon material for high-rate electrochemical capacitive energy storage. *Angew. Chemie - Int. Ed.* **47**, 373–376 (2008).
10. Phillip, W. A. *et al.* Tuning structure and properties of graded triblock terpolymer-based mesoporous and hybrid films. *Nano Lett.* **11**, 2892–900 (2011).
 11. Peinemann, K. V., Abetz, V. & Simon, P. F. W. W. Asymmetric superstructure formed in a block copolymer via phase separation. *Nat. Mater.* **6**, 992–6 (2007).
 12. Litster, S. & McLean, G. PEM fuel cell electrodes. *Journal of Power Sources* **130**, 61–76 (2004).
 13. Hamedani, H. A. *et al.* Microstructure, property and processing relation in gradient porous cathode of solid oxide fuel cells using statistical continuum mechanics. *J. Power Sources* **196**, 6325–6331 (2011).
 14. Liang, C., Hong, K., Guiochon, G. A., Mays, J. W. & Dai, S. Synthesis of a large-scale highly ordered porous carbon film by self-assembly of block copolymers. *Angew. Chem. Int. Ed. Engl.* **43**, 5785–5789 (2004).
 15. Tanaka, S., Nishiyama, N., Egashira, Y. & Ueyama, K. Synthesis of ordered mesoporous carbons with channel structure from an organic-organic nanocomposite. *Chem. Commun.* **0**, 2125–2127 (2005).
 16. Meng, Y. *et al.* Ordered mesoporous polymers and homologous carbon frameworks: Amphiphilic surfactant templating and direct transformation. *Angew. Chemie - Int. Ed.* **44**, 7053–7059 (2005).

17. Kosonen, H. *et al.* Functional Porous Structures Based on the Pyrolysis of Cured Templates of Block Copolymer and Phenolic Resin. *Adv. Mater.* **18**, 201–205 (2006).
18. Deng, Y. *et al.* Ordered mesoporous silicas and carbons with large accessible pores templated from amphiphilic diblock copolymer poly(ethylene oxide)-*b*-polystyrene. *J. Am. Chem. Soc.* **129**, 1690–1697 (2007).
19. Werner, J. G., Hoheisel, T. N. & Wiesner, U. Synthesis and characterization of gyroidal mesoporous carbons and carbon monoliths with tunable ultralarge pore size. *ACS Nano* **8**, 731–43 (2014).
20. Huang, Y. *et al.* One-step hydrothermal synthesis of ordered mesostructured carbonaceous monoliths with hierarchical porosities. *Chem. Commun. (Camb)*. 2641–2643 (2008). doi:10.1039/b804716b
21. Liang, C. & Dai, S. Dual phase separation for synthesis of bimodal meso-/macroporous carbon monoliths. *Chem. Mater.* **21**, 2115–2124 (2009).
22. Gu, Y., Dorin, R. M. & Wiesner, U. Asymmetric organic-inorganic hybrid membrane formation via block copolymer-nanoparticle co-assembly. *Nano Lett.* **13**, 5323–5328 (2013).
23. Dorin, R. M. *et al.* Designing block copolymer architectures for targeted membrane performance. *Polymer (Guildf)*. **55**, 347–353 (2014).
24. Dorin, R. M. *et al.* Solution Small-Angle X-ray Scattering as a Screening and Predictive Tool in the Fabrication of Asymmetric Block Copolymer Membranes.

- ACS Macro Lett.* **1**, 614–617 (2012).
25. Gu, Y., Werner, J. G., Dorin, R. M., Robbins, S. W. & Wiesner, U. Graded porous inorganic materials derived from self-assembled block copolymer templates. *Nanoscale* **7**, 5826–5834 (2015).
 26. Florent, M., Xue, C., Zhao, D. & Goldfarb, D. Formation mechanism of cubic mesoporous carbon monolith synthesized by evaporation-induced self-assembly. *Chem. Mater.* **24**, 383–392 (2012).
 27. Ruokolainen, J. *et al.* Supramolecular Routes to Hierarchical Structures: Comb-Coil Diblock Copolymers Organized with Two Length Scales. *Macromolecules* **32**, 1152–1158 (1999).
 28. Brunauer, S., Emmett, P. H. & Teller, E. Adsorption of Gases in Multimolecular Layers. *J. Am. Chem. Soc.* **60**, 309–319 (1938).
 29. Barrett, E. P., Joyner, L. G. & Halenda, P. P. The Determination of Pore Volume and Area Distributions in Porous Substances. I. Computations from Nitrogen Isotherms. *J. Am. Chem. Soc.* **73**, 373–380 (1951).
 30. Ferrari, A. & Robertson, J. Interpretation of Raman spectra of disordered and amorphous carbon. *Physical Review B* **61**, 14095–14107 (2000).
 31. Tuinstra, F. & Koenig, L. Raman Spectrum of Graphite. *J. Chem. Phys.* **53**, 1126–1130 (1970).

CHAPTER 3

BLOCK COPOLYMER SELF-ASSEMBLY DERIVED ASYMMETRIC POROUS CARBON MATERIALS FROM NON-EQUILIBRIUM PROCESSES

Abstract

Asymmetric porous inorganic materials provide increased accessibility and flux, making them attractive for applications in energy conversion and storage, separations, and catalysis. Non-equilibrium based block copolymer directed self-assembly approaches provide a route to obtaining such materials. We report on a one-pot synthesis using the co-assembly and non-solvent induced phase separation (CNIPS) of poly(isoprene)-*b*-poly(styrene)-*b*-poly(4-vinylpyridine) (ISV) triblock terpolymer and phenol formaldehyde resols. After heat-treatment, asymmetric porous carbon materials result with a mesoporous top surface atop a porous support with graded porosity along the film normal. The walls of the macroporous support are also mesoporous providing a structural hierarchy. Using a combination of *ex situ* transmission small angle x-ray scattering (SAXS) of the membrane dope solutions, *in situ* grazing incidence SAXS (GISAXS) after dope solution blading and during solvent evaporation, and scanning electron microscopy (SEM) of the final membrane structures, we demonstrate how successfully navigating the pathway complexity associated with the non-equilibrium approach of CNIPS enables switching from disordered to ordered top surfaces in the as-made organic-organic hybrids and resulting carbon materials after thermal treatments. We expect the final asymmetric porous carbon materials with hierarchical porosity in the substructure to be of interest for a number of applications, including batteries, fuel cells, and as catalyst supports.

Sarah A. Hesse, Peter A. Beaucage, Detlef-M. Smilgies, Ulrich Wiesner. *To be submitted for publication.*

Introduction

Porous inorganic materials have gained attention in applications ranging from energy conversion and storage to catalysis to separations.^{1,2} Porous carbon materials, a class of inorganic materials, find use in a broad range of applications including batteries, fuel cells, and gas separation due to their favorable chemical and physical properties such as high chemical resistance, compatibility with polymers, easy processability, as well as electrical and thermal conductivity.³⁻⁶ Initial studies used silica templates as a mold to make ordered mesoporous carbon materials.^{7,8} These initial hard-templating routes involve multiple processing steps, however, including the oftentimes highly chemically-hazardous removal of the template.⁹ For this reason, various soft-templating approaches were developed to fabricate ordered mesoporous carbons. These studies often utilized the self-assembling properties of block copolymers (BCPs) as structure-directing agents for organic carbon precursors, such as phenol formaldehyde resols or resorcinol resols.¹⁰⁻¹³

A number of these studies focused on the micro- and mesopore scale in order to maximize surface area. However, in order to increase accessibility/flux together with surface area, in 2015 Gu *et al.* developed a method for creating porous inorganic materials with graded porosity (Cornell Graded Materials – CGMs).¹⁴ These materials, instead of having only mesopores throughout the material, had pores from the meso- to the macroscale, arranged in an asymmetric and graded fashion along the film normal. The underlying process originally employed for the generation of ultrafiltration (UF) membranes is called self-assembly and non-solvent induced phase separation (SNIPS) – a non-equilibrium process pioneered in 2007 by Peinemann *et al.* for using a poly(styrene)-*b*-poly(2-vinylpyridine) diblock copolymer (SV) system.^{15,16} The SNIPS process combines the industrially well-utilized and scalable process of non-solvent induced phase separation

(NIPS) with block copolymer self-assembly.^{15,17,18} To that end block copolymers (BCPs) are dissolved in a selective solvent mixture. The resulting micellar solution is then blade-cast/doctor bladed and allowed to evaporate for a short period of time, which introduces a polymer concentration gradient along the film normal. The films are then precipitated in a non-solvent bath, typically water, thereby forming a structural gradient frozen into a polymer glass. When the formation parameters are tuned correctly, the resulting membranes possess well-ordered top surfaces with narrow pore size distribution, which continuously evolve into structures with increasing pore size along the film normal from meso- to macropores. Gu *et al.* used such BCP membranes as templates to deposit metals like nickel or copper, or carbon precursors, generating the first asymmetric porous inorganic membrane materials with a structural hierarchy after additional thermal processing.¹⁴

In order to decrease the number of processing steps in asymmetric porous organic-inorganic hybrid material formation, a process called CNIPS – co-assembly and non-solvent induced phase separation – was developed.¹⁹ This process is similar to the SNIPS process, however, instead of using just BCPs in the casting solutions, BCPs are employed as structure directing agents for inorganic precursor materials and are used together in the casting solutions thereby eliminating time consuming post-membrane formation processing steps.

In 2015 Hesse *et al.* used the CNIPS process to create asymmetric porous carbon materials with a hierarchy of structure.²⁰ ISV triblock terpolymer and phenol formaldehyde resols carbon precursors were combined in a one-pot solution, subjected to the CNIPS process and subsequently heat-treated to both cross-link the phenol formaldehyde resols and remove the polymer. The expectation was to obtain carbon

materials with an ordered top surface as is characteristic of materials made *via* the combination of BCP self-assembly and NIPS. However, while this proof-of-principle study yielded the characteristic asymmetric pore structure, no formation conditions were found to obtain membranes with periodically ordered pores in the top surface layer of the resulting carbon materials.

It is periodic pore order in the top-separation layer together with narrow pore size distributions, however, which sets SNIPS/CNIPS membranes apart from conventional UF membranes. This combination leads to maximum pore density, in turn providing high flux, which together with high resolution from narrow pore size distributions enables advanced membrane performance.²¹ The current study describes in-depth investigations into the early formation stages of CNIPS derived porous carbon materials from the ISV+resols system in order to generate a deeper understanding of the processes and parameters controlling periodic pore order in the top surfaces of these asymmetric membranes. We demonstrate that such fundamental understanding of the early formation stages enables generation of as-made hybrid materials as well as resulting asymmetric carbon membranes with highly ordered top surface pores. We anticipate that these results will help to transfer the benefits of scalable SNIPS/CNIPS type membrane formation processes into a host of other inorganic materials thereby opening up pathways for new applications not accessible for purely polymer-organic membrane materials.

Experimental Section

Materials Synthesis/Preparation

Materials. Materials were used as received except as otherwise indicated. Anhydrous (99.9 %) grades of tetrahydrofuran (THF) and 1,4-dioxane (DOX) were purchased from Sigma-Aldrich. Deionized (DI) water with a resistivity of 18.2 M Ω cm was used as the nonsolvent precipitation bath. The following chemicals were used for the synthesis of phenol formaldehyde resols: Phenol (Sigma-Aldrich, purified by redistillation, ≥ 99 %), formalin solution (Sigma-Aldrich, ACS reagent, 37 wt% in water, containing 10-15% methanol as stabilizer to prevent polymerization), sodium hydroxide (Sigma-Aldrich, reagent grade, ≥ 98 % pellets anhydrous), *para*-toluene sulfonic acid monohydrate (Sigma-Aldrich, ACS reagent, ≥ 98.5 %), deionized (DI) water with a resistivity of 18.2 M Ω cm.

Polymer Synthesis and Characterization. The poly(isoprene)-*b*-poly(styrene)-*b*-poly(4-vinylpyridine) (ISV) triblock terpolymer used in this study was synthesized *via* sequential living anionic polymerization as previously reported.¹⁸ The polymer had a molar mass of 95 kg mol⁻¹ with 29 vol% poly(isoprene) (PI), 57 vol% poly(styrene) (PS), 14 vol% poly(4-vinylpyridine) (P4VP) and a polydispersity index of 1.2. A Varian INOVA 400 MHz ¹H solution nuclear magnetic resonance (¹H NMR) spectrometer was used to determine the block fractions of each block using chloroform-d₆ as solvent (D, 99.8 %, Cambridge Isotope Laboratories). A Waters ambient-temperature gel permeation chromatograph (GPC) equipped with a Waters 410 differential refractive index (RI) detector (flow-rate 1 mL min⁻¹) was used to analyze the ISV polydispersity using polystyrene standards for polydispersity index (PDI) determination. Tetrahydrofuran (THF) was used as the solvent. Overall ISV molar mass was obtained using the molar

mass of the PI block (determined with GPC using PI standards) combined with the NMR results of the molar ratios of the different blocks.

Solution Preparation. ISV solutions were prepared by dissolving ISV at various concentrations in a solvent mixture of DOX:THF (7:3 by weight) and stirred to obtain homogeneous solutions. Oligomeric phenol_formaldehyde resols with a molar mass of less than 500 g mol^{-1} were synthesized using a procedure described elsewhere.^{10,20} A stock solution of 25 wt% resols in DOX, as well as a stock solution of 25 wt% resols in THF were prepared and combined in a 7:3 weight ratio to obtain a 25 wt% resols solution in DOX:THF (7:3 by weight). In the so-called “simultaneous method”, appropriate amounts of ISV powder and resols stock solution were combined to achieve the desired ISV/resols ratios (typically 2:1 by weight; see text for details) and DOX:THF (7:3 by weight) was immediately added before dissolution of the ISV to reach the desired polymer concentrations. In the so-called “consecutive method”, ISV was first dissolved in DOX:THF (7:3 by weight) to obtain a homogeneous solution, to which the resols stock solution was added thereafter to obtain the targeted ISV/resols weight ratio (typically 2:1). All solution concentrations used for ISV+resols refer to the ISV plus resols overall weight ratio in 7:3 DOX:THF.

Membrane Casting. Self-assembly/Co-assembly and non-solvent induced phase separation (S/CNIPS) was used to prepare the membranes. As described in the results and discussion section, two substrate temperatures (room temperature, RT, or 30 °C) and humidity environments (<28 % or ~70 %) were used. However, the general process remained the same. The casting solution was pipetted onto a glass substrate, a thin film was cast with a doctor blade using a gate height (height between the substrate and casting blade) between 203 and 229 μm . After various evaporation times, see main text, the films

were plunged into a non-solvent DI water bath to allow for precipitation (usually for 30 s). In the case of overnight stirring (*e.g.* see Figure 4), membranes were stirred in DI water overnight allowing for the dissolution of resols out of the membranes, effectively resulting in ISV membranes (with negligible amounts of resols).

Temperature Processing. The membranes were dried and heated in a convection oven to crosslink the resols at a temperature of 130 °C for about 24 h. This step was followed by a heat-treatment step in a flow furnace using nitrogen as the flow gas. The temperature profile for this carbonizing step was 1 °C min⁻¹ to 600 °C. The temperature was held at 600 °C for 3h before being further ramped at 5 °C min⁻¹ to 900 °C. The furnace was then kept at 900 °C for 3 h before being allowed to cool back to room temperature at ambient rate.

Materials Characterization

Small-Angle X-ray Scattering (SAXS) of solutions. Transmission SAXS measurements were performed at the G1 station of the Cornell High Energy Synchrotron Source (CHESS) with a typical beam energy of 9.8 keV and a sample-to-detector distance of about 2 m. The precise sample-detector distance was determined for each configuration using silver behenate. Samples were loaded in 0.9 mm glass capillaries (Charles Supper Co.), flame-sealed, and sealed with epoxy as a secondary seal. Two-dimensional scattering patterns were collected on either a Dectris Pilatus3 300k or a Dectris Eiger 1M pixel array detector. Patterns were azimuthally integrated and plotted using the Nika and Irena software packages for Igor Pro.^{22,23} The scattering vector q is defined as $q=(4\pi/\lambda)\sin\theta$, where θ is half of the scattering angle. Reported lattice

parameters were determined by fitting the primary peak with a gaussian function and converting the position to a lattice parameter assuming the indicated lattice. For the body centered cubic (BCC) lattice, the lattice parameter, a , was determined by: $a=2\sqrt{2}\pi/q^*$.

In Situ Grazing-Incidence Small-Angle X-ray Scattering (GISAXS). *In situ* GISAXS experiments were performed at the D1 station of the Cornell High Energy Synchrotron Source (CHESS) using a custom-built doctor blade setup as detailed by Smilgies *et al.*²⁴ A schematic of the experimental setup is provided elsewhere.²⁵ Solutions were cast by an automated doctor blade spreading the polymer solution across a glass substrate at $7500 \mu\text{m s}^{-1}$. Gate heights (coating gap between the substrate and the blade) of 203 or 229 μm were used. *In situ* GISAXS data was collected almost immediately after casting using a Pilatus 200k detector and exposure times of one second at three or 5 s intervals, between which the shutter was closed to limit radiation exposure of the sample. Representative selected intervals are shown in the figures. Incident angles of 0.12° to 0.15° were used, slightly below the critical angle of the glass substrate. GISAXS patterns are plotted against the scattering vector magnitude, q , with $q=4\pi \sin\theta/\lambda$, where θ is half of the total scattering angle and λ is the x-ray wavelength (1.16 Å or 1.17 Å). The software that was used to both plot the data and index the patterns to determine the lattice parameter is called indexGIXS.^{26,27} In order to obtain lattice parameters, a , of cubic lattices from the positions of the primary peak, q^* , the following equations were employed: simple cubic (SC) lattice: $a=2\pi/q^*$; for a BCC lattice: $a=2\sqrt{2}\pi/q^*$.

SEM Analysis. Scanning electron microscopy (SEM) micrographs were obtained using either a TESCAN MIRA3 FE-SEM using an in-lens detector and an accelerating voltage of 5-15 kV, or a ZEISS Gemini 500 Scanning Electron Microscope (SEM) and

voltage of 2kV. The as-made and post-130 °C treated samples were coated with gold-palladium prior to imaging. SEM images were brightness/contrast adjusted. Pore-to-pore distances were calculated by fast Fourier transform (FFT) analysis of the SEM micrographs (using the raw data, *i.e.* without post-SEM brightness/contrast adjustment) followed by radial integration using ImageJ with the Radial Profile plugin (Philippe Carl).

Thermogravimetric Analysis. Analysis was conducted on a TA Instruments Q500 thermogravimetric analyzer (TGA) under nitrogen flow. The temperature was ramped from room temperature at 1 °C min⁻¹ to 600 °C, holding isothermally at 600 °C for 3 h and then further ramping up at 5 °C min⁻¹ to 900 °C. The furnace was then held at 900 °C for 3 h before being allowed to cool back to room temperature at ambient rate.

Nitrogen Sorption. Nitrogen adsorption-desorption isotherms of the porous carbon materials were recorded using a Micromeritics ® ASAP 2020 surface area and porosity analyzer at -196 °C. The specific surface areas were determined following the Brunauer-Emmett-Teller (BET) method.^{28,29} Barrett-Joyner-Halenda (BJH) analysis was used to determine the pore size distributions.³⁰

Results and Discussion

Graded meso- and macro-porous carbon materials, referred to in the following as CGM-Cs, were obtained from a non-equilibrium type process using the combination of co-assembly and nonsolvent-induced phase separation (CNIPS) of triblock terpolymer poly(isoprene)-*block*-poly(styrene)-*block*-poly(4-vinylpyridine) (ISV) with phenol formaldehyde resols and a subsequent series of heat-treatments (Figure 3.1). Triblock terpolymer ISV employed here was synthesized *via* previously reported sequential anionic polymerization.¹⁸ The polymer had a molar mass of 95 kg mol⁻¹ with 29 vol% poly(isoprene) (PI), 57 vol% poly(styrene) (PS), 14 vol% poly(4-vinylpyridine) (P4VP) and a polydispersity index of 1.2. Phenol formaldehyde resols (resols) with a molar mass of less than 500 g mol⁻¹ were synthesized as described previously and used as thermally cross-linkable carbon precursor materials.^{13,20}

The CNIPS process and heat-treatment (Figure 3.1 bottom) for preparing CGM-C materials followed previously reported protocols.²⁰ Typically a 2:1 ratio by weight of ISV and resols in a 7:3 ratio by weight of DOX:THF were prepared into co-assembled solutions. After stirring, the homogeneous solutions were cast onto glass slides using a doctor blade and allowed to evaporate for a specific amount of time. This introduced a concentration gradient along the film-normal direction. Hereafter, the films were plunged into a nonsolvent, i.e. deionized (DI) water, bath.

The membranes were only immersed in the water for short periods of time (~30 s) to avoid dissolution of the hydrophilic resols in water. This concluded the CNIPS part of the process. The ISV+resols hybrid membranes were then subjected to a series of heat-treatments. They were first dried and subsequently

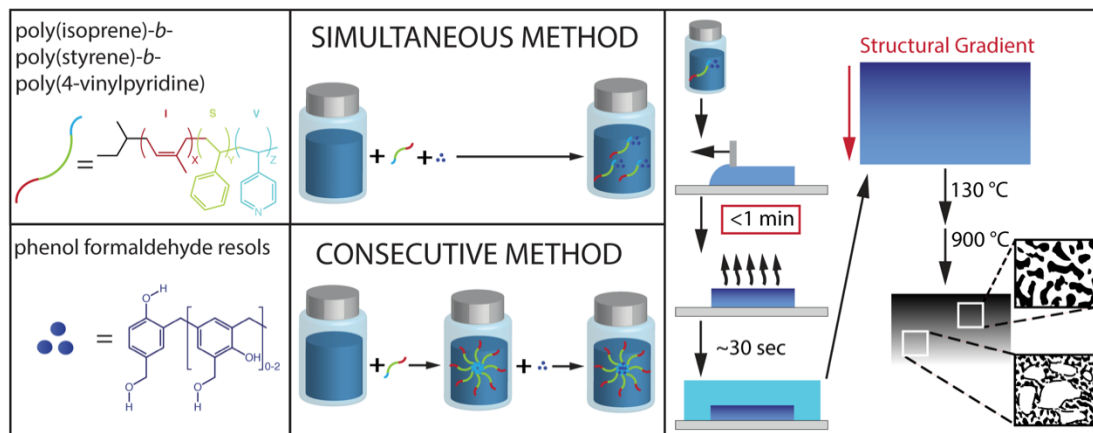


Figure 3.1. Schematic Representation of Chemical Components and CNIPS Process Pathways. Typically a 2:1 weight ratio of ISV and resols in a 7:3 ratio (by weight) of DOX:THF were cast onto a glass slide. The starting solutions were prepared by either a “simultaneous” or a “consecutive method” as indicated. The solutions were evaporated for a specific amount of time to induce a concentration gradient, and plunged into a DI water bath whereby the polymer was precipitated, converting the concentration gradient into a structural gradient. The resulting asymmetric membranes were subjected to a series of heat-treatments to crosslink the resols (130 °C) and carbonize the system (900 °C). The BCP decomposes during carbonization leading to shrinkage and additional mesoporosity.

cured at 130 °C to induce cross-linking of the resols. Cross-linking is essential to provide a stable structure for the subsequent carbonization step at 900 °C.

Two different methods were employed for making the casting solutions (Figure 3.1, top right). In the “simultaneous method”, stock solutions of 25 wt% resols in 7:3 DOX:THF were made and combined with ISV powder (2:1 ISV:resols by weight) without prior dissolution of the ISV. DOX and THF were added thereafter (7:3 DOX:THF) to dissolve the ISV and mix with the resols. In the “consecutive method”, ISV was first dissolved in 7:3 DOX:THF. After complete dissolution, the 25 wt% resols solution was added. In both the consecutive and simultaneous method, ISV terpolymer and carbon precursor were dissolved at a 2:1 ratio (by weight) in a 7:3 (by weight) DOX:THF solution, while solution concentrations were kept comparable (*vide supra*). It is important to note that the overall process following solution preparation for both the

consecutive method and simultaneous method was kept the same – in order to ensure a direct comparison between both methods. Any differences in structural characteristics of the membranes therefore could be traced back to the differences in the preparation of the casting solutions.

Small-Angle X-Ray Scattering (SAXS) of Solutions

Figure 3.2 compares selected small-angle x-ray scattering (SAXS) results of the different quiescent casting solutions employing the simultaneous (Figure 3.2b) and consecutive (Figure 3.2c) solution preparation methods with those of parent ISV (no additives, Figure 3.2a) in order to investigate the effects of resols additives as well as sample preparation method on order and structure as a function of solution concentration (marked for each trace). For pure ISV (Figure 3.2a), results for solutions ranging from 0.5 wt% to 17 wt% ISV in 7:3 DOX:THF are exhibited. While at the lowest concentration no particular structure is evident, a correlation peak first emerging at 4.1 wt% suggests onset of micelle formation without ordered packing. Beyond 10 wt% a clear lattice is evidenced by well-defined higher order peaks consistent with a body-centered cubic (BCC) lattice with a lattice parameter of 57 nm at 17 wt%, consistent with previously reported results.³¹

SAXS patterns of ISV+resols solutions prepared *via* the simultaneous method (Figure 3.2b) and ranging in concentration from 0.8 wt% to 17 wt% (ISV+resols at 2:1 ISV:resols weight ratio) show a similar evolution but with two major differences: First, peaks are shifted to smaller q values, suggesting larger characteristic structures consistent with resols swelling the system. Second, no specific lattice could be associated with the relatively broad first and higher order

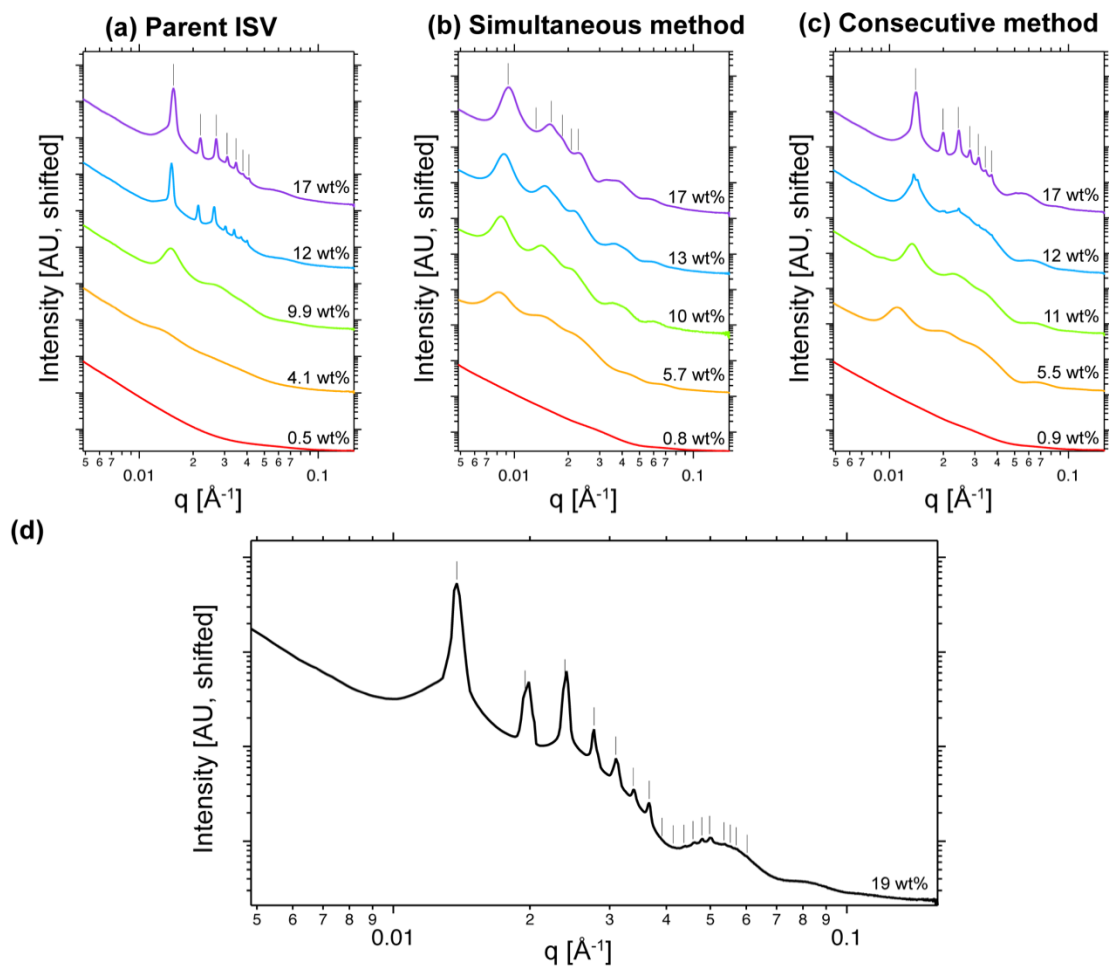


Figure 3.2. Small-angle x-ray scattering patterns of solutions of (a) parent ISV, (b) simultaneous method ISV+resols (2:1 ISV:resols by weight), (c) consecutive method ISV+resols (2:1 ISV:resols by weight), (d) selected pattern of consecutive method at 19 weight% ISV+resols (2:1 ISV:resols by weight). All solutions were 7:3 DOX:THF (by weight). Tick marks indicate expected peak positions for a body-centered cubic (BCC) lattice relative to the observed primary peak. The (a) ISV concentrations and (b, c, d) ISV+resols concentrations are reported with each trace.

reflexes, even at the highest concentrations studied (see also Figure S3.1). Interestingly, both of these effects are reverted when the consecutive method is used for sample preparation (Figure 3.2c). At 17 wt% SAXS data again suggest a BCC lattice with a lattice parameter of 63 nm, i.e. only slightly larger as compared to the pure ISV system at the same overall concentration. Figure 3.2d provides the scattering pattern of a 19 wt%

ISV+resols solution prepared by this method exhibiting 13 higher order peaks and consistent with a BCC lattice with a spacing of 64 nm. To the best of our knowledge this is the largest number of higher order reflexes observed for a ISV based micellar lattice in 7:3 DOX:THF.^{16,31} The individual BCC lattice reflexes sit on top of oscillations that presumably are due to the form factor of the micelles.

We hypothesize that in the simultaneous case, the addition of resols prior to dissolution of the ISV hinders the ISV polymer from forming homogeneous micelles and therefore from forming well-ordered micellar BCC lattices in solution. In the meantime we know from independent studies (data not shown) that the P4VP block rather than the PI block of ISV in 7:3 DOX:THF forms the micelle core. The reason why the presence of resols hinders highly ordered micelle lattice formation might be that they hydrogen bond to the P4VP blocks upon dissolution early on, thereby locking the system into large structures that cannot equilibrate into well-defined micellar lattices. In contrast, in the consecutive case, ISV polymer micelles are allowed to form first, before addition of the resols, therefore allowing for cubic micelle lattice formation with only slightly larger lattice spacings as for the parent ISV terpolymer presumably due to swelling of the P4VP micelle cores.

Figure S3.1 shows SAXS patterns of the full concentration series studied (including points between those in Figure 3.2) as well as a table of concentration versus lattice spacings based on the first order peak position and assuming a BCC lattice in all cases. The onset of cubic ordering in the parent ISV case (Figure S3.1a) occurs at comparable overall concentration (~12 wt%) as in the ISV+resols consecutive case (Figure S3.1c). This means that in the ISV+resols case ordering occurs at a lower ISV concentration – so less polymer is needed to obtain cubic order in solution with a similar lattice parameter. This

is again consistent with swelling of the micelle cores with resols which after mixing into the existing BCP micelle solutions may simply diffuse into the existing P4VP cores and expand their size.

In Situ Grazing-Incidence Small-Angle X-Ray Scattering (GISAXS)

To elucidate the behavior of this pathway-dependent system during evaporation, *in situ* grazing-incidence small-angle x-ray scattering (GISAXS) during blade-coating and evaporation was performed.²⁵ Details are provided in the experimental section. In short, films were cast with a doctor blade and the subsequent evaporation process monitored *in situ* at various times using GISAXS. During successful S/CNIPS based membrane formation, this evaporation process leads to long range BCP micelle ordering as evidenced by Bragg reflection spots in the GISAXS patterns in a layer formed atop a disordered substructure.

Figure 3.3a-c shows representative time dependent *in situ* GISAXS pattern sequences for all three scenarios tested, *i.e.* for parent ISV terpolymer (a), as well as for ISV+resols (2:1 ISV:resols weight ratio) systems prepared either with the simultaneous (b) or consecutive (c) methods.

Figures S3.2 to S3.5 of the SI summarize all data sets collected together with specific indexed patterns. Figure 3a shows *in situ* GISAXS patterns of a film cast from a

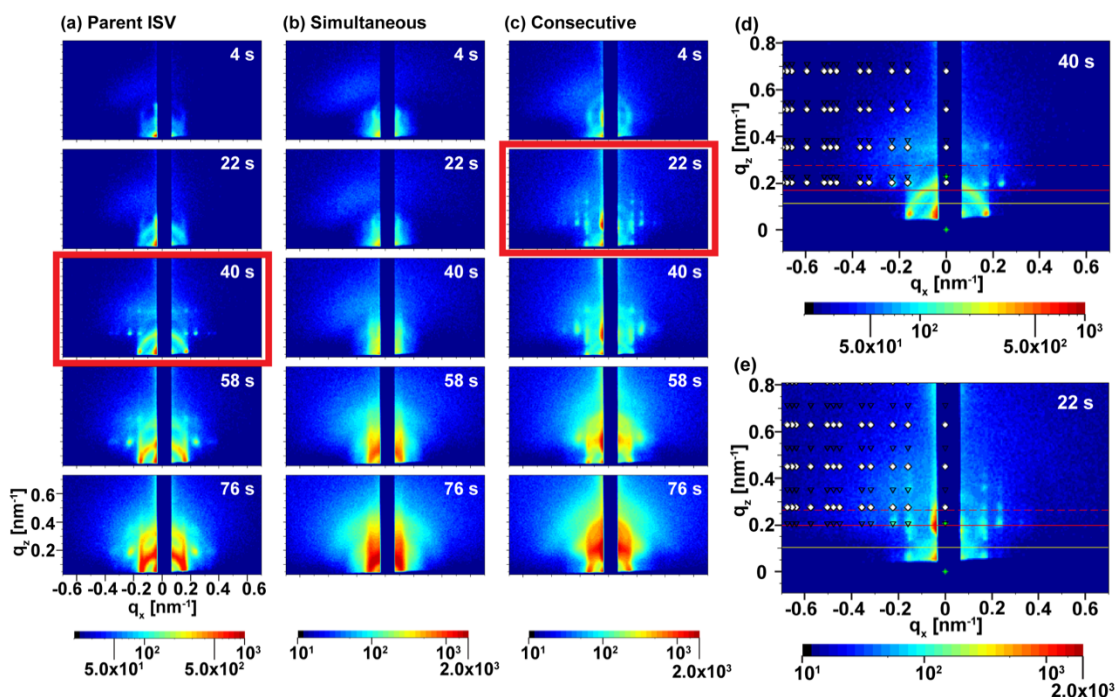


Figure 3.3. Selected in situ GISAXS patterns of solutions of (a) 10 wt% ISV, (b) 10 wt% ISV+resols simultaneous method (2:1 ISV:resols by weight), (c) 10 wt% ISV+resols consecutive method (2:1 ISV:resols by weight) cast and evaporated for various times. The two images boxed in red (a) 40 s and (c) 22 s were indexed in (d) and (e), respectively. All solutions were 7:3 DOX:THF (by weight). Spot markings in (d) and (e) correspond to those expected for a SC lattice with the (001) plane parallel to the surface and lattice parameters of 38 nm and 39.5 nm, respectively.

10 wt% solution of parent ISV terpolymer and collected at different solvent evaporation times ranging from 4 s to 76 s. The film started out disordered, with very faint scattering rings evident at the earliest time point (4 s evaporation time). These scattering rings become more prominent at 22 s. The half-ring (lower ring) at smaller q is caused by transmission scattering, while the upper full ring is associated with reflection scattering. Discrete Bragg reflection spots first emerge at an evaporation time of 40 s. This marks the transition from a disordered to a highly ordered state with long-range order. As time progresses, the Bragg spots become more intense, but on the time scale shown up to about 80 s never disappear.

In contrast, time dependent *in situ* GISAXS patterns over the same time interval resulting from the evaporation of a film cast from a 10 wt% ISV+resols solution (2:1 ISV:resols weight ratio) prepared *via* the simultaneous route do not exhibit well defined reflection spots, suggesting disordered micelle structures at all times studied (Figure 3.3b). Finally, the time dependent progression of *in situ* GISAXS patterns resulting from a film that was cast from a 10 wt% ISV+resols solution (2:1 ISV:resols weight ratio) prepared *via* the consecutive method shown in Figure 3.3c is again more similar to that of the parent ISV polymer, except that well-defined reflections signaling long-range order appear earlier, here around 22 s rather than 40 s, and are getting washed out at the longest time points shown around 80 s.

In situ GISAXS patterns at 40 s for series (a) and 22 s for series (c) were simulated using indexGIXS.^{26,27} The indexed patterns are shown in Figure 3.3d and 3.3e, respectively. The circles and triangles indicate expected peak positions for simple cubic (SC) lattices for the directly scattered and reflected beams, respectively. The sample horizon is indicated by the yellow line, while the polymer critical angle, and substrate critical angle are indicated by the solid and dashed red lines, respectively. The region between the polymer and substrate critical angles is called the Yoneda band.³² Patterns in Figure 3.3d and 3.3e for 10 wt% solutions of pure ISV at 40 s and ISV+resols prepared *via* the simultaneous method at 22 s were both indexed to an SC lattice with the (001) plane in the in-plane direction relative to the film surface, and lattice parameters of 38 nm and 39.5 nm, respectively.

Table 3.1 summarizes all the quantitative *in situ* GISAXS analysis results with additional data sets and indexing results at varying concentrations provided in Figures S3.2 to S3.5 of the Supporting Information. In the pure ISV case, SC

Polymer system	System wt%	Obs. ordered structure	Lattice spacing [nm]	Exp. q^* [nm^{-1}]
ISV	7.9	SC	39.5	0.159
ISV	10	SC	38.0	0.165
ISV+resols (simultaneous)	8.0, 10, 12, 15	—	—	—
ISV+resols (consecutive)	8.0	SC	40.5	0.155
ISV+resols (consecutive)	10	SC	39.5	0.159
ISV+resols (consecutive)	13	SC	39.5	0.159
ISV+resols (consecutive)	15	BCC	58.0	0.153

Table 3.1. Summary of in situ GISAXS pattern analysis for different solution concentrations indicating suggested BCP film surface lattices and corresponding lattice spacings.

lattices with lattice parameters of 39.5 nm and 38 nm emerged for the 7.9 wt% (Figure S3.2a) and 10 wt% ISV solutions (Figure 3.3a and S3.2b) in 7:3 DOX:THF, respectively. For ISV+resols solutions prepared *via* the simultaneous method, no pattern could be ascribed to any particular lattice with long-range order (Figure 3.3b and S3.3). Instead, disordered structures dominated the behavior as evidenced by the formation of scattering rings (Figure S3.3c and S3.3d). For the consecutive case, however, all tested concentrations resulted in patterns that could be indexed to a particular lattice with long-range order (Figure S3.4). At lower concentrations of 8.0 wt%, 10 wt%, and 13 wt% (Figures S3.4 a-c), GISAXS patterns at 31 s, 22 s, and 13 s evaporation time were consistent with SC lattices with the (001) plane parallel to the surface and lattice parameters of 40.5 nm, 39.5 nm, 39.5 nm, respectively, while at the highest concentration tested of 15 wt% (Figure S3.4d), the GISAXS pattern at the 21 s time-point was consistent with a BCC lattice with the (110) plane parallel to the film surface and a lattice

parameter of 58 nm (Figure S3.5). This latter high concentration case was the sole example of BCC ordering in the membrane top surface layer consistent with ordering that was found for quiescent solutions at higher concentrations (Figure 3.2c).

These *in situ* GISAXS results obtained for our 95 kg mol⁻¹ ISV terpolymer based studies are consistent with those reported by Gu *et al.* for pure ISV cast films with varying molar mass and similar terpolymer composition and corroborate the overall picture that order in the top surface layer of these membranes evolves from disorder to BCC and then to SC lattices, the former consistent with solution structures at higher concentrations as observed with SAXS studies (see Figure 3.2) and the latter being consistent with the pore structure of the final ISV membranes (*vide infra*).²⁵ For a 91 kg mol⁻¹ ISV terpolymer these authors observed an SC lattice at a lower ISV concentration of 10 wt%, while solution SAXS at higher concentration of 16 wt% confirmed a BCC lattice. Furthermore, for a smaller, 43 kg mol⁻¹ ISV terpolymer at 16 wt% they observed a transition from a BCC to a SC lattice, with both lattices having the same lattice orientation relative to the substrate as found in the current study. Consistent with the interpretation of results in this earlier investigation, we infer that the highest ISV+resols concentration of 15 wt% studied here for the consecutive method generates samples of sufficiently high viscosity to prevent the final BCC to SC transition – thereby trapping the system in the BCC order state.

From these results on the early membrane formation stages upon solvent evaporation after blading, the addition of resols to ISV does not seem to substantially perturb the structure formation process if, and only if, the resols are added to the terpolymer using the consecutive method. In contrast, as is revealed by these *in situ* GISAXS studies, adding ISV and resols simultaneously to the 7:3 DOX:THF solvent mixture does prevent well-defined lattice formation.

Qualitatively, comparing *in situ* GISAXS with transmission solution SAXS results (*i.e.* compare Figure 3.2a-c with Figure 3.3a-c), it is apparent that while parent ISV as well as consecutive method derived ISV+resols solutions and films exhibit highly ordered (cubic) lattices, results from the simultaneous case do not. For a more quantitative comparison of solution SAXS with *in situ* GISAXS results, in particular for the consecutive method of interest here, the GISAXS pattern obtained from the 15 wt% ISV+resols solution after 21 s of evaporation (Figure S3.5d) and indexed to a BCC lattice with a lattice parameter of 58 nm can be directly compared to the corresponding solution SAXS results for concentrations above 15 wt%, as all these solution results could also be indexed to BCC lattices (see Figure S3.1c) and the 15 wt% in the GISAXS experiments only indicates the starting solution concentration. For example, comparison to the BCC lattice parameter of 63 nm of an 18 wt% ISV+resols solution (see Table in Figure S3.1d) shows that the lattice parameter results deviate by less than 10%. This corroborates earlier studies of ISV solutions and resulting SNIPS derived ISV based UF membranes demonstrating that solution SAXS is a good predictor of UF membrane surface structure.¹⁶ From our current studies this result also seems to hold for consecutive method derived ISV+resols mixed membranes.

Characterization of As-Made Membranes via Scanning Electron Microscopy

(SEM)

Following x-ray solution and *in situ* evaporation studies, membranes cast *via* the CNIPS process were characterized in the as-made state using scanning electron microscopy (SEM). As-made is defined as being the state immediately following

Polymer System	Rel. humidity [%]	Substrate T	Non-solvent bath T	Obs. surface order
ISV	<30	RT	RT	cubic
ISV	~70	RT	RT	—
ISV	~70	30 °C	RT	cubic
ISV+resols (consecutive)	<30	RT	RT	—*
ISV+resols (consecutive)	<30	30 °C	RT	cubic
ISV+resols (consecutive)	<30	30 °C	4 °C	cubic
ISV+resols (consecutive)	<30	30 °C	40 °C	cubic
ISV+resols (simultaneous)	<30	RT	RT	—
ISV+resols (simultaneous)	<30	30 °C	RT	—

Table 3.2. Summary of experiments conducted to elucidate optimized experimental conditions for obtaining ordered top surfaces in membranes cast via the S/CNIPS process.

precipitation in the non-solvent bath. Alternatively, after casting membranes were left in the DI water bath overnight under stirring in order to provide enough time for the resols to be washed out, which we expected would improve visualization of porosity *via* SEM.

In order to screen for optimal membrane structure formation, various parameters including evaporation time, substrate temperature, and water bath conditions were tested.

A summary of the results from varied substrate temperatures as well as non-solvent bath temperatures is provided in Table 3.2, while the full set of scanning electron micrographs is provided in Figures S3.6 to S3.11.

While casting at room temperature resulted in ordered top surfaces in the pure ISV dopes (Figure S3.6), such conditions did not result in optimal surface ordering for ISV+resols dopes (see results for consecutive method in Figure S3.7 where the closest to cubic order was observed at the 90 s evaporation time point). To search for experimental conditions for improved top surface ordering, the casting substrate temperature was varied. Instead of a room temperature substrate, membranes were cast on a 30 °C substrate. This resulted in substantially improved top surface order for both 10 wt% and 15 wt% ISV+resols casting solutions using the consecutive method (compare results in Figure S8 with those in Figure S3.7). When the heated substrate approach was applied to the simultaneous preparation method, it failed (Figure S3.9). When it was applied together with increased humidity casting conditions (~70 % relative humidity) for the pure parent ISV system, which resulted in poor ordering on room temperature substrates under these conditions, it indeed helped improve the order of the top surface of the material (Figure S3.10). Finally, for the consecutive method, three water bath temperatures were tested to probe their effects on membrane top surface order (Figure S3.11). When dipping into DI water baths at room temperature (~20 °C, left images) and 4 °C (right images), the cubic order which developed during the evaporation was preserved, whereas when dipping into a warmed 40 °C (middle images) bath, the order was not preserved.

Figure 3.4 shows SEM characterization results for optimized membrane formation conditions, i.e. cast at low relative humidity (<30 %), evaporated for 45 s on RT (~20 °C, 4a) or 40 s on 30 °C (3.4b and 3.4c) substrates, before being plunged into a RT (~20 °C) nonsolvent DI water bath, obtained from the following polymer dope solutions in 7:3 DOX:THF: 9.9 wt% parent ISV (Figure 3.4a), 10 wt% ISV+resols (2:1 ISV:resols weight ratio) simultaneous method (Figure 3.4b), and 10 wt% ISV+resols

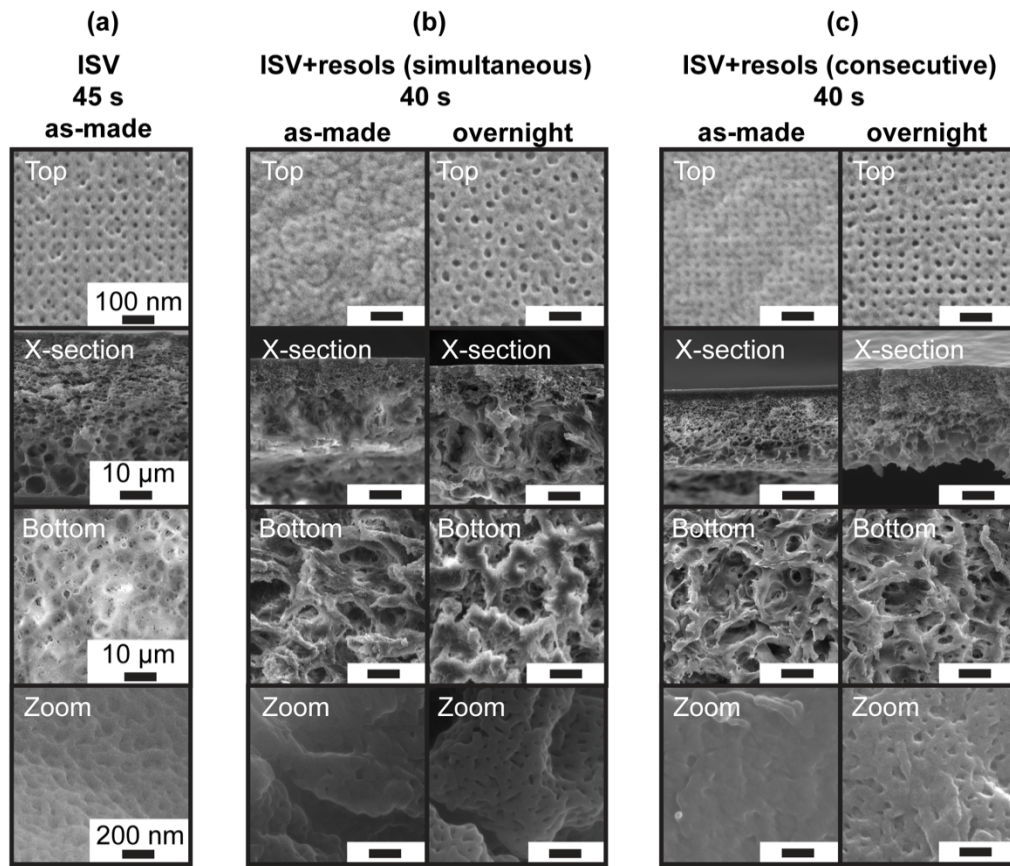


Figure 3.4. SEM characterization of membranes prepared from (a) 9.9 wt% ISV, (b) 10 wt% ISV+resols (2:1 ISV:resols weight ratio) and *via* the simultaneous method, and (c) 10 wt% ISV+resols (2:1 ISV:resols weight ratio) and *via* the consecutive method. The solutions were in 7:3 DOX:THF, cast, and evaporated for (a) 45 s on a RT (~ 20 °C) substrate, or (b+c) 40 s on a 30 °C substrate, respectively. All films were cast at low relative humidity (<30 %) and plunged into a RT (~ 20 °C) nonsolvent DI water bath. Micrographs from top to bottom respectively show top surface, cross-section, bottom surface, and a zoomed-in image from the macroporous region of the membrane. Scale bars are the same in all rows as indicated on the left.

(2:1 ISV:resols weight ratio) consecutive method (Figure 3.4c). For both simultaneous and consecutive cases, membrane samples were taken following 30 s of exposure to (left column), as well as overnight stirring in (right column), the non-solvent DI water bath (*vide supra*).

As is evident from these images, good quality surface ordering was achieved for

both the parent ISV membrane, as well as for the membrane obtained from the consecutive method. In contrast, well ordered top surface layers of membranes formed using the simultaneous method were not observed, consistent with x-ray scattering results reported in the previous sections. Fast Fourier transform (FFT) analysis of top surface order (Figure S3.12), while not applicable to membranes obtained from the simultaneous method (Figure S3.12b), yielded pore-to-pore distances (based off of the q^* position and assuming SC lattices) of 39 nm for the parent ISV case (Figure S3.12a) as well as 32 nm (red, as-made) and 40 nm (blue, overnight stirring) for consecutive method derived membranes (Figure S3.12c). These results were consistent with those obtained by manually measuring >50 pore-to-pore (channel-to-channel) distances using the measuring tool in ImageJ (data not shown). These results are consistent with the corresponding *in situ* GISAXS derived values of 38 nm and 39.5 nm for 10 wt% ISV and ISV+resols derived membranes (see Table 3.1).

Heat-Treatment of As-Made Membranes and Comparison to Carbonized

Materials

Once optimized parameters (low, <30 % relative humidity, 30 °C heated substrate, RT, ~20 °C non-solvent DI water bath) leading to ordered top surfaces in the organic-organic (ISV-resols) hybrid membranes were identified, these membranes were subjected to a series of heat-treatments to produce carbon materials. Immediately following casting and precipitation, as-made membranes were dried at room temperature and then underwent heat-treatment at 130 °C, both in a vacuum oven, in order to cross-link the resols. After heat-treatment (Figure S3.13) to this moderate temperature (*i.e.* below

polymer decomposition temperatures), surface features became less prominent and pores appeared to close (Figure S3.13).

After cross-linking, the membranes were heat-treated in a flow furnace under inert atmosphere (nitrogen) at $1\text{ }^{\circ}\text{C min}^{-1}$ to $600\text{ }^{\circ}\text{C}$ for 3h, immediately followed by ramping to $900\text{ }^{\circ}\text{C}$ at $5\text{ }^{\circ}\text{C min}^{-1}$ for 3h. In this process, the polymer decomposed (Figure S3.14). However, the structure was preserved due to the cross-linked resols, which were converted to a carbon material as described and analyzed in depth in previous publications.^{13,20} Figure 5 provides a comparison by means of SEM characterization of membrane top surfaces (top rows) and cross sections (bottom rows) between as-made membranes prepared from an 11 wt% and a 10 wt% ISV+resols (2:1 ISV:resols weight ratio) solutions in 7:3 DOX:THF *via* simultaneous and consecutive method, respectively, and their carbonized counterparts.

In the simultaneous method as-made case (Figure 3.5a), a disordered mesoporous top surface transitioned into a support structure of about $20\text{ }\mu\text{m}$ thickness with asymmetric porosity. Figure 3.5a also shows that while overall features remained similar, increasing evaporation time resulted in a denser and thinner cross-section, likely due to the evaporation of more solvent out of the membrane. When this organic-organic hybrid material was carbonized (Figure 3.5c), the overall asymmetric structure was retained. However, due to material loss and associated material shrinkage, membrane thickness was reduced to about $10\text{ }\mu\text{m}$ (compare cross section scale bars in Figure 3.5a/c). Finally, this SEM analysis demonstrates that an increased evaporation time resulted in smaller feature sizes on the mesoporous top surface.

For the consecutive method as-made and carbonized cases (Figure 3.5b/d) general trends were the same as described for the simultaneous method. The main

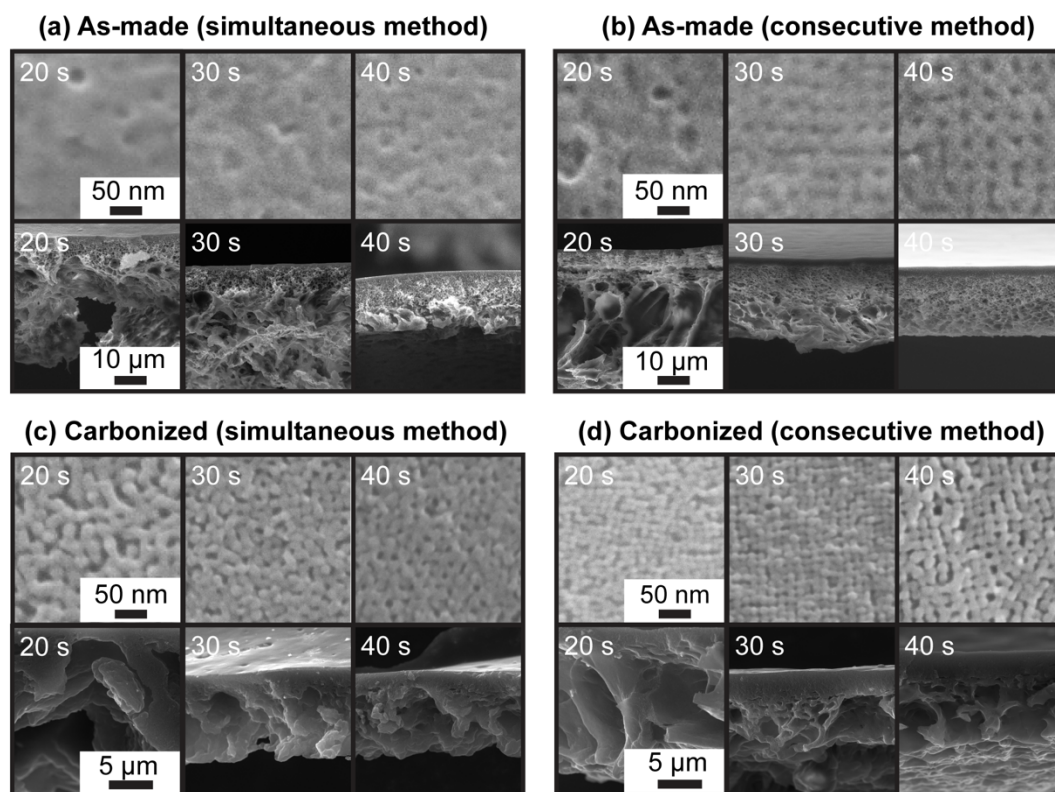


Figure 3.5. Top surface (top rows) and cross-section (bottom rows) SEM characterization of (a) as-made and (c) corresponding carbonized membranes prepared via the simultaneous method from an 11 wt% ISV+resols (2:1 ISV:resols weight ratio) solution in 7:3 DOX:THF. SEM characterization of (b) as-made and (d) corresponding carbonized membranes prepared via the consecutive method from a 10 wt% ISV+resols (2:1 ISV:resols weight ratio) solution in 7:3 DOX:THF. The films were cast at the same height. However, with increased evaporation time from 20 to 40s (left to right), more solvent evaporates, producing denser and thus thinner thickness membranes. The films were cast at low relative humidity (<30 %) onto a 30 °C heated substrate, and allowed to evaporate for various amounts of time (20-40 s, as indicated) before being plunged into a RT (~20 °C) nonsolvent DI water bath. Scale is the same for all rows as indicated by scale bars on the left side.

difference, however, was the highly ordered, cubic top surface order of the as-made materials, in particular at longer evaporation times, which was retained in the final carbonized membranes. Similar results were obtained for membranes which were cast from a 15 wt% ISV+resols solution (Figure S3.15).

Characterization of Carbon Materials

A more in-depth characterization of carbon materials prepared via both the simultaneous and consecutive method using SEM and nitrogen sorption analysis are shown in Figure 3.6 and 3.7, respectively.

The carbon materials resulting from the simultaneous method possessed a homogeneous top surface, but with only disordered arrays of mesopores (Figure 3.6a, b). In contrast, for carbon materials obtained from the consecutive method employing optimized membrane formation parameters, a top surface with periodic local cubic order was achieved (Figure 3.7a, b).

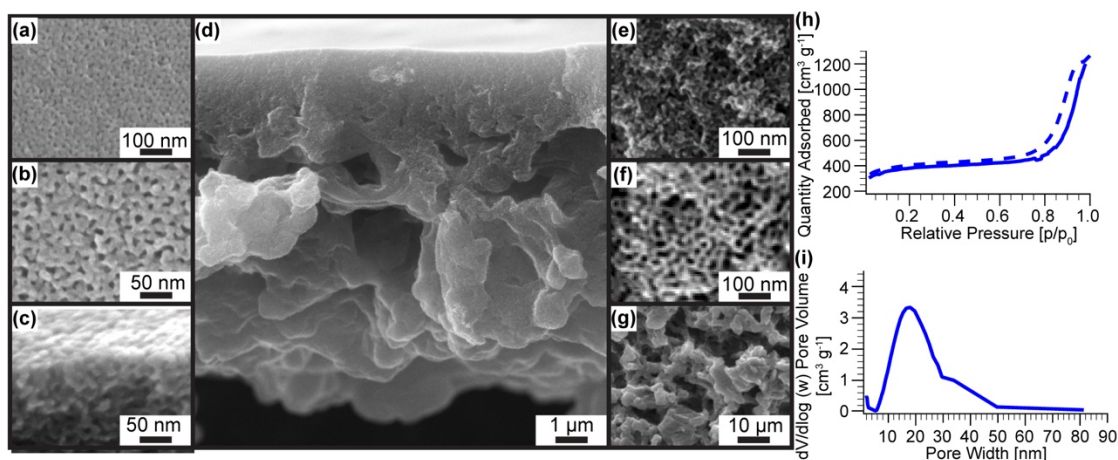


Figure 3.6. Characterization of carbon materials carbonized from membranes which were obtained from 11 wt% ISV+resols (2:1 ISV:resols weight ratio) solutions in 7:3 DOX:THF prepared *via* the simultaneous method, cast onto a 30 °C heated substrate, allowed to evaporate at low relative humidity conditions (<30 %) for 40 s before being plunged into a RT (~20 °C) nonsolvent DI water bath, dried, cross-linked at 130 °C for <24 h, and carbonized. The temperature profile for the carbonizing step was first heating at a rate of 1 °C min⁻¹ to 600 °C. The temperature was held at 600 °C for 3h before being further ramped at 5 °C min⁻¹ to 900 °C, where it was held for 3 h before being allowed to cool back to room temperature. (a)-(g) Scanning electron micrographs: (a)-(c) Top surface images at different magnifications, (d) full asymmetric cross-section, (e) mesoporous middle part of cross-section, (f) higher magnification mesoporous middle part of cross-section, (g) macroporous bottom. (h) Nitrogen sorption isotherms of the carbonized material. (i) BJH derived pore size distribution of the final carbonized membrane material.

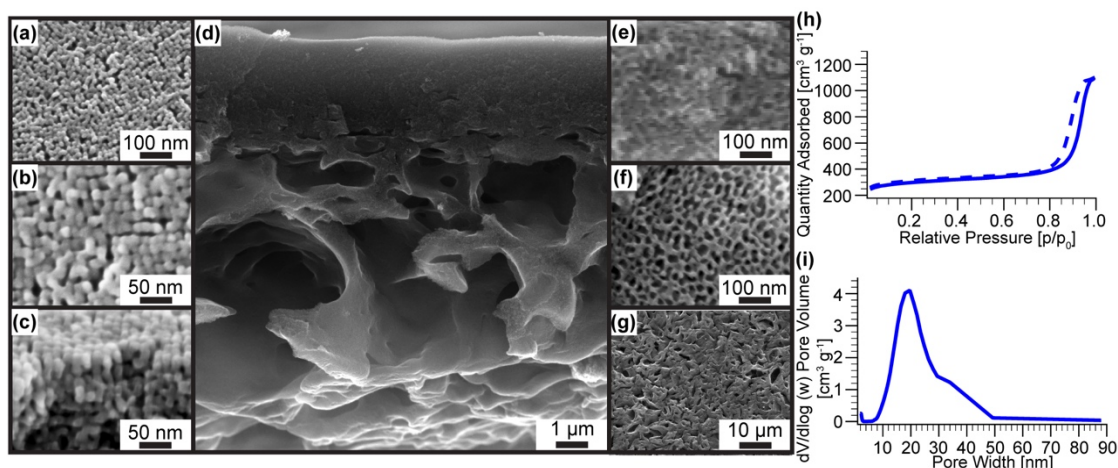


Figure 3.7. Characterization of carbon material carbonized from membranes which were obtained from 10 wt% ISV+resols (2:1 ISV:resols weight ratio) solutions in 7:3 DOX:THF prepared *via* the consecutive method, cast onto a 30 °C heated substrate, allowed to evaporate at low relative humidity conditions (<30 %) for 40 s before being plunged into a RT (~20 °C) nonsolvent DI water bath, dried, cross-linked at 130 °C for <24 h, and carbonized. The temperature profile for the carbonizing step was first heating at a rate of 1 °C min⁻¹ to 600 °C. The temperature was held at 600 °C for 3h before being further ramped at 5 °C min⁻¹ to 900 °C, where it was held for 3 h before being allowed to cool to room temperature. (a)-(g) Scanning electron micrographs: (a)-(c) Top surface at different magnifications, (d) full asymmetric cross-section, (e) mesoporous middle part of cross-section, (f) higher magnification mesoporous middle part of cross-section, (g) macroporous bottom. (h) Nitrogen sorption isotherms of the carbonized material. (i) BJH derived pore size distribution of the final carbonized material.

It is evident from comparing these SEM images with those of the parent ISV membrane or the ISV+resols consecutive method derived as-made/overnight samples (e.g. see Figure 3.4a/c), that the original array of square ordered mesopores in the top surface layer of these materials is replaced by square ordered arrays of dimples in the carbonized materials.

We therefore conclude that in the top surface layer the resulting carbon material stems from resols that originally filled the P4VP coated (pore) space of the ISV membrane in the co-assembly process. This square ordering extends a few micelle layers

down along the film normal (Figure 3.7c) before the order is lost in the meso- to macro-porous substructure.

Simultaneous and consecutive methods resulted in asymmetric carbon structures (Figure 3.6d, 3.7d) with mesoporosity throughout the material. This porosity was characterized via nitrogen sorption isotherms analyzed using the Brunauer-Emmett-Teller (BET) method (Figure 3.6h and 3.7h).

Type-IV curves with H1-type hysteresis and sharp capillary condensations above relative pressures of 0.9 were observed in both cases. For the simultaneous method, a BET surface area of $1322 \text{ m}^2 \text{ g}^{-1}$ with a weighing error of $357 \text{ m}^2 \text{ g}^{-1}$, micropore area of $837 \text{ m}^2 \text{ g}^{-1}$, and specific pore volume of $1.96 \text{ cm}^3 \text{ g}^{-1}$ at $p/p_0=0.99$ were obtained. For the consecutive method, a slightly lower BET surface area of $1024 \text{ m}^2 \text{ g}^{-1}$ with a weighing error of $143 \text{ m}^2 \text{ g}^{-1}$, micropore area of $655 \text{ m}^2 \text{ g}^{-1}$, and specific pore volume of $1.69 \text{ cm}^3 \text{ g}^{-1}$ at $p/p_0=0.99$ were obtained. BJH pore size distributions of materials prepared from both methods had also similar profiles (Figure 3.6i and 3.7i). For the material from the simultaneous method, the pore size distribution peaked at 18 nm with a FWHM of 15 nm, while for the material from the consecutive method the values were 20 nm and 12 nm for peak pore size and FWHM, respectively.

Conclusions

We reported on the successful non-equilibrium type one-pot synthesis method to obtaining asymmetric porous carbon materials with ordered top-surface layers and hierarchical substructure with meso- and macropores. To that end, approaches were pursued in which carbon precursors (resols) were either simultaneously or consecutively mixed with the structure directing triblock terpolymer, ISV. Both methods generally resulted in approximately 10 micron thick carbon materials with a mesoporous top surface layer which continued into a support structure with increasing pore size along the film normal, ending in a macroporous structure at the membrane bottom. The difference between the two methods is that only after carefully screening various processing conditions the optimized consecutive method resulted in an ordered top surface layer in the resulting porous carbon materials. In the consecutive method, ISV was first dissolved in a 7:3 DOX:THF solvent mixture, before the addition of resols, which likely allows for the formation of uniform micelles in solution prior to the addition of hydrogen bonding additive, and therefore allows for the evolution of ordered solution structure with increasing concentration as evidenced by SAXS of quiescent ISV+resols solutions. This order also occurs in the top surface layer of as-made membranes upon solvent evaporation as evidenced by *in situ* GISAXS experiments and SEM images of the resulting top surfaces of the final carbon materials. In contrast to the consecutive method, even after carefully screening a variety of processing conditions the simultaneous method (in which resols are already present when the polymer dissolves and forms micelles) only resulted in relatively disordered structures both in quiescent solutions as well as in the resulting membranes as evidenced by SAXS, *in situ* GISAXS, and SEM of the final carbons.

We expect that the insights gained by these fundamental solution and evaporation studies will aid in expanding the types of additives which can be combined with polymers in the CNIPS process, while successfully maintaining the characteristic well-ordered top surfaces of SNIPS membranes. This periodic order of the pores in the top separation layer, together with the asymmetric and simultaneously hierarchical porosity of the substructure is expected to combine high surface area with high flux. Due to the advantages of high porosity and pore accessibility as well as the scalability of the NIPS based membrane formation process, we expect these asymmetric carbon materials to find use in areas as diverse as catalysis, energy conversion and storage, and separations.

Acknowledgements

This work was funded by the National Science Foundation under award DMR-1707836. This work is based upon research conducted at the Cornell High Energy Synchrotron Source (CHESS) which is supported by the National Science Foundation under award DMR-1332208. This work made further use of the Cornell Center for Materials Research Shared Facilities which are supported through the NSF MRSEC program (DMR-1719875). P.A.B. was supported by the National Science Foundation Graduate Research Fellowship Program (DGE-1650441). S.A.H. acknowledges Wiesner Group (Cornell University) members Y. Hibi, R. P. Thedford, K. P. Barteau for help casting membranes at CHESS D1 beamline, Q. Zhang for help indexing pure ISV GISAXS patterns, and J. G. Werner for helpful discussions.

APPENDIX B

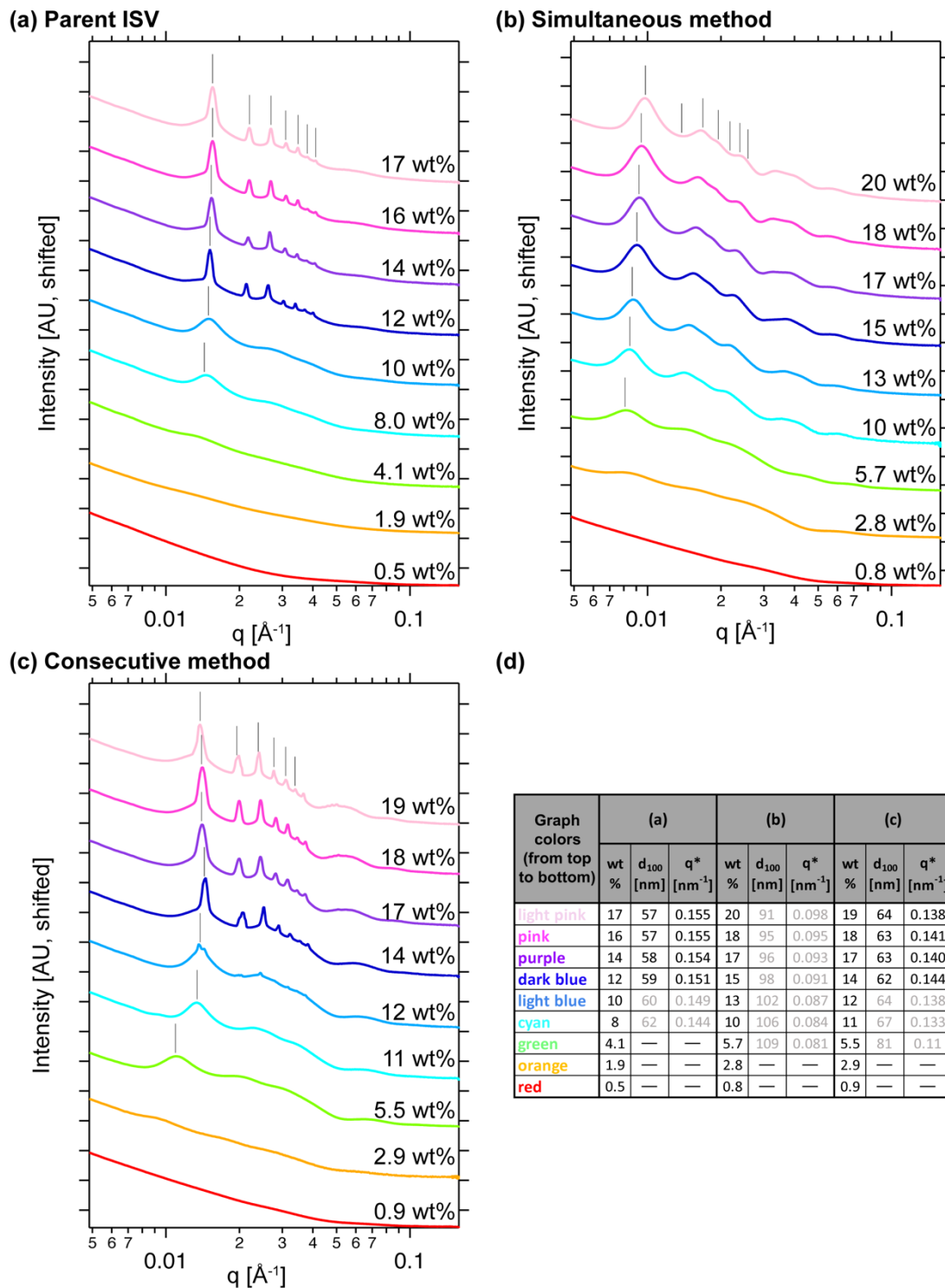


Figure S3.1. Complete small-angle x-ray scattering (SAXS) patterns of solutions of (a) parent ISV, (b) simultaneous method ISV+resols (2:1 ISV:resols by weight), and (c) consecutive method ISV+resols (2:1 ISV:resols by weight). All solutions were 7:3

DOX:THF (by weight). Tick marks indicate expected peak positions for a body-centered cubic (BCC) morphology relative to the observed primary peak. The (a) ISV concentrations and (b, c) ISV+resols concentrations are reported next to each trace, ranging from about 1 wt% to 20 wt%. (d) provides a table consistent in color coding to wt% dependent traces in a-c with the corresponding d spacings, where applicable. Light gray text marks spacings given for traces which were analyzed assuming a BCC lattice but do not show evidence of BCC ordering. These values are given merely as a reference to indicate expected lattice spacings based solely off of the primary peak.

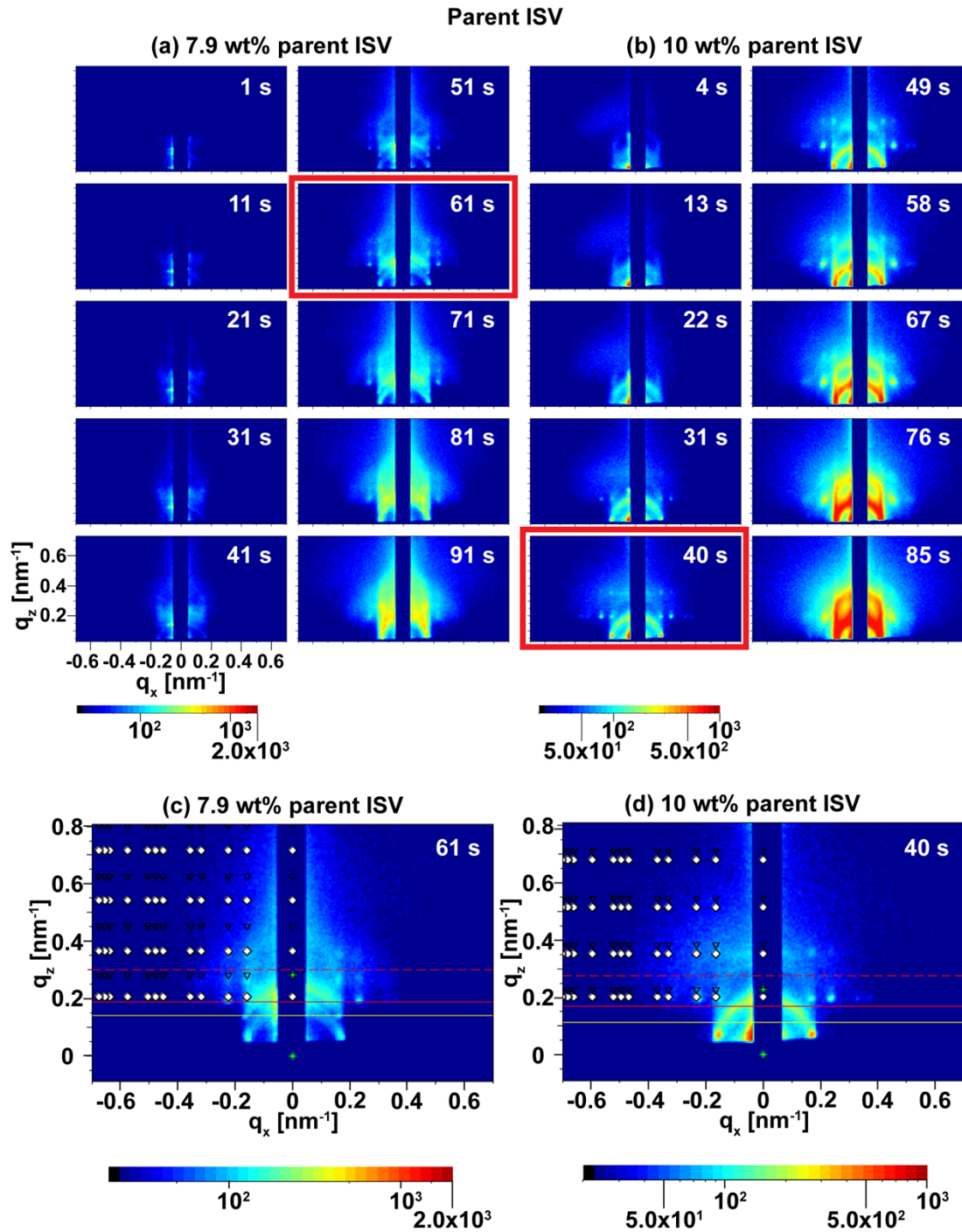


Figure S3.2. Complete *in situ* GISAXS patterns of (a) 7.9 wt% and (b) 10 wt% solutions of parent ISV terpolymer in 7:3 DOX:THF solutions cast and evaporated for varying amounts of time as indicated. The two images boxed in red in (a) and (b) were indexed in (c) and (d), respectively. Patterns were indexed to an SC lattice with the (001) plane parallel to the surface and lattice parameters of 39.5 nm and 38 nm for (c) and (d), respectively.

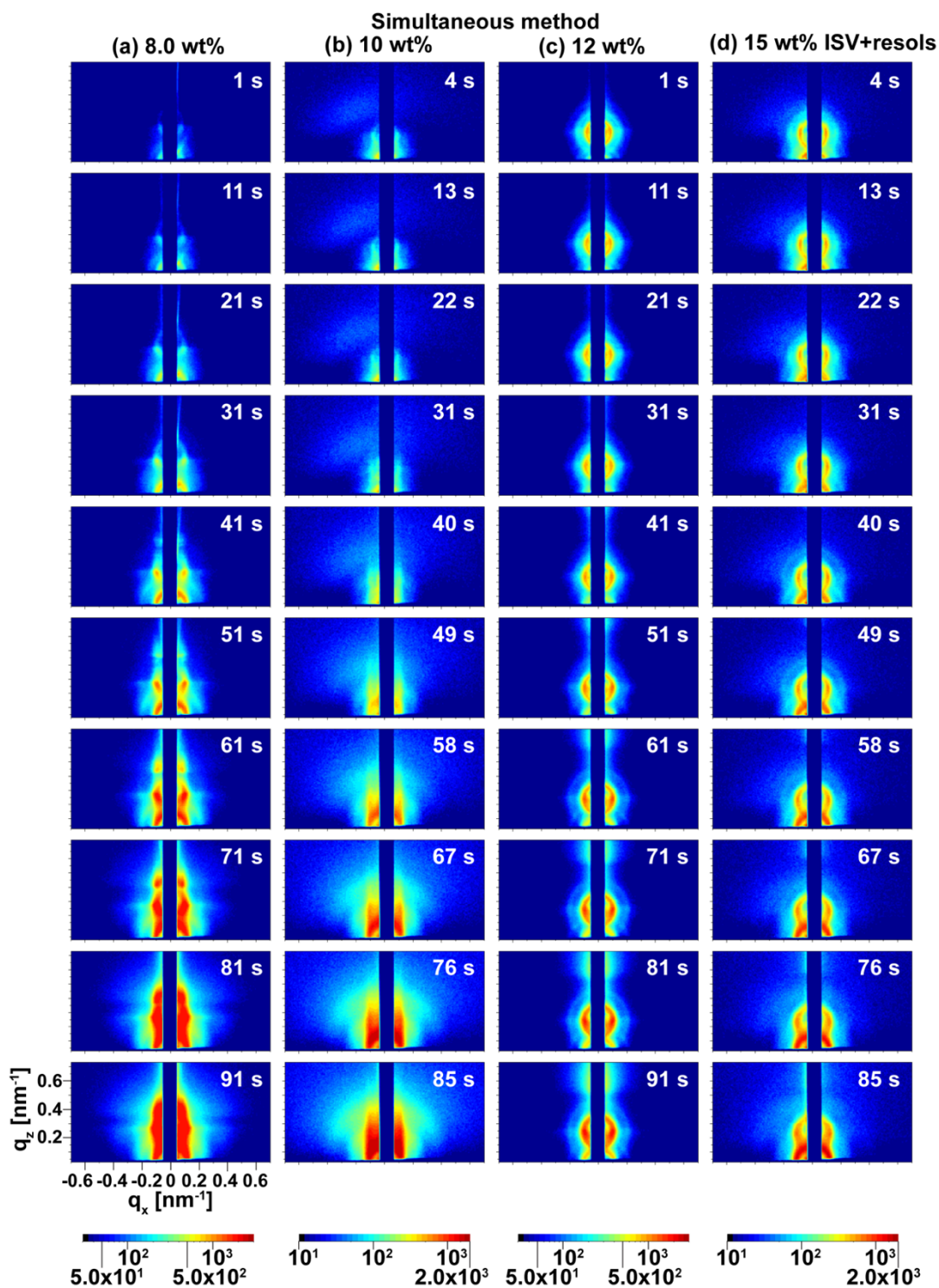


Figure S3.3. Complete *in situ* GISAXS patterns of (a) 8.0 wt%, (b) 10 wt%, (c) 12 wt%, (d) 15 wt% ISV+resols (2:1 ISV:resols weight ratio) in 7:3 DOX:THF solutions prepared *via* the simultaneous method, cast, and evaporated for varying times as indicated. Some disordered structure is evidenced by broad amorphous rings. No long-range order is evident from these diffractograms.

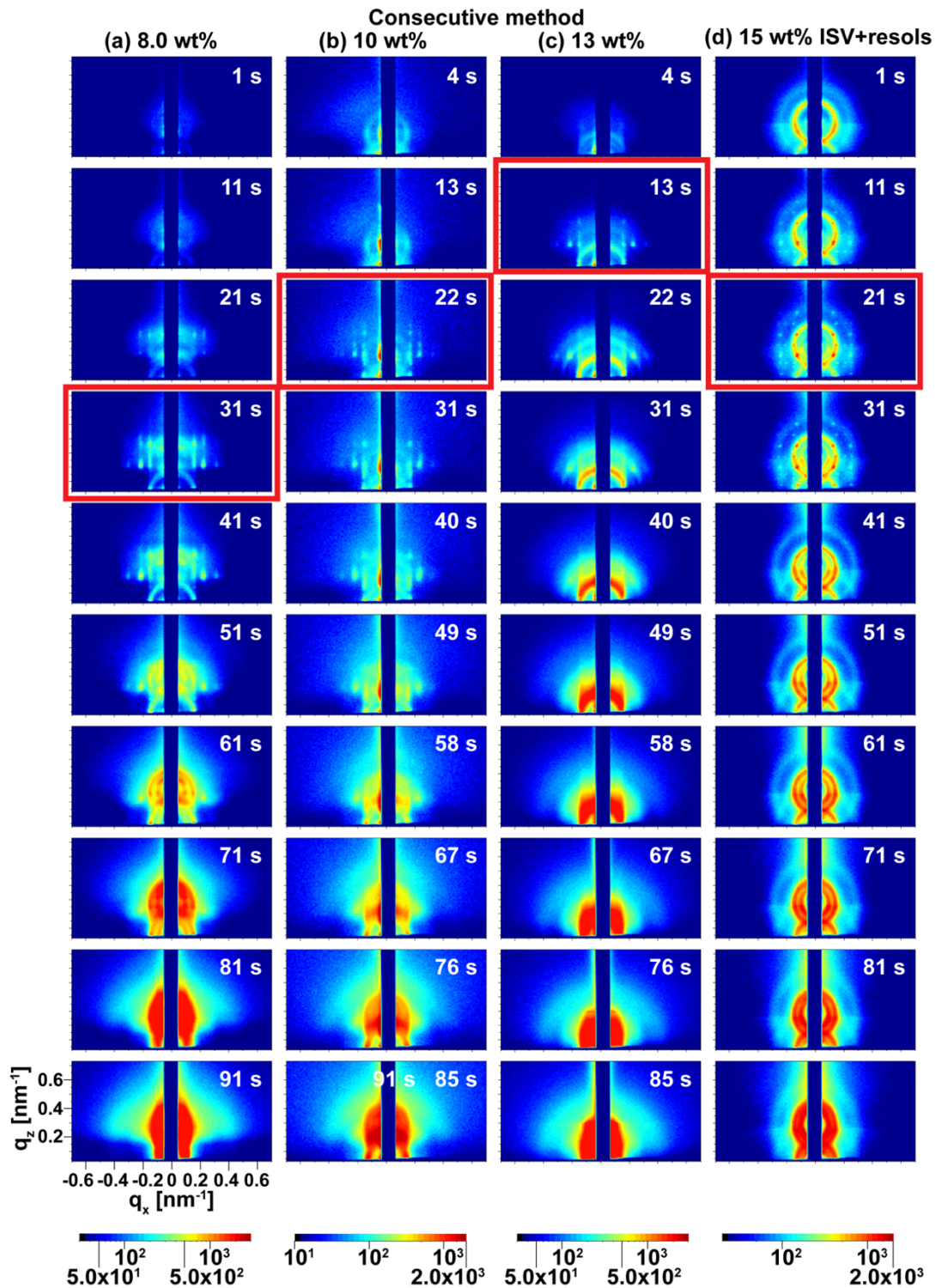


Figure S3.4. Complete *in situ* GISAXS patterns of (a) 8.0 wt%, (b) 10 wt%, (c) 13 wt%, and (d) 15 wt% ISV+resols (2:1 ISV:resols weight ratio) in 7:3 DOX:THF solutions prepared *via* the consecutive method, cast, and evaporated for varying amounts of time as indicated. The images boxed in red in (a), (b), (c), and (d) are indexed in figure S5 (a), (b), (c), and (d), respectively.

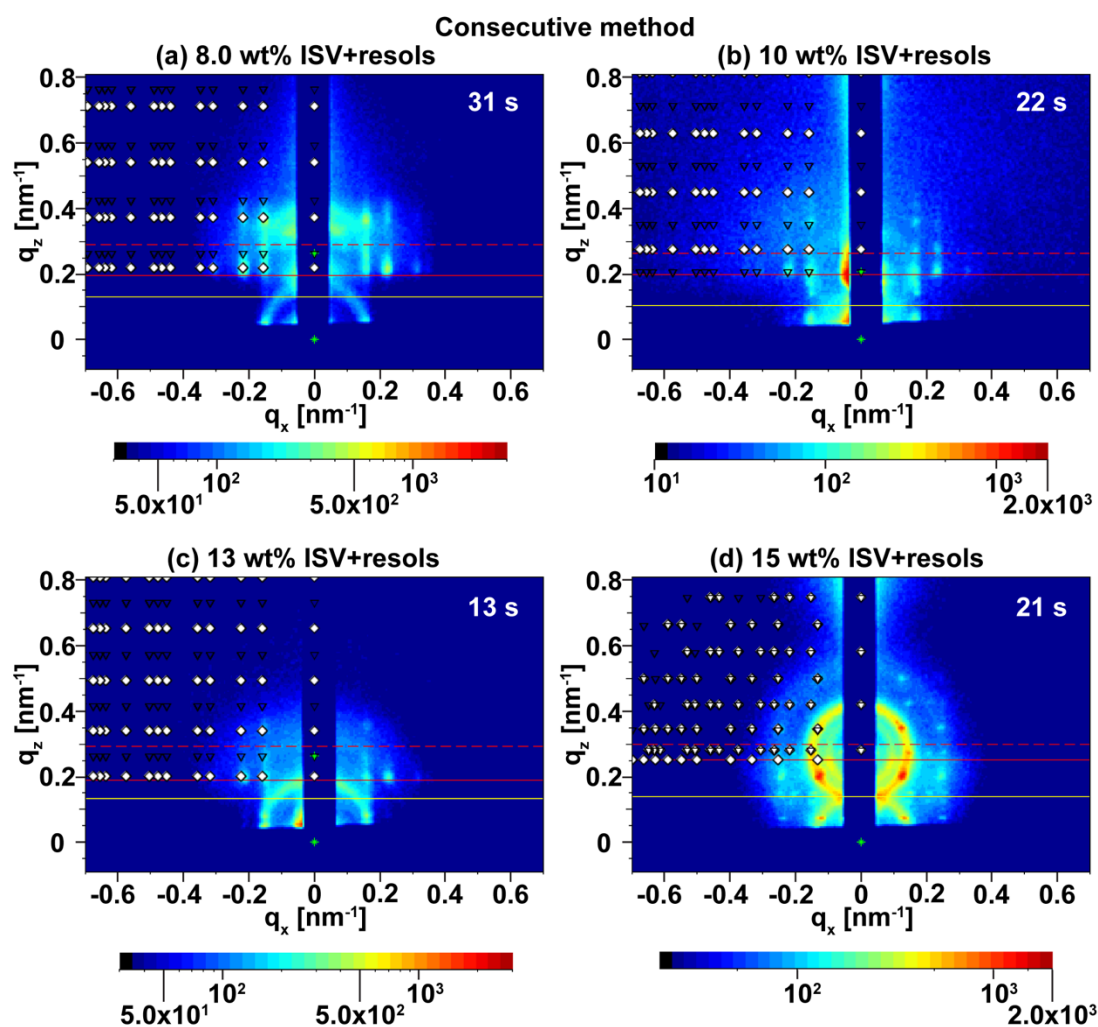


Figure S3.5. Selected *in situ* GISAXS patterns from Figure S4 of (a) 8.0 wt%, (b) 10 wt%, (c) 13 wt%, and (d) 15 wt% ISV+resols (2:1 ISV:resols weight ratio) in 7:3 DOX:THF solutions prepared *via* the consecutive method cast and evaporated for 31 s, 22 s, 13 s, 21 s, respectively. Patterns for (a), (b), and (c) were indexed to an SC lattice with the (001) plane parallel to the surface and lattice parameters of 40.5 nm, 39.5 nm, 39.5 nm, respectively. The pattern of the 15 wt% ISV+resols sample evaporated for 21 s was best indexed by a BCC lattice with the (110) plane parallel to the film surface and a lattice parameter of 58 nm.

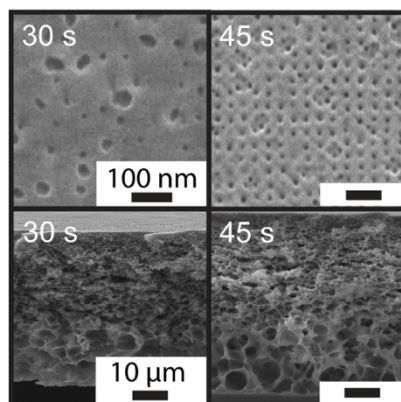
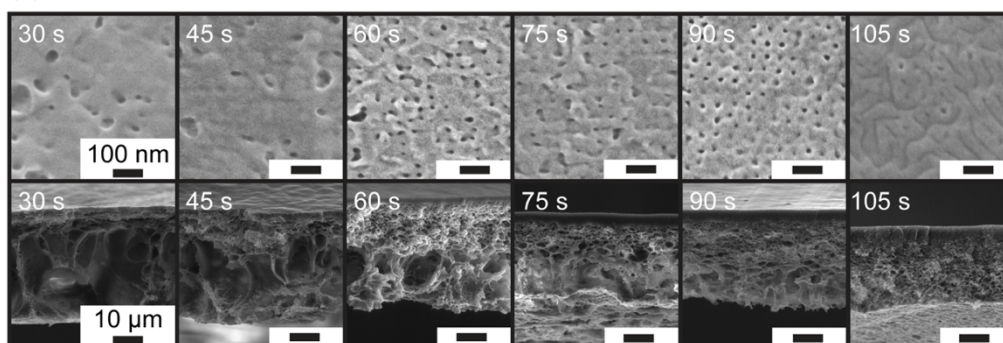


Figure S3.6. Top surface (top row) and cross-section (bottom row) SEM characterization of 9.9 wt% ISV in 7:3 DOX:THF, evaporated on a RT (~ 20 °C) substrate at low relative humidity ($< 30\%$) for 30 s (left column) and 45 s (right column), and subsequently plunged into a RT (~ 20 °C) nonsolvent DI water bath.

Consecutive method, RT substrate

(a) 10 wt% ISV+resols



(b) 15 wt% ISV+resols

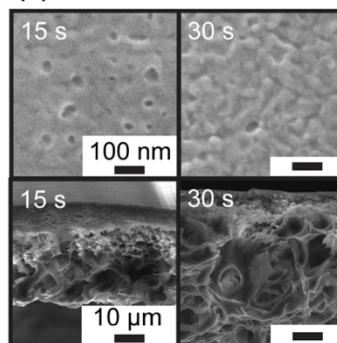


Figure S3.7. Top surface (top rows) and cross-section (bottom rows) SEM characterization of (a) 10 wt% and (b) 15 wt% ISV+resols (2:1 ISV:resols weight ratio) in 7:3 DOX:THF solutions cast via the consecutive method on a room temperature (~ 20 °C) substrate under low ($< 30\%$) relative humidity, and allowed to evaporate for various amounts of times. The films were plunged into a RT (~ 20 °C) nonsolvent DI water bath.

Consecutive method, 30 °C substrate

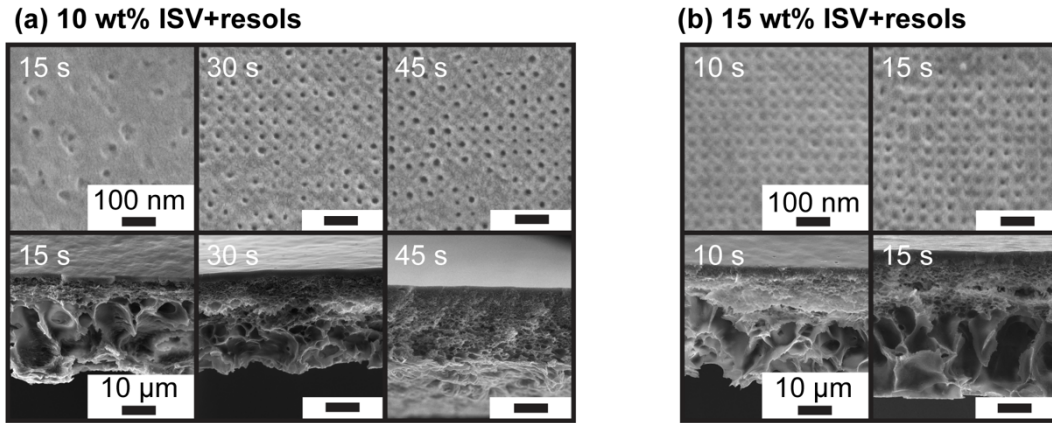


Figure S3.8. Top surface (top rows) and cross-section (bottom rows) SEM characterization of (a) 10 wt% and (b) 15 wt% ISV+resols (2:1 ISV:resols weight ratio) in 7:3 DOX:THF solutions cast *via* the consecutive method on a substrate heated to 30 °C under low (<30 %) relative humidity, and allowed to evaporate for various amounts of time. The films were plunged into a RT (~20 °C) nonsolvent DI water bath.

Simultaneous method

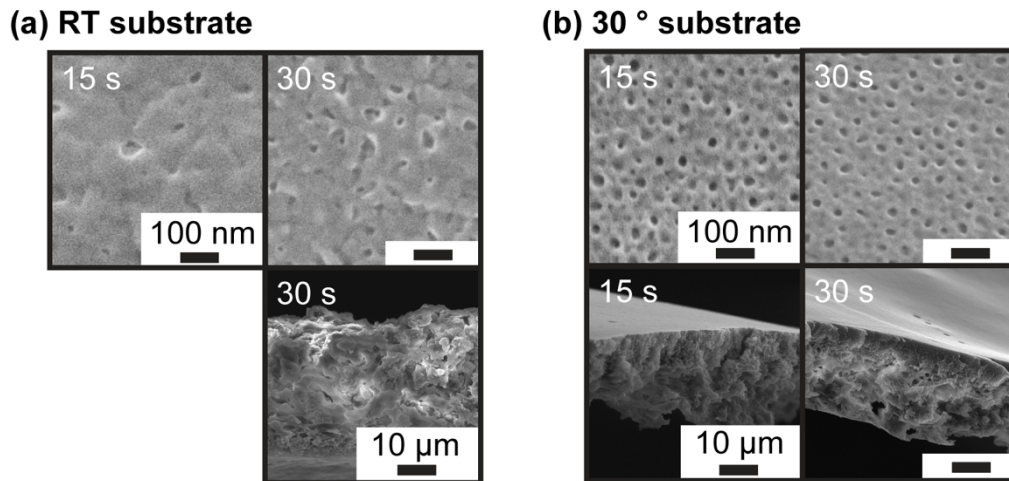
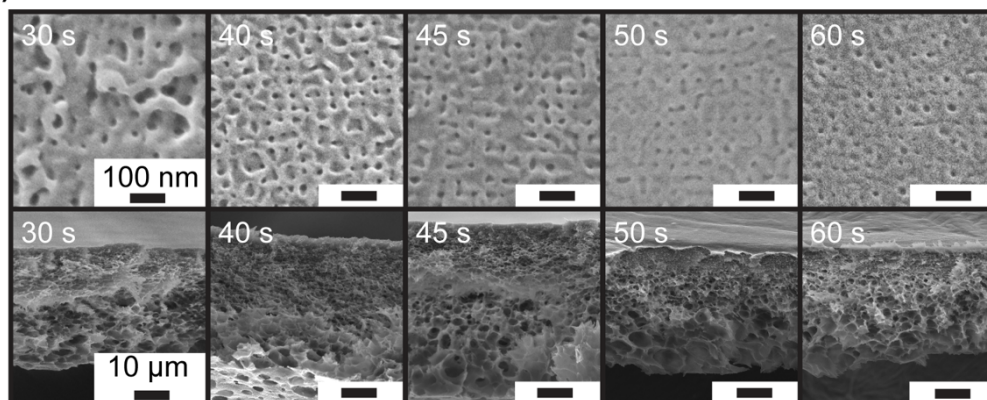


Figure S3.9. Top surface (top rows) and cross-section (bottom rows) SEM characterization of a 10 wt% ISV+resols (2:1 ISV:resols weight ratio) in 7:3 DOX:THF solution cast via the simultaneous method on (a) a RT (~20 °C) and (b) a substrate heated to 30 °C under low (<30 %) relative humidity, and allowed to evaporate for various amounts of time. The films were plunged into a RT (~20 °C) nonsolvent DI water bath.

Consecutive method

(a) RT substrate



(b) 30 °C substrate

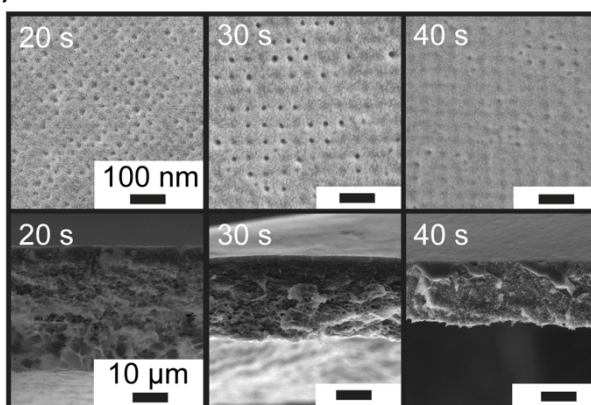


Figure S3.10. Top surface (top rows) and cross-section (bottom rows) SEM characterization of a 10 wt% ISV in 7:3 DOX:THF solution cast *via* the consecutive method under high relative humidity (~70%) on (a) a RT (~20 °C) and (b) a substrate heated to 30 °C, and allowed to evaporate for various amounts of time. The films were plunged into a RT (~20 °C) non-solvent DI water bath.

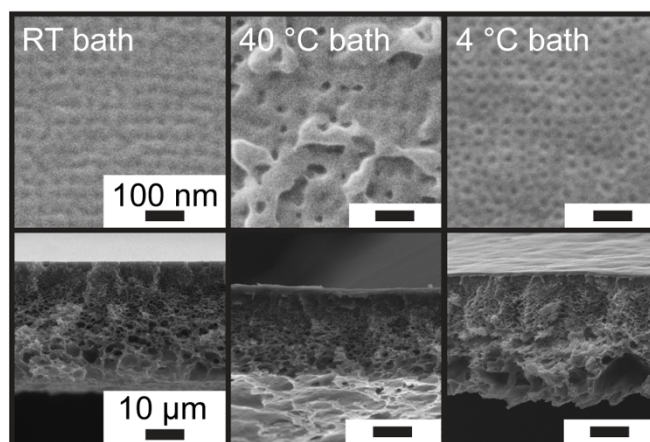


Figure S3.11. Top surface (top row) and cross-section (bottom row) SEM characterization of a 10 wt% ISV+resols (2:1 ISV:resols weight ratio) in 7:3 DOX:THF solution prepared *via* the consecutive method and cast at low (<30%) relative humidity on a 30 °C substrate and dipped into a RT (~20 °C) (left), a 40 °C (middle), and a 4 °C (right) DI water bath.

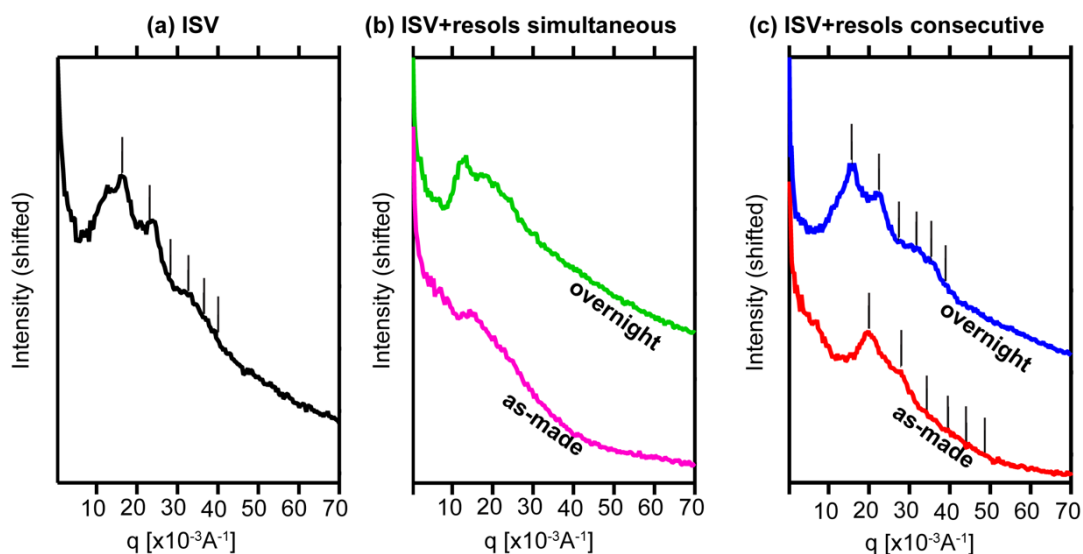


Figure S3.12. FFT analysis of SEM images of the top surface of the membranes for (a) ISV membrane, (b) ISV+resols (2:1 ISV:resols weight ratio) derived membrane from simultaneous method as-made (pink), or stirred in DI water overnight (green), (c) ISV+resols (2:1 ISV:resols weight ratio) derived membrane from consecutive method as-made (red), or stirred in DI water overnight (blue). Cubic ordering is only evident for ISV and ISV+resols consecutive method derived membranes. Tick marks indicate expected peak positions for a 2D square lattice. q^* positions yield pore-to-pore distances of 39 nm (black) for the ISV membrane, as well as 32 nm (red) and 40 nm (blue) for as-made membrane and a membrane stirred overnight in the DI water bath.

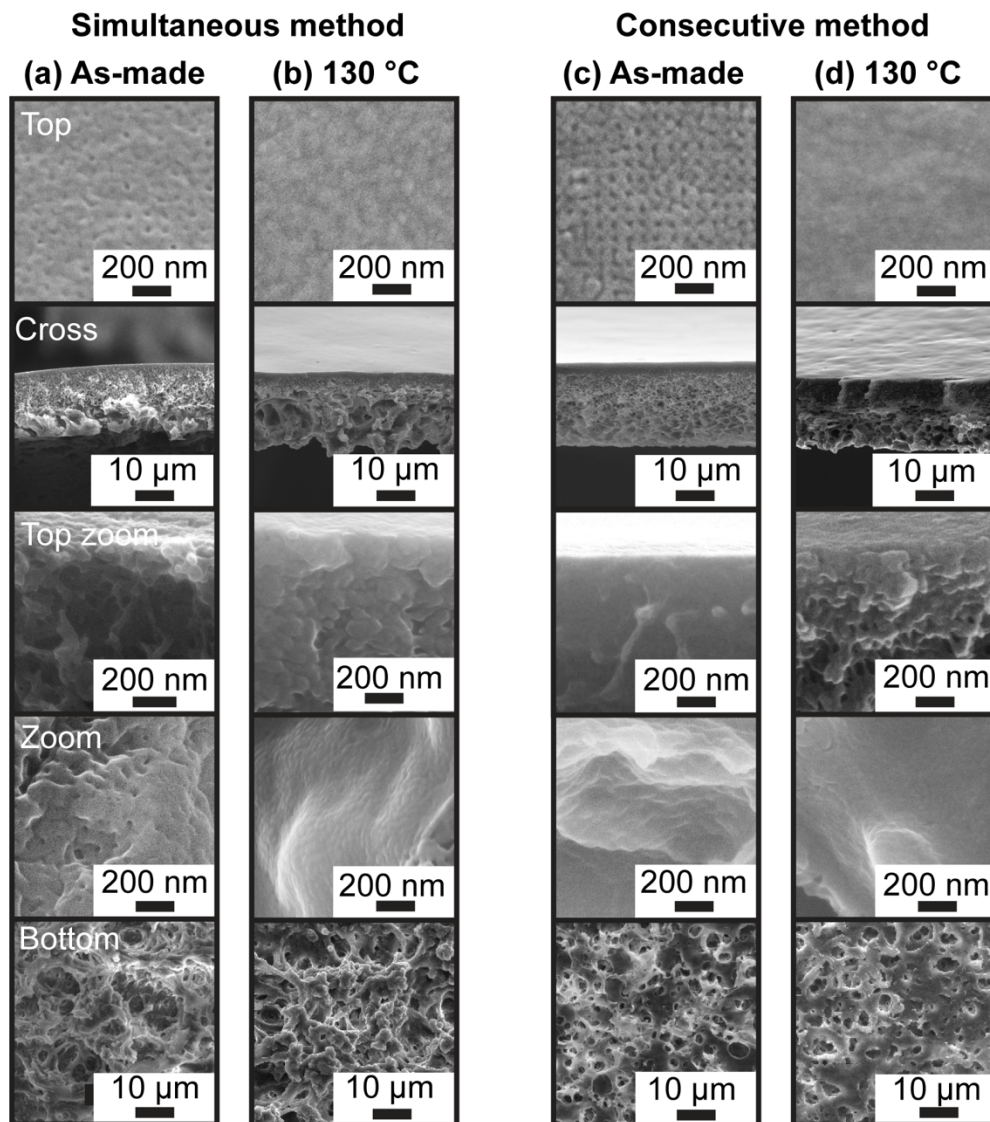


Figure S3.13. SEM characterization of (a) as-made and (b) 130 °C heat-treated membranes obtained *via* the simultaneous method from an 11 wt% ISV+resols (2:1 ISV:resols weight ratio) solution. SEM characterization of (c) as-made and (d) 130 °C heat treated membranes obtained *via* the consecutive method from a 10 wt% ISV+resols (2:1 ISV:resols weight ratio) solution. The evaporation time for all membranes was 40 s. From top to bottom: Top surface, cross-section, enlarged cross-section of mesoporous top surface, enlarged mesopores in the walls of the macroporous pockets towards the bottom membrane region, and bottom surface. Membranes were cast onto a 30 °C substrate at low relative humidity (<30%), and dipped into a RT (~20 °C) nonsolvent DI water bath.

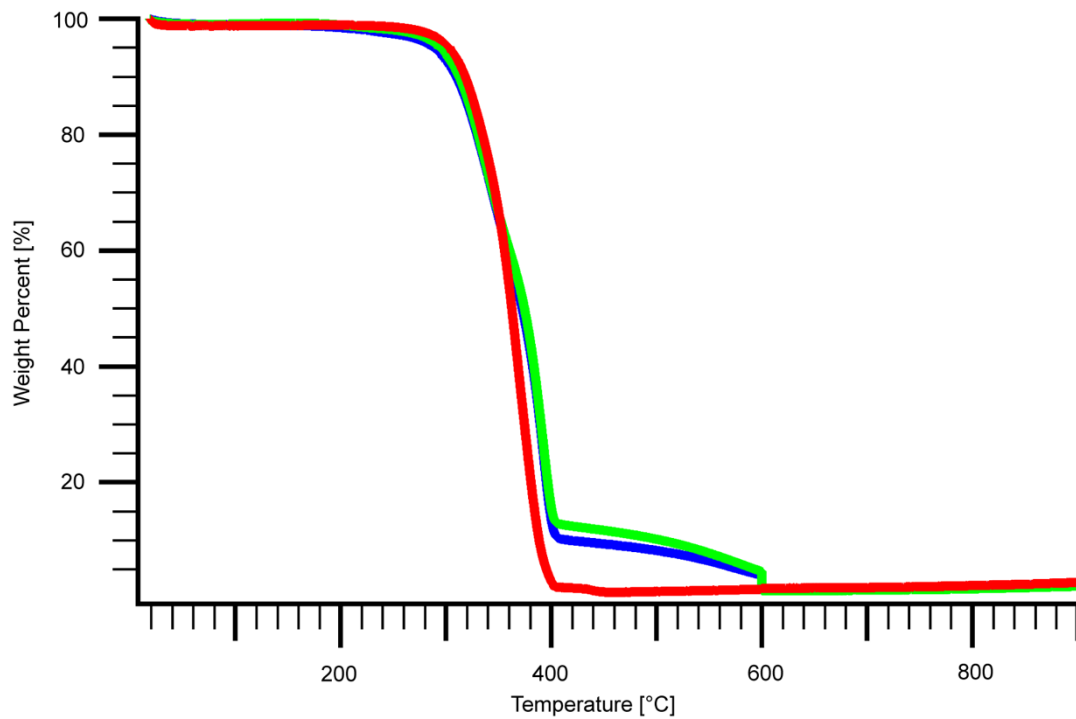


Figure S3.14. Thermogravimetric analysis (TGA) of 130 °C heat-treated ISV (red) and ISV+resols (2:1 ISV:resols weight ratio) hybrid membranes from both the simultaneous (blue) and consecutive (green) methods.

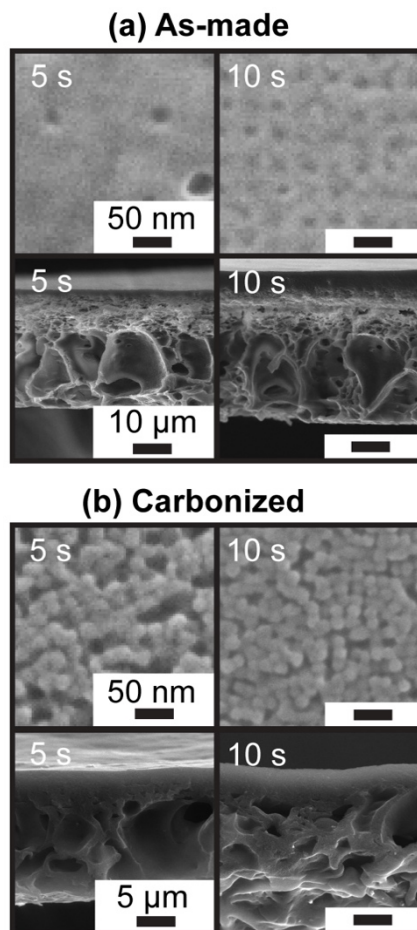


Figure S3.15. Top surface (top rows) and cross-section (bottom rows) SEM characterization of (a) as-made and (b) carbonized membranes cast from 15 wt% ISV+resols (2:1 ISV:resols weight ratio) solution made *via* the consecutive method and allowed to evaporate for two different times, as indicated. Membranes were cast at low relative humidity (<30%), onto 30 °C substrates, and plunged into RT (~20 °C) nonsolvent DI water bath.

REFERENCES

1. Rolison, D. R. *et al.* Multifunctional 3D nanoarchitectures for energy storage and conversion. *Chem. Soc. Rev.* **38**, 226–52 (2009).
2. Orilall, M. C. & Wiesner, U. Block copolymer based composition and morphology control in nanostructured hybrid materials for energy conversion and storage: solar cells, batteries, and fuel cells. *Chem. Soc. Rev.* **40**, 520–535 (2011).
3. Werner, J. G., Rodríguez-calero, G. G., Abruña, H. D. & Wiesner, U. Block Copolymer Derived Multifunctional Gyroidal Monoliths for 3-D Electrical Energy Storage Applications. *arXiv:1706.02134 [physics.chem-ph]* (2017). doi:10.1039/C7EE03571C
4. Wang, X., Li, W., Chen, Z., Waje, M. & Yan, Y. Durability investigation of carbon nanotube as catalyst support for proton exchange membrane fuel cell. *J. Power Sources* **158**, 154–159 (2006).
5. Ismail, A. F. & David, L. I. B. A review on the latest development of carbon membranes for gas separation. *J. Memb. Sci.* **193**, 1–18 (2001).
6. Werner, J. G., Rodríguez-Calero, G. G., Abruña, H. D. & Wiesner, U. Block copolymer derived 3-D interpenetrating multifunctional gyroidal nanohybrids for electrical energy storage. *Energy Environ. Sci.* **11**, 1261–1270 (2018).
7. Lee, J., Yoon, S., Hyeon, T., Oh, S. M. & Kim, K. B. Synthesis of a new mesoporous carbon and its application to electrochemical double-layer capacitors. *Chem. Commun.* **0**, 2177–2178 (1999).
8. Ryoo, R., Joo, S. H. & Jun, S. Synthesis of Highly Ordered Carbon Molecular

Sieves via Template-Mediated Structural Transformation. *J. Phys. Chem. B* **103**, 7743–7746 (1999).

9. Jun, S. *et al.* Synthesis of new, nanoporous carbon with hexagonally ordered mesostructure [5]. *J. Am. Chem. Soc.* **122**, 10712–10713 (2000).

10. Liang, C., Hong, K., Guiochon, G. A., Mays, J. W. & Dai, S. Synthesis of a large-scale highly ordered porous carbon film by self-assembly of block copolymers. *Angew. Chem. Int. Ed. Engl.* **43**, 5785–5789 (2004).

11. Tanaka, S., Nishiyama, N., Egashira, Y. & Ueyama, K. Synthesis of ordered mesoporous carbons with channel structure from an organic-organic nanocomposite. *Chem. Commun.* **0**, 2125–2127 (2005).

12. Kosonen, H. *et al.* Functional porous structures based on the pyrolysis of cured templates of block copolymer and phenolic resin. *Adv. Mater.* **18**, 201–205 (2006).

13. Werner, J. G., Hoheisel, T. N. & Wiesner, U. Synthesis and characterization of gyroidal mesoporous carbons and carbon monoliths with tunable ultralarge pore size. *ACS Nano* **8**, 731–43 (2014).

14. Gu, Y., Werner, J. G., Dorin, R. M., Robbins, S. W. & Wiesner, U. Graded porous inorganic materials derived from self-assembled block copolymer templates. *Nanoscale* **7**, 5826–5834 (2015).

15. Peinemann, K. V., Abetz, V. & Simon, P. F. W. W. Asymmetric superstructure formed in a block copolymer via phase separation. *Nat. Mater.* **6**, 992–6 (2007).

16. Dorin, R. M. *et al.* Solution Small-Angle X-ray Scattering as a Screening and Predictive Tool in the Fabrication of Asymmetric Block Copolymer Membranes. *ACS Macro Lett.* **1**, 614–617 (2012).
17. Dorin, R. M., Sai, H. & Wiesner, U. Hierarchically porous materials from block copolymers. *Chem. Mater.* **26**, 339–347 (2014).
18. Phillip, W. A. *et al.* Tuning structure and properties of graded triblock terpolymer-based mesoporous and hybrid films. *Nano Lett.* **11**, 2892–900 (2011).
19. Gu, Y., Dorin, R. M. & Wiesner, U. Asymmetric organic-inorganic hybrid membrane formation via block copolymer-nanoparticle co-assembly. *Nano Lett.* **13**, 5323–5328 (2013).
20. Hesse, S. A., Werner, J. G. & Wiesner, U. One-pot synthesis of hierarchically macro- and mesoporous carbon materials with graded porosity. *ACS Macro Lett.* **4**, 477–482 (2015).
21. Pendergast, M. M., Dorin, R., Phillip, W. A., Wiesner, U. & Hoek, E. M. V. Understanding the structure and performance of self-assembled triblock terpolymer membranes. *J. Memb. Sci.* **444**, 461–468 (2013).
22. Ilavsky, J. & Jemian, P. R. Irena: Tool suite for modeling and analysis of small-angle scattering. *J. Appl. Crystallogr.* **42**, 347–353 (2009).
23. Ilavsky, J. Nika: Software for two-dimensional data reduction. *J. Appl. Crystallogr.* **45**, 324–328 (2012).

24. Smilgies, D. M. *et al.* Look fast: Crystallization of conjugated molecules during solution shearing probed in-situ and in real time by X-ray scattering. *Phys. Status Solidi - Rapid Res. Lett.* **7**, 177–179 (2013).
25. Gu, Y., Dorin, R. M., Tan, K. W., Smilgies, D. M. & Wiesner, U. In Situ Study of Evaporation-Induced Surface Structure Evolution in Asymmetric Triblock Terpolymer Membranes. *Macromolecules* **49**, 4195–4201 (2016).
26. Smilgies, D. M. & Blasini, D. R. Indexation scheme for oriented molecular thin films studied with grazing-incidence reciprocal-space mapping. *J. Appl. Crystallogr.* **40**, 716–718 (2007).
27. Busch, P., Rauscher, M., Smilgies, D. M., Posselt, D. & Papadakis, C. M. Grazing-incidence small-angle X-ray scattering from thin polymer films with lamellar structures - The scattering cross section in the distorted-wave Born approximation. *J. Appl. Crystallogr.* **39**, 433–442 (2006).
28. Brunauer, S., Emmett, P. H. & Teller, E. Adsorption of Gases in Multimolecular Layers. *J. Am. Chem. Soc.* **60**, 309–319 (1938).
29. Sing, K. S. W. *et al.* Reporting Physisorption Data for Gas/Solid Systems With Special Reference to the Determination of Surface Area and Porosity (Recommendations 1984). *Pure Appl. Chem.* **57**, 603–619 (1985).
30. Barrett, E. P., Joyner, L. G. & Halenda, P. P. The Determination of Pore Volume and Area Distributions in Porous Substances. I. Computations from Nitrogen Isotherms. *J. Am. Chem. Soc.* **73**, 373–380 (1951).

31. Dorin, R. M. *et al.* Designing block copolymer architectures for targeted membrane performance. *Polymer (Guildf)*. **55**, 347–353 (2014).
32. Yoneda, Y. Anomalous surface reflection of X rays. *Phys. Rev.* **131**, (1963).

CHAPTER 4

ASYMMETRIC PORE ARCHITECTURE IMPROVES MASS TRANSPORT AND INTERNAL AREA UTILIZATION OVER CONVENTIONAL UNIFORM PORE ARCHITECTURES

Abstract

Porous materials design often faces a tradeoff between the requirements of high internal surface area and high flux. Asymmetric structures with continuous porosity gradients offer a potential solution to overcome this tradeoff. Borrowing self-assembly and industry-proven non-solvent induced phase separation from polymer and membrane science we obtain asymmetric porous titanium nitride (TiN) and carbon materials that are conducting (TiN, carbon) or superconducting (TiN). Their mesoporous top surface layer merges into a substructure with graded porosity evolving into bottom macropores. Compared to conventional mesoporous materials, the faster diffusion through asymmetric TiN as an electrochemical double-layer capacitor provides a $\sim 2x$ improvement in capacity retention at high scan rates, resulting in state-of-the-art power density (112.9 kW kg^{-1}) at competitive energy density (7.3 W-h kg^{-1}). For asymmetric carbon, we report a record setting power density ($1151.5 \text{ kW kg}^{-1}$) at 14.5 W-h kg^{-1} . Results on non-optimized materials suggest that asymmetric structures may benefit a number of energy storage and conversion applications.

Sarah A. Hesse*, Kevin E. Fritz*, Peter A. Beaucage, R. Paxton Thedford, F. Yu, Francis J. DiSalvo, Jin Suntivich, Ulrich Wiesner. *To be submitted for publication.*

Main Text

In energy storage, the ability to prepare mesoporous materials with small, interconnected pores has resulted in remarkable improvements in power^{1,2} and energy density^{3,4}. Still, at fast rates, only a small fraction of the pores are accessible. This results in pore underutilization, which creates a tradeoff between energy density and rate capability (*i.e.*, power density) in energy storage devices such as batteries and capacitors.⁵⁻¹² Even for electrochemical double-layer capacitors (EDLCs), a device known for high power density, the energy density drops precipitously at high rate operation.

Nature uses asymmetric structures to address the tradeoff between requirements for high internal surface area and high flux. For example, the respiratory system (Figure 4.1a) uses airflow through the trachea (diameter of ~1.5-2.5 cm) and bronchi (diameter of ~0.4 mm) to the alveoli (diameter of ~50-250 μm) in order to allow high flux while simultaneously providing large surface area for O_2/CO_2 exchange. Creating engineered asymmetric porous inorganic structures requires non-equilibrium processes, which has remained challenging. For example, in conventional block copolymer (BCP) self-assembly (SA) directed porous inorganic materials formation, equilibrium conditions dictate that pore sizes are homogeneous throughout the material.^{13,14} To overcome this limitation, we combine three different processes: Inorganic materials formation, BCP SA, and a widely used and scalable industrial membrane formation process referred to as nonsolvent induced phase separation (NIPS).¹⁵ The combination of BCP SA and NIPS (SA+NIPS=SNIPS) has provided a paradigm shift in the ability to

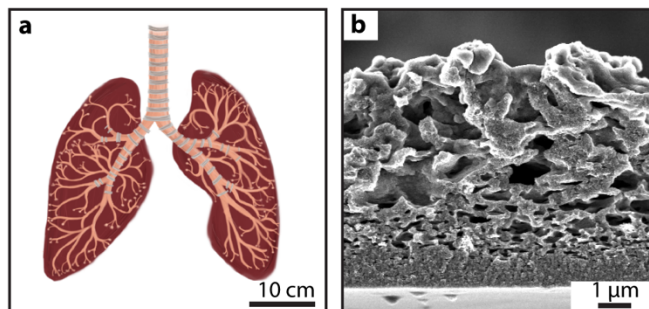


Figure 4.1. Asymmetric structures used for high flux/accessibility are common in nature. In this work, we utilize this concept to improve internal transport in porous materials. (a) The asymmetric structure of the respiratory system: air flows from the trachea ($\varnothing \sim 1.5\text{-}2.5\text{ cm}$) to the bronchi ($\varnothing < 1.5\text{ cm}$) to the smaller bronchioles ($\varnothing \sim 1.0\text{ cm}$) and ends up in the alveoli ($\varnothing < 0.2\text{ mm}$). (b) The asymmetric structure of the engineered material: reactants (e.g., liquids, ions, and gases) can travel from large macropores ($\varnothing \sim 60\text{ }\mu\text{m}$) to smaller macropores ($\varnothing \sim 0.5\text{ }\mu\text{m}$), and finally to mesopores ($\varnothing \sim 10\text{ nm}$).

generate high flux and high resolution asymmetric ultrafiltration (UF) membranes.^{16,17}

Here we translate this success to the direct formation of asymmetric porous nitride and carbon structures (Figure 4.1b) and demonstrate that they can enhance mass transport of ions in EDLCs and allow for high rate capability without compromising on available surface area inside the materials. Titanium nitride (TiN) is an ideal candidate for aqueous EDLCs, owing to its high conductivity and corrosion resistance.¹⁸ For comparison, we synthesize asymmetric graphitic carbon and measure its capacitive performance as carbon is an industry standard for high-energy-density EDLCs. In order to characterize the effect of the asymmetric morphology on transport, we compare asymmetric TiN to an ordered, mesoporous TiN monolith mimicking conventional mesoporous materials used in EDLC applications.

Figure 4.2 shows the overall synthesis flow. Briefly, a triblock terpolymer

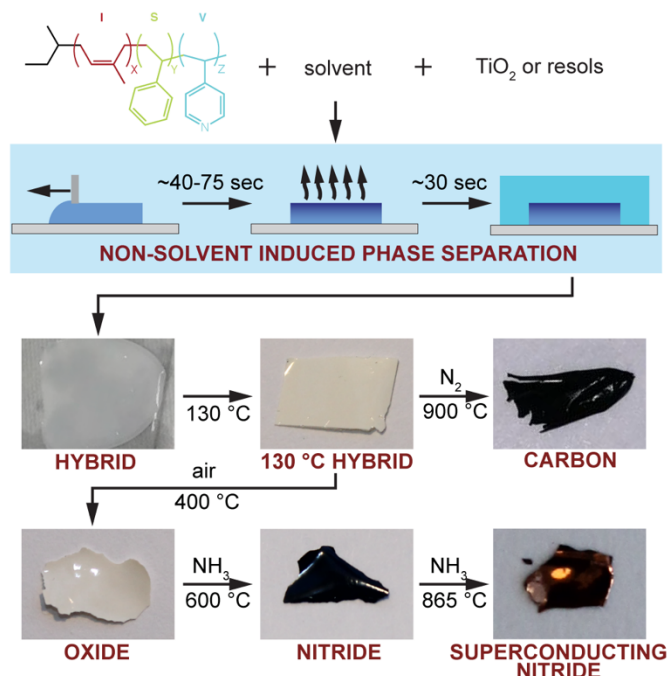


Figure 4.2. Schematic representation of SNIPS process and heat-treatment. The casting solutions, consisting of the ISV terpolymer mixed with either TiO_2 sol NPs or resols, was cast onto glass slides to form $\sim 200\text{-}400\ \mu\text{m}$ thick films. After allowing the films to partially evaporate to induce an ISV+additive concentration gradient, they were plunged into a DI water bath, precipitating the polymer and converting the concentration gradient into an asymmetric composite structure. The resulting membranes were dried at RT and $130\ \text{°C}$. The ISV+resols hybrids were heated to $900\ \text{°C}$ in inert atmosphere (N_2) leading to ISV decomposition and resulting in graphitic carbon. The ISV+ TiO_2 hybrids were heat-treated in air ($400\ \text{°C}$). This led to polymer decomposition and formation of freestanding anatase titanium (IV) oxide. The oxide was then subjected to heat-treatment in ammonia ($600\ \text{°C}$) to form TiN. A second heat-treatment in ammonia ($865\ \text{°C}$) led to TiN superconductors. Photographs of the materials at each synthetic step are shown at the bottom.

poly(isoprene)-*block*-poly(styrene)-*block*-poly(4-vinylpyridine) (ISV) was used as the amphiphilic BCP to structure-direct either inorganic titanium dioxide (TiO_2) sol-gel derived nanoparticles (NPs) or organic phenol formaldehyde resols (resols). The inorganic/organic additive preferentially swells the hydrophilic V block of ISV.^{19,20} ISV was synthesized *via* sequential anionic polymerization.²¹ For the nitrides/graphitic carbons, ISVs of molar mass $113/95\ \text{kg mol}^{-1}$ with 29/29 vol% poly(isoprene) (PI),

59/57 vol% poly(styrene) (PS), 12/14 vol% poly(4-vinylpyridine) (P4VP) and polydispersity index (PDI) of 1.3/1.2 were used to structure-direct TiO₂ NPs or resols, respectively. The TiO₂ NPs were prepared from a modified hydrolytic sol-gel synthesis, while resols were synthesized *via* condensation of phenol and formaldehyde under basic conditions.^{22,23}

Solutions consisting of homogeneous mixtures of ISV and either TiO₂ NPs or resols dissolved in 1,4-dioxane (DOX) and tetrahydrofuran (THF) were cast onto glass slides using a doctor blade with a predetermined gate height on the order of a few hundred microns. Films were allowed to evaporate for a set amount of time *via* the film surface which introduced an ISV+additive concentration gradient along the film normal. Evaporation was halted by plunging the films into a nonsolvent, here deionized (DI) water, to precipitate ISV, thus freezing-in the asymmetric structure. Subsequent drying and heat treatments, first at 130 °C (Figure S4.1) and then higher temperatures as shown in Figure 2, converted the as-made composite materials into the final asymmetric inorganic porous structures.

Following heat treatment at 130 °C, ISV+TiO₂ hybrids were taken to 400 °C in air for 3 h to produce porous freestanding asymmetric TiO₂. The scanning electron micrograph (SEM), X-ray diffraction (XRD), and nitrogen sorption characterization for a representative material are provided in Figure S4.2. Heating in air generated porous TiO₂ by removing organic material without losing the asymmetric structure. From XRD (Figure S2g), the peaks were consistent with an anatase phase TiO₂ (ICSD #01-070-7348) which crystallized in space group I41/amd (#141) with lattice parameters of $a = b = 3.79$ Å and $c = 9.52$ Å, and a grain size from Debye-Scherrer analysis of 12.1 nm. These lattice

parameters are comparable to those reported for bulk anatase TiO_2 ($a = b = 3.785 \text{ \AA}$, $c = 9.514 \text{ \AA}$),²⁴ while the grain size is on the order of the strut thickness. Results of nitrogen sorption as well as XRD characterization for all materials in this study are summarized in Table S4.1 and S4.2, respectively. The oxide was converted into free-standing TiN by heat treatment to $600 \text{ }^\circ\text{C}$ in flowing ammonia for 6 h before allowing the sample to cool to room temperature. For asymmetric carbon, heat treatment at $130 \text{ }^\circ\text{C}$ of casted ISV+resols membranes induced cross-linking of the oligomeric resols. ISV+resols hybrids were subsequently heated to $900 \text{ }^\circ\text{C}$ in flowing nitrogen, decomposing the polymer and producing free-standing asymmetric carbons.

Characterization results for the final TiN and carbon structures *via* SEM, XRD, and nitrogen sorption are shown in Figure 4.3. By varying dope solution parameters, *e.g.* film thickness and/or evaporation time, the cross-sections and thereby surface area accessibility of the materials could be tuned. For TiN, gate heights of 305-381 μm and evaporation times of 60 s resulted in asymmetric cross-sections with fingerlike profiles (Figure 4.3a). Increased evaporation time of 75 s resulted in somewhat denser cross-sections with larger diameter macropores (Figure 4.3b), as increased solvent evaporation leaves behind a higher concentration film for precipitation. The final asymmetric TiN was considerably thinner ($\sim 60 \text{ }\mu\text{m}$) than the original hybrid ($\sim 100 \text{ }\mu\text{m}$, Figure S4.1), due to substantial mass loss from decomposition of the organics. Asymmetric carbon products had thinner cross-sections ($\sim 8 \text{ }\mu\text{m}$) due to smaller casting gate heights of 203-229 μm . By

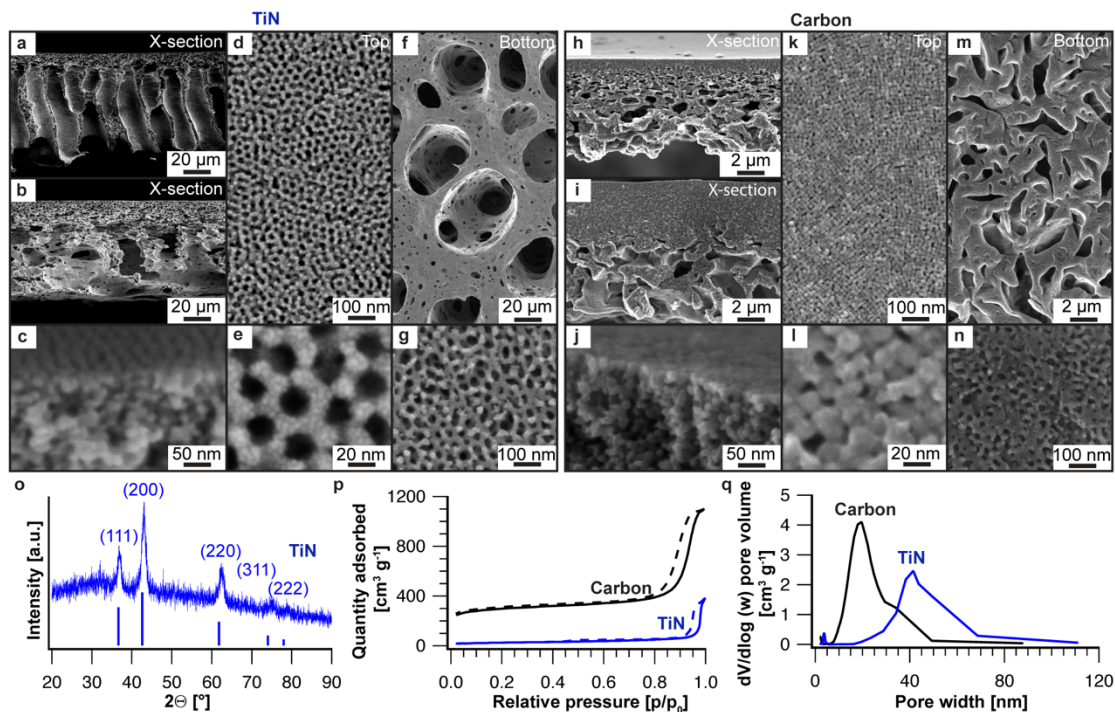


Figure 4.3. Characterization of asymmetric TiN and carbon. SEM characterization of (a-g) asymmetric TiN: (a) and (b) two different types of asymmetric TiN cross-sections; (c) the top ~ 150 nm mesoporous part of the cross-section; (d), (e) the mesoporous top surface; (f) the bottom surface showing macropores; (g) the mesoporous wall. SEM characterization of (h-n) asymmetric carbon: (h), (i) two different types of asymmetric carbon cross-sections; (j) the top ~ 150 nm mesoporous part of the cross-section; (k), (l) the mesoporous top surface; (m) the bottom surface showing macropores; (n) the mesoporous wall. (o) XRD pattern of TiN. Blue tick marks indicate expected peak positions and relative intensities for cubic TiN (Fm-3m, space group # 230, ICSD #00-038-1420). (p) Nitrogen sorption isotherms of TiN (blue) and carbon (black) materials. (q) BJH derived pore size distributions of the TiN (blue) and carbon (black) materials.

varying the solution preparation, cross-sections could be varied from a more asymmetric structure with a continuous gradient along the film normal (Figure 4.3h) to one with a denser top layer atop a macroporous substructure (Figure 4.3i).

Characterization details of the TiN sample in Figure 4.3b are provided in Figure 4.3c-g and 4.3o-q, while those of the sample depicted in Figure 4.3a are provided in Figure S4.3a-f and S4.3m. Similarly, details of the carbon sample whose cross-section is

shown in Figure 4.3i is provided in Figure 4.3j-n and 4.3p,q, while those of the sample shown in Figure 4.3h are provided in Figure S4.3g-l and S4.3n,o. The top ~ 150 nm of the cross-sections for both TiN and carbon asymmetric structures (Figure 4.3c and 4.3j) showed evidence of mesoporosity and mesoscale ordering. For TiN, surface pores were arranged in a hexagonal structure (Figure 4.3d and e), consistent with the ISV+TiO₂ hybrid (Figure S4.1). For asymmetric carbon, the top surface showed a more cubic pore arrangement (Figure 4.3k, l), reflecting the cubically packed pores of the hybrid material (Figure S4.1). For both TiN (Figure 4.3f) and carbon (Figure 4.3m), bottom surfaces exhibited micron-sized macropores. Furthermore, for both materials the walls of the macropores were mesoporous (Figure 4.3g, 4.3n), which contributed to the specific surface area (*vide infra*).

XRD characterization of the TiN (Figure 4.3o) was consistent with cubic rocksalt TiN (ICSD #00-038-1420), which crystallized in space group Fm-3m (#225) with a lattice parameter of 4.20 Å and a coherent scattering domain size of 6.9 nm from Debye-Scherrer analysis. The lattice parameter is below the reported literature values, which lie between 4.235 Å and 4.242 Å,^{25,26} but comparable to previously reported BCP-derived mesoporous TiN.¹⁸ We attribute this difference to residual oxygen content and anion vacancies as described in previous studies.^{18,25,27,28}

The porosity of asymmetric TiN and carbon samples was characterized *via* nitrogen sorption isotherms analyzed using the Brunauer-Emmett-Teller (BET) method (Figure 4.3p). In both cases, type-IV curves with H₁-type hysteresis and sharp capillary condensation above relative pressures of 0.99 were observed. For TiN, a BET surface area of 90 ± 3.0 m² g⁻¹, a micropore area of 15 m² g⁻¹, and a specific pore volume of 0.59

$\text{cm}^3 \text{g}^{-1}$ at $p/p_0=0.99$ were obtained. This surface area is similar to previously reported surface areas for mesoporous TiN, consistent with the mesoporous walls of the asymmetric material (*vide supra*).¹⁸ BJH analysis (Figure 4.3q) revealed a pore size distribution that peaked at 41 nm with a FWHM of 17 ± 7 nm, similar to the oxide precursor (Figure S4.2i). In comparison, asymmetric carbon had a much higher surface area due to increased microporosity and lower density. A BET surface area of $1024 \pm 142 \text{ m}^2 \text{ g}^{-1}$, micropore area of $655 \text{ m}^2 \text{ g}^{-1}$, and specific pore volume of $1.69 \text{ cm}^3 \text{ g}^{-1}$ at $p/p_0=0.99$ were obtained. BJH analysis (Figure 4.3q) showed a pore size distribution that peaked at 20 nm with a FWHM of 12 ± 5 nm.

To evaluate ionic diffusion inside the asymmetric morphology, we compared the electrochemical performance of asymmetric TiN with a BCP-directed homogeneous porous TiN morphology with the most accessible mesopores, *i.e.* the three-dimensional alternating gyroid structure with interconnected pores.^{22,29} Gyroidal mesoporous TiN was synthesized using evaporation induced BCP-directed self-assembly (EISA) to closely match features of the asymmetric TiN in terms of thickness, pore size distribution, and specific surface area. Synthetic details are described in the Methods section. The ordered mesostructure was confirmed using small angle x-ray scattering (SAXS) and SEM (Figure S4.4). The SAXS pattern could be indexed to an alternating gyroid (q214) structure with d_{100} unit cell size of 38 nm. The porosity was characterized using nitrogen sorption. Type-IV curves with H_1 -type hysteresis and sharp capillary condensation above relative pressures of 0.99 were observed. A BET surface area of $139 \text{ m}^2 \text{ g}^{-1}$ with a weighing error of $2.1 \text{ m}^2 \text{ g}^{-1}$, micropore area of $34 \text{ m}^2 \text{ g}^{-1}$, and specific pore volume of $1.29 \text{ cm}^3 \text{ g}^{-1}$ at $p/p_0=0.99$ were observed with a peak in the pore size distribution around 24 nm with a

FWHM of 4.2 nm, consistent with SEM results (Figure S4.4b-c). From pore size distribution analysis, pores of the gyroidal mesoporous TiN were on average slightly smaller than those of the asymmetric TiN. Hence, the BET surface area of the mesoporous TiN was higher (139 *vs.* 90 m² g⁻¹). XRD suggested mesoporous TiN crystallized with a rocksalt structure (ICSD #00-038-1420) and a lattice parameter of 4.20 Å with a grain size, determined from Debye-Scherrer analysis, of 5.5 nm, similar to the asymmetric TiN.

Cyclic voltammetry (CV) was conducted in aqueous 0.1 M HClO₄ to compare ion diffusion in the asymmetric TiN monolith with gyroidal mesoporous TiN. Measured currents were normalized to the respective BET surface areas to normalize the response of both the asymmetric and mesoporous TiN to their internal surface areas. At slow scan rates (50 mV s⁻¹), CVs of both morphologies showed similar capacitive current and specific capacitance, indicating that ion diffusion is sufficiently fast with respect to the charge/discharge rate (Figure 4.4a). At high scan rates (5 V s⁻¹), however, the capacitive performance of the two morphologies diverged substantially (Figure 4.4b). While the CV for asymmetric TiN showed a similar shape to the one at slower scan rate, mesoporous TiN showed substantial capacitance loss (~60% *vs.* ~30% initial value retention, see Figure 4.4d, 4.5b). We note that because mesoporous TiN had a higher BET area than the asymmetric TiN, the gravimetric (mass-normalized) capacitance was higher

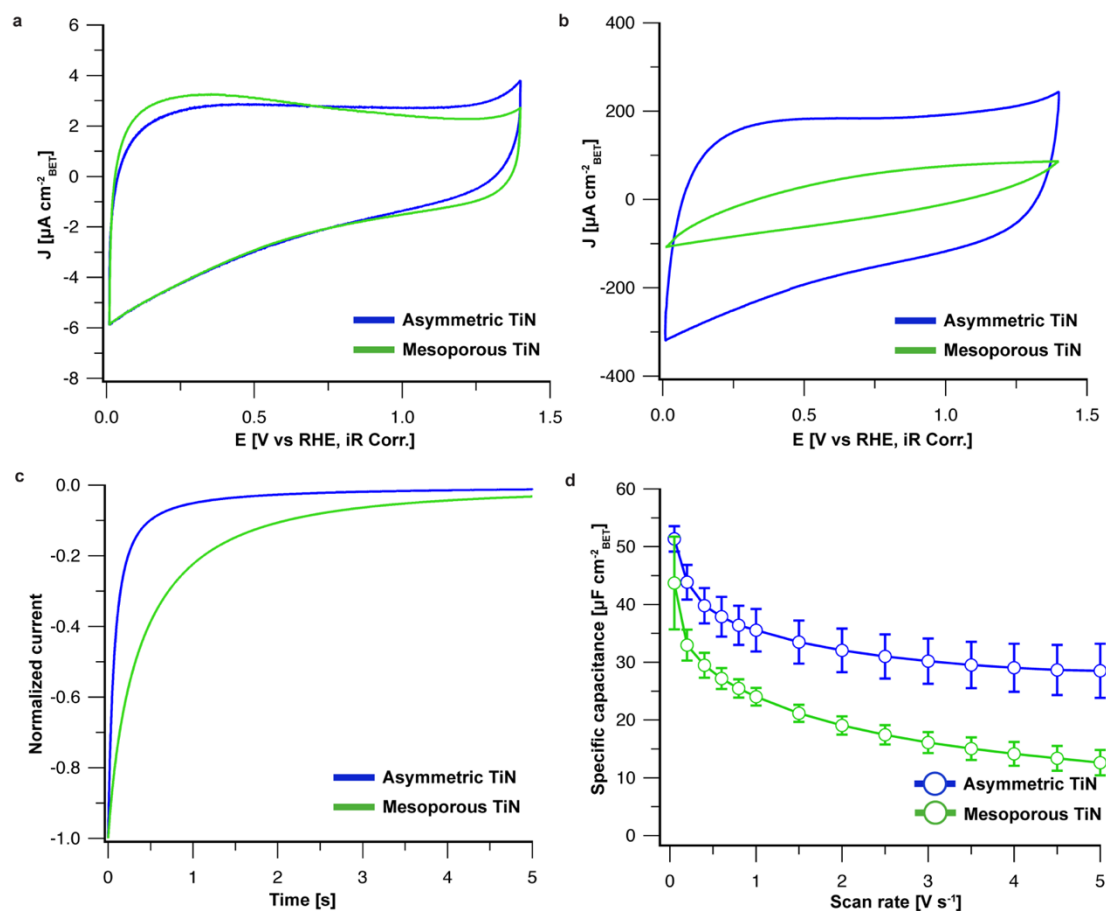


Figure 4.4. Electrochemical characterization of asymmetric TiN and gyroidal mesoporous TiN. Cyclic voltammograms for asymmetric TiN (blue) and mesoporous TiN (green) at (a) 50 mV s⁻¹ and (b) 5 V s⁻¹. (c) Chronoamperometry starting from the open circuit voltage to 0.01 V vs. RHE showing enhanced ion diffusion in asymmetric TiN. (d) Scan rate dependence of specific capacitance for asymmetric TiN (blue) and mesoporous TiN (green) showing improved surface accessibility for asymmetric TiN. Error bars represent the standard deviation of three independent trials. All results were collected in Ar-saturated 0.1 M HClO₄.

at slow scan rate; however, the trend was reversed at higher scan rate because the asymmetric TiN has a better rate capability (2x at 5 V s⁻¹, see Figures S4.5, S4.6). We emphasize that in order to allow a fair comparison of surface area accessibility in asymmetric and mesoporous TiN, the solution resistance was corrected using the high frequency intercept from impedance measurements and compensated (since the absolute

surface areas of the two morphologies were not the same). The trend of improved capacitance retention in the asymmetric structure persisted even if we did not apply this correction (Figure S4.7).

To understand the origin of the capacitance retention in asymmetric TiN, chronoamperometry (CA) was used (Figure 4.4c). In this experiment, the voltage was held at the open-circuit voltage (~ 0.65 - 0.75 V vs reversible hydrogen electrode (RHE)) for five minutes, then the potential was immediately dropped to 0.01 V vs RHE while the decay current was measured. After normalizing the current, we calculated effective time constants of 92.8 ms (asymmetric TiN) and 372 ms (mesoporous TiN), indicating that double-layer charging is ~ 4 x faster in the asymmetric structure, which we attribute to more facile ion diffusion. This result is consistent with the improved capacitance retention for asymmetric TiN at higher scan rate. We note that the open-circuit voltage varied by < 0.1 V between the asymmetric and mesoporous morphologies, consistent with the idea that the two structures had similar surface chemistries.

Since carbon represents the industry standard composition for double-layer capacitors due to its low density and process-ability, we also measured the rate-dependent capacitance of the asymmetric graphitic carbon. To increase the capacitance, the asymmetric carbon was first activated by cycling to 1.4 V vs RHE at 5 V s^{-1} to introduce redox functional groups, *e.g.*, oxygen on the carbon surface. Like asymmetric TiN, the CV retained most of the low scan rate shape at 5 V s^{-1} (Figure S4.9a). The CVs shown in Figure S4.9a were measured using the same protocol as for TiN after the activation step had reached a steady-state CV shape

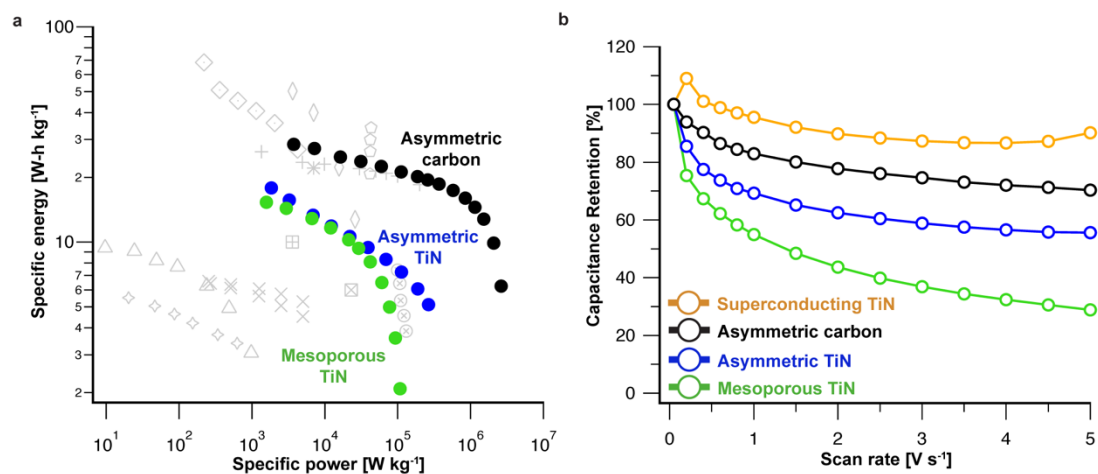


Figure 4.5. Capacitor performance benchmark and comparison of scan-rate dependent capacitance retention. (a) Ragone plot comparing energy storage performance of gyroidal mesoporous TiN, asymmetric TiN, and asymmetric carbon. Literature examples include $\text{LaMnO}_{3\pm\delta}$ (\diamond^{39}), MnO_2 (\boxplus^{40} , $*^{41}$, \triangle^{42} , \diamond^{43}), carbon nanotubes (\otimes^{44} , \boxtimes^{45}), graphene (\times^{46} , $+^{47}$), N-doped carbon (\diamond^3), and titanium carbide (\diamond^{48}). (b) Scan rate dependence of capacitance retention for superconducting asymmetric TiN, asymmetric carbon, asymmetric TiN, and gyroidal mesoporous TiN. All results were collected in Ar-saturated 0.1 M HClO_4 .

and capacitive current. We found the specific capacitance of asymmetric carbon to be $13.8 \mu\text{F cm}^{-2}_{\text{BET}}$ at 50 mV s^{-1} , with 70% capacity retention at 5 V s^{-1} . We hypothesize that the high capacitance retention is a result of the asymmetric structure and also the thinner cross section of the asymmetric carbon (Figure 4.5b).

To demonstrate the benefit of the asymmetric architecture, the energy density and power density of both asymmetric and gyroidal mesoporous TiN as well as asymmetric graphitic carbon were calculated and compared to literature reports (Figure 4.5a, S4.10). We report energy and power densities using a half-cell comparison, consistent with the cited literature. Since literature reports do not include resistance compensation, we report energy and power density values without resistance compensation. Full calculation details are included in the Methods section. Due to the facile ion diffusion through the

asymmetric structure, which leads to capacitance retention at high scan rates, the peak average power density for both asymmetric structures of TiN (112.9 kW kg⁻¹) and graphitic carbon (1151.5 kW kg⁻¹) are significantly higher than the state-of-the-art. The energy density at the peak power density for TiN is 7.3 W-h kg⁻¹ and for graphitic carbon is 14.5 W-h kg⁻¹. At the measured power density, these energy density values are amongst the highest energy values reported to date. We stress that these values represent a non-optimized result. We expect further improvements can be made by adding additional functional groups such as amines or by activating the carbon with CO₂ to further increase surface area.³⁰ Furthermore, the SNIPS process could be further optimized to improve capacitance retention, power density, and energy density.

Finally, we evaluated whether the observed rate limitation is a result of the imperfect electrical conductivity in TiN. To test the influence of electrical conductivity, we examined the rate capability of the asymmetric TiN with less residual oxygen, which has improved electrical conductivity. To this end, we used a second heat treatment step under flowing NH₃ to remove residual lattice oxygen. After initial annealing at 600 °C for 6 h, asymmetric TiN monoliths were subsequently annealed under flowing NH₃ at 865 °C for 3 h. After annealing, the structure retained its asymmetric morphology (Figure 4.6a-b), and open and accessible macroporous bottom (Figure 4.6e, f). The ordered top surface densified, however, likely a result of crystallite overgrowth (Figure 4.6c, d). Importantly, while the XRD peaks and relative intensities (Figure 4.6g) remained consistent with cubic

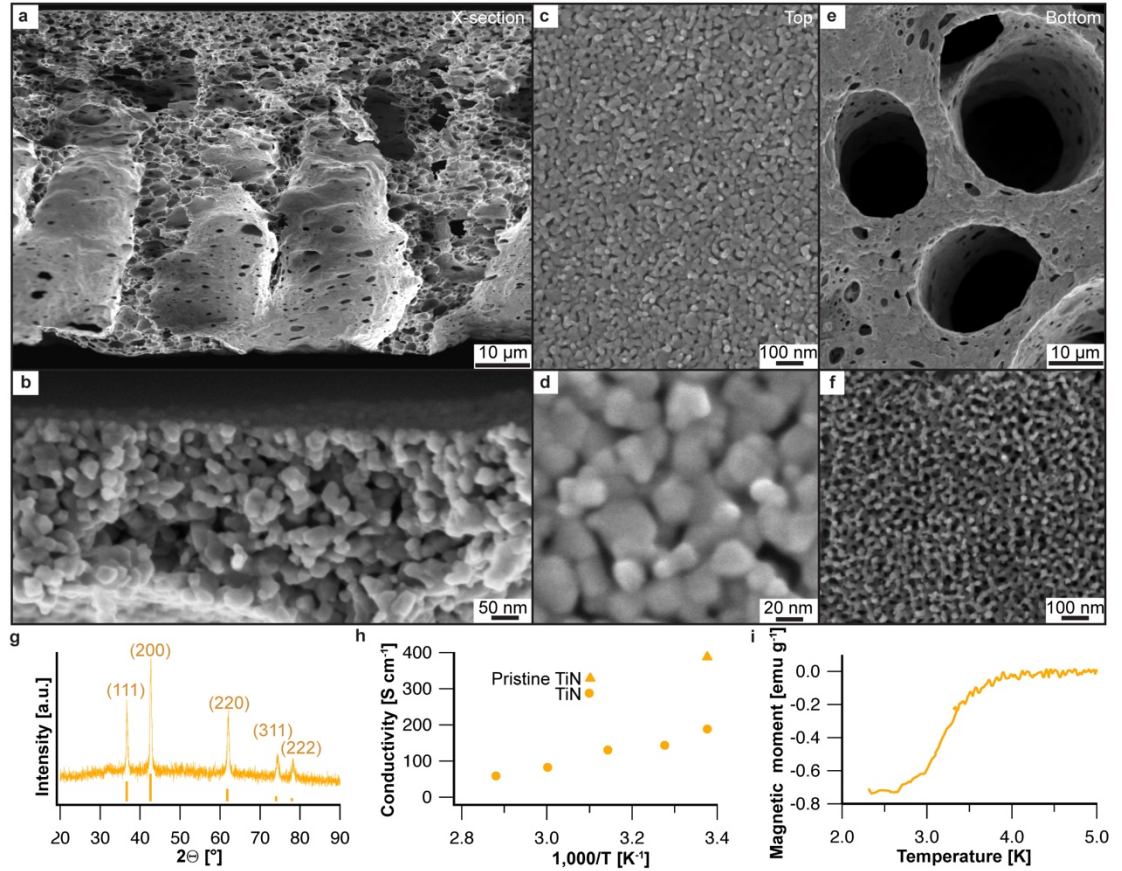


Figure 4.6. Characterization of asymmetric TiN superconductor. SEM characterization of: (a) $\sim 50 \mu\text{m}$ thick asymmetric cross-section; (b) the mesoporous top surface part of the cross-section; (c),(d) the mesoporous top surface; (e) bottom surface with macropores; (f) mesoporous wall. (g) XRD pattern: Blue tick marks indicate expected peak positions and relative intensities for cubic TiN (ICSD #00-038-1420). (h) Temperature dependent conductivity measurements. TiN is a nitride that was exposed to air for a longer period of time than the pristine TiN. (i) Temperature-dependent magnetization from 2.2 to 5 K for superconducting TiN membrane with an onset T_c of 3.8 K.

rocksalt TiN (ICSD #00-038-1420), the lattice parameter from XRD increased from 4.20 Å to 4.24 Å, similar to bulk TiN suggesting successful removal of additional residual oxygen.^{25,26} Furthermore, the grain sizes increased from 6.9 nm to 19 nm, consistent with the size of domains observed on the top surface in SEM (*e.g.* Figure 4.6d). The progression of the transformation through various processing steps is shown in Figure

S4.11.

The annealed membrane had a conductivity of 188 S cm^{-1} measured using a four-point probe geometry (Figure S4.12), comparable to that of glassy carbon (Figure 4.6h) as well as previous BCP-derived porous TiN thin films.^{18,31} While the electrical conductivity is sufficient for electrochemical applications, the value is lower than bulk TiN ($>10^4 \text{ S cm}^{-1}$) likely due to the remaining residual oxygen and vacancies resulting from the low ammonolysis temperature needed to maintain the porous structure in addition to the nanoscale grain sizes which increase electron scattering, lowering conductivity.^{27,32}

A superconducting TiN membrane could find application, *e.g.* in gas separations.^{33,34} The temperature-dependent magnetization of the high temperature annealed asymmetric TiN was measured under an applied field of 100 Oe during warming after zero-field cooling to 2.5 K (Figure 4.6i). A superconducting transition was observed between 2.5 K and about 4 K, with a flux expulsion from the material indicated by negative values of the magnetic moment. The observed T_c is slightly below the value reported in the literature for TiN (5.6 K), possibly due to residual oxygen and vacancies in the lattice.^{25,27,28,35–37}

To study the effect of residual oxygen content on the electrochemical properties of asymmetric TiN, the capacitance retention of the superconducting TiN was investigated using CV. Like the previous TiN monolith, a double-layer capacitance response dominated the CV result when scanned between 50 mV s^{-1} and 5 V s^{-1} . We note that the measured capacitive current was lower than the previous TiN monolith (Figure S4.8a, S4.8b), which likely reflects the loss of the residual oxygen content, which could be redox-active and thus can contribute to the capacitive current.³⁸ Significantly, the

capacitance retention at 5 V s^{-1} was 90% with respect to the slow scan rate capacitance, substantially higher than the 56% retention measured for the TiN treated only at $600 \text{ }^\circ\text{C}$ (Figure S4.8c). Based on this result, we conclude that our experiment does not yet test the limit of diffusion inside the asymmetric TiN structure. Instead, the limitation of our measurement is likely the electrical conductivity of the synthesized material. Our results demonstrate the exceptional diffusional performance of asymmetric morphologies and suggest that an asymmetric architecture can improve transport through, and pore utilization of, mesoporous materials, with particular interest for energy and sustainability applications.

Acknowledgements

This work was funded by the National Science Foundation under award DMR-1707836. K.E.F. and J.S. further thank the Center for Alkaline Based Energy Solutions (CABES) an Energy Frontier Research Center funded by the U.S. Department of Energy, Office of Science, Office of Basic Energy Sciences, under Award No. DE-SC0019445 (electrochemical characterization). This work made use of the Cornell Center for Materials Research Shared Facilities which are supported through the NSF MRSEC program (DMR-1719875) and the Cornell NanoScale Facility, a member of the National Nanotechnology Coordinated Infrastructure (NNCI), which is supported by the NSF (Grant ECCS-15420819). P.A.B. and R. P. T. were supported by the National Science Foundation Graduate Research Fellowship Program (DGE-1650441). This research used the Soft Matter Interfaces (SMI) beamline of the National Synchrotron Light Source II, a U.S. Department of Energy (DOE) Office of Science User Facility operated for the DOE

Office of Science by Brookhaven National Laboratory under Contract No. DE-SC0012704. The authors further thank Sol M. Gruner of the Cornell University Physics department for the opportunity of using laboratory space and equipment for conductivity measurements. The authors thank Wiesner group member J. Hinckley for input on figure design and Suntivich group member Ding-Yuan Kuo for valuable discussions and advice on electrochemical measurements.

Author Contributions

S.A.H., K.E.F., P.A.B., and U.B.W. conceived the project. S.A.H. performed and optimized synthesis, and collected and analyzed SEM, N₂ sorption, and XRD data. K.E.F. collected and analyzed electrochemical data, supervised by J.S. F.J.D. and P.A.B. assisted with some XRD data analysis and some synthetic optimization. P.A.B. collected and analyzed low-temperature magnetization data. P.A.B. collected the SAXS data. R.P.T. collected and analyzed conductivity. F.Y. performed sample etching. U.W. supervised the work and helped interpret data. S.A.H., K.E.F., J.S., and U.B.W. wrote the manuscript with input from all authors.

APPENDIX C

Material	Corresponding Figure	Trace Color	BET	Microp	Peak	FWHM [nm]	Single point
			surface area [m ² g ⁻¹]	ore area [m ² g ⁻¹]	pore size [nm]		adsorption pore volume [cm ³ g ⁻¹]
Asymmetric Carbon (Figure 3i)	4p,q	Black	1024 ± 142	655	20	12 ± 5.1	1.69
Asymmetric Carbon (Figure 3h)	S3n,o	Black	1322 ± 357	837	18	14 ± 6.4	1.96
Asymmetric TiO ₂	S2h,i	Red	60 ± 1.1	11	42	16 ± 6.8	0.57
Asymmetric TiN	4p,q	Blue	90 ± 3.0	15	41	17 ± 7.1	0.59
Mesoporous TiN	S4f,g	Green	139 ± 2.1	35	24	4.2 ± 1.8	1.29

Table S4.1. Surface area and pore volume of various asymmetric materials as measured via nitrogen sorption.

Material	Corresponding Figure	Trace Color	Anatase TiO ₂			TiN	
			LC a [Å]	LC c [Å]	XS [nm]	LC a [Å]	XS [nm]
Asymmetric 130 °C Hybrid	S1e	Purple	—	—	—	—	—
Asymmetric TiO ₂	S2g	Red	3.79	9.52	12	—	—
Asymmetric TiN (75 s evaporation time)	3o	Blue	—	—	—	4.20	6.9
Asymmetric TiN (60 s evaporation time)	S3m	Blue	*	*	*	4.21	6.5
Mesoporous TiN	S4e	Green	—	—	—	4.20	5.6
Asymmetric TiN Superconductor	6g, S5	Yellow	—	—	—	4.24	19
Asymmetric TiO ₂ (for superconductor)	S5	Red	3.80	9.54	12	—	—
Asymmetric 130 °C Hybrid (for superconductor)	S5	Purple	—	—	—	—	—

*residual TiO₂ (anatase)

Table S4.2. Lattice parameters and crystal size results of asymmetric materials as determined *via* XRD.

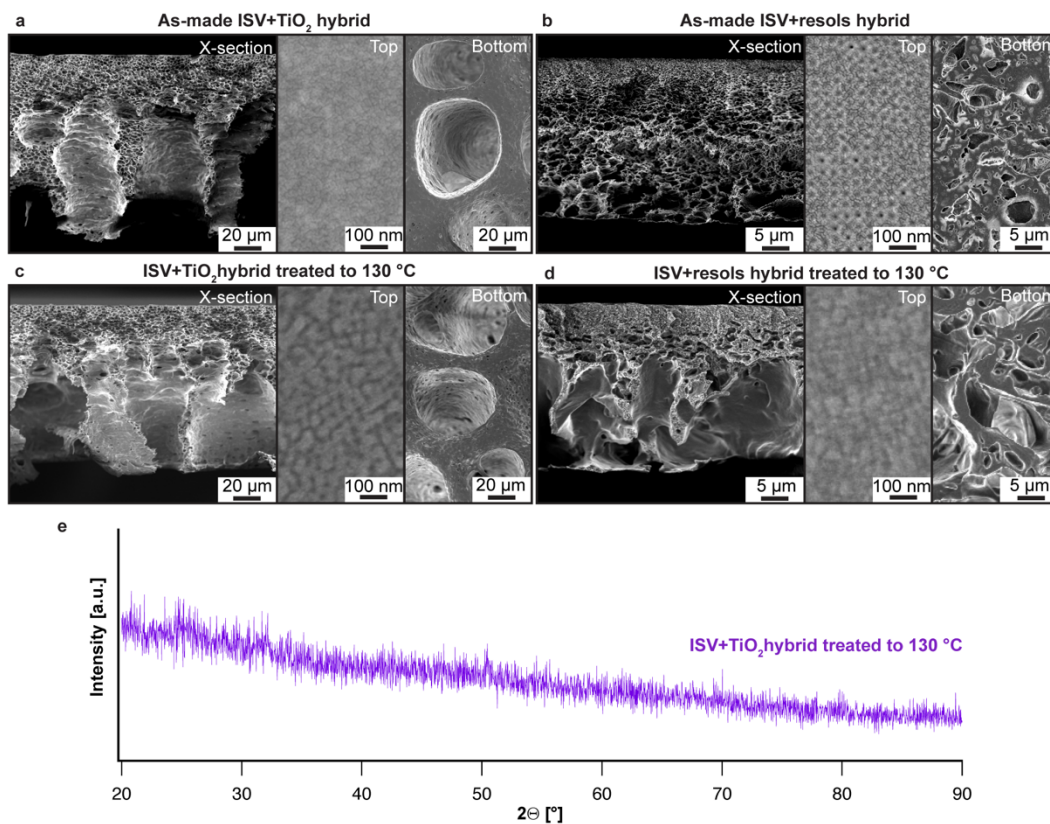


Figure S4.1. Characterization *via* SEM of the cross-section, top surface, and bottom surface of the (a) As-made ISV+TiO₂ hybrid, (b) As-made ISV+resols hybrid, (c) ISV+TiO₂ hybrid treated to 130 °C, (d) ISV+resols hybrid treated to 130 °C, and (e) XRD of the 130 °C ISV+TiO₂ hybrid.

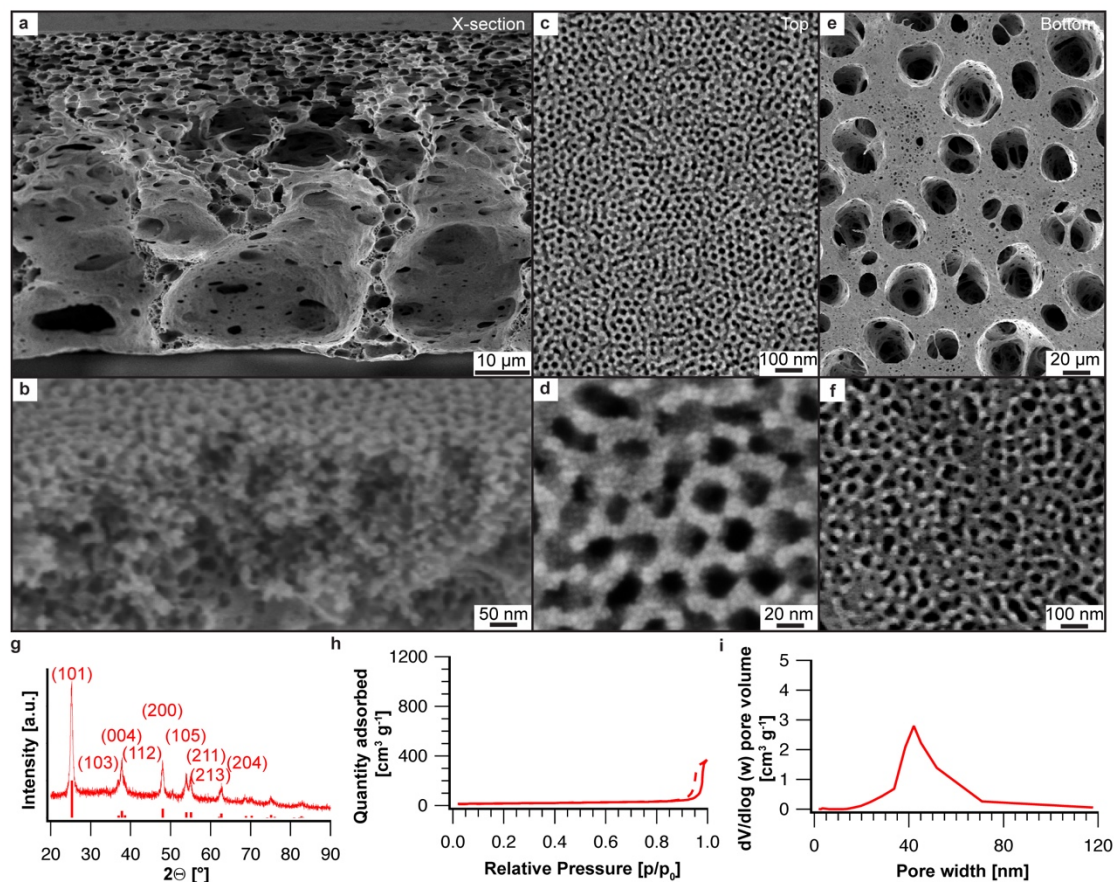


Figure S4.2. Characterization of asymmetric TiO_2 following heat-treatment to $400\text{ }^\circ\text{C}$ in air. (a) $\sim 60\text{ }\mu\text{m}$ cross-section SEM showing asymmetry. (b) Higher magnification SEM of the top mesoporous part of the cross-section. (c) SEM of the mesoporous top surface. (d) Higher magnification top surface SEM. (e) SEM of macroporous bottom surface. (f) Higher magnification SEM of the mesoporous wall. (g) XRD pattern of asymmetric TiO_2 . Red tick marks correspond to anatase TiO_2 (I41/amd, space group #141, ICSD # 01-070-7348). (h) Nitrogen sorption isotherm. (i) BJH derived pore size distribution of asymmetric TiO_2 .

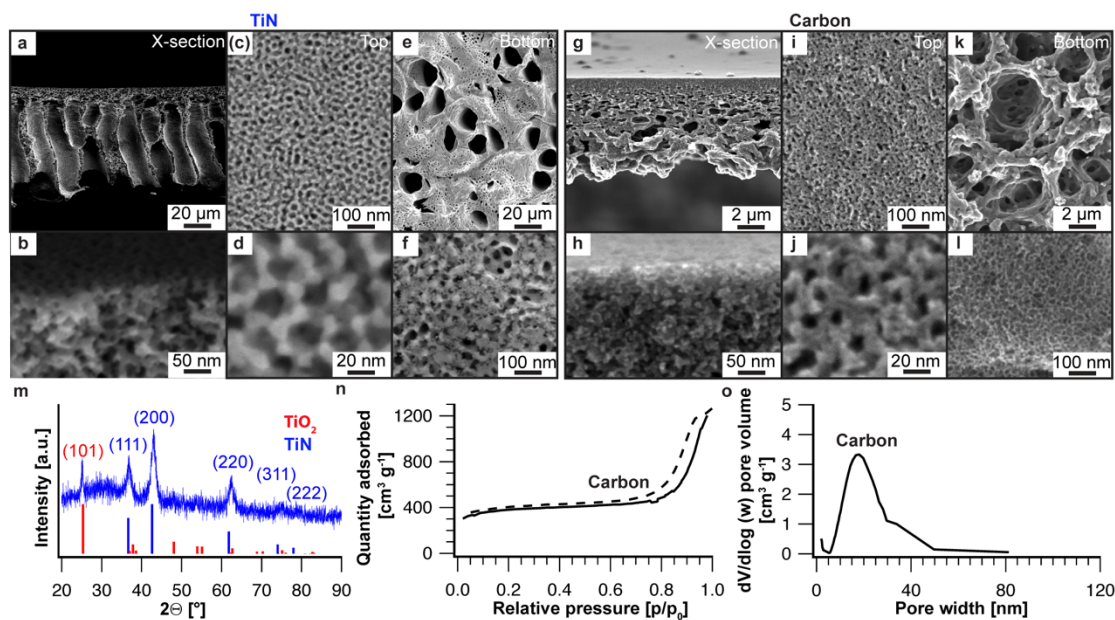


Figure S4.3. Full characterization of the asymmetric TiN and carbon materials for which the cross-sections are shown in panels (4.3a) and (4.3h) in Figure 4.3 in the main text. (a-f) SEM characterization of the asymmetric TiN from Figure 4.3a; (a) $\sim 60 \mu\text{m}$ asymmetric cross-section; (b) High magnification SEM of the top mesoporous part of the cross-section; (c) Mesoporous top surface. (d) Higher magnification top surface SEM; (e) Macroporous bottom surface; (f) Higher magnification SEM of the mesoporous wall. (g-l) SEM characterization of asymmetric carbon from Figure 4.3h: (g) $\sim 8 \mu\text{m}$ asymmetric cross-section SEM; (h) Higher magnification SEM of the top $\sim 150 \text{ nm}$ mesoporous top part of the cross-section; (i) Mesoporous top surface; (j) Higher magnification top surface SEM; (k) Macroporous bottom surface; (l) Higher magnification SEM of the mesoporous wall. (m) XRD pattern of asymmetric TiN. Blue tick marks indicate expected peak positions and relative intensities for cubic TiN (Fm-3m, space group # 230, ICSD #00-038-1420), while red tick marks indicate tetragonal anatase anatase TiO_2 (I41/amd, space group #141, ICSD # 01-070-7348). (n) Nitrogen sorption isotherm of the asymmetric carbon. (o) BJH derived pore size distribution of the asymmetric carbon.

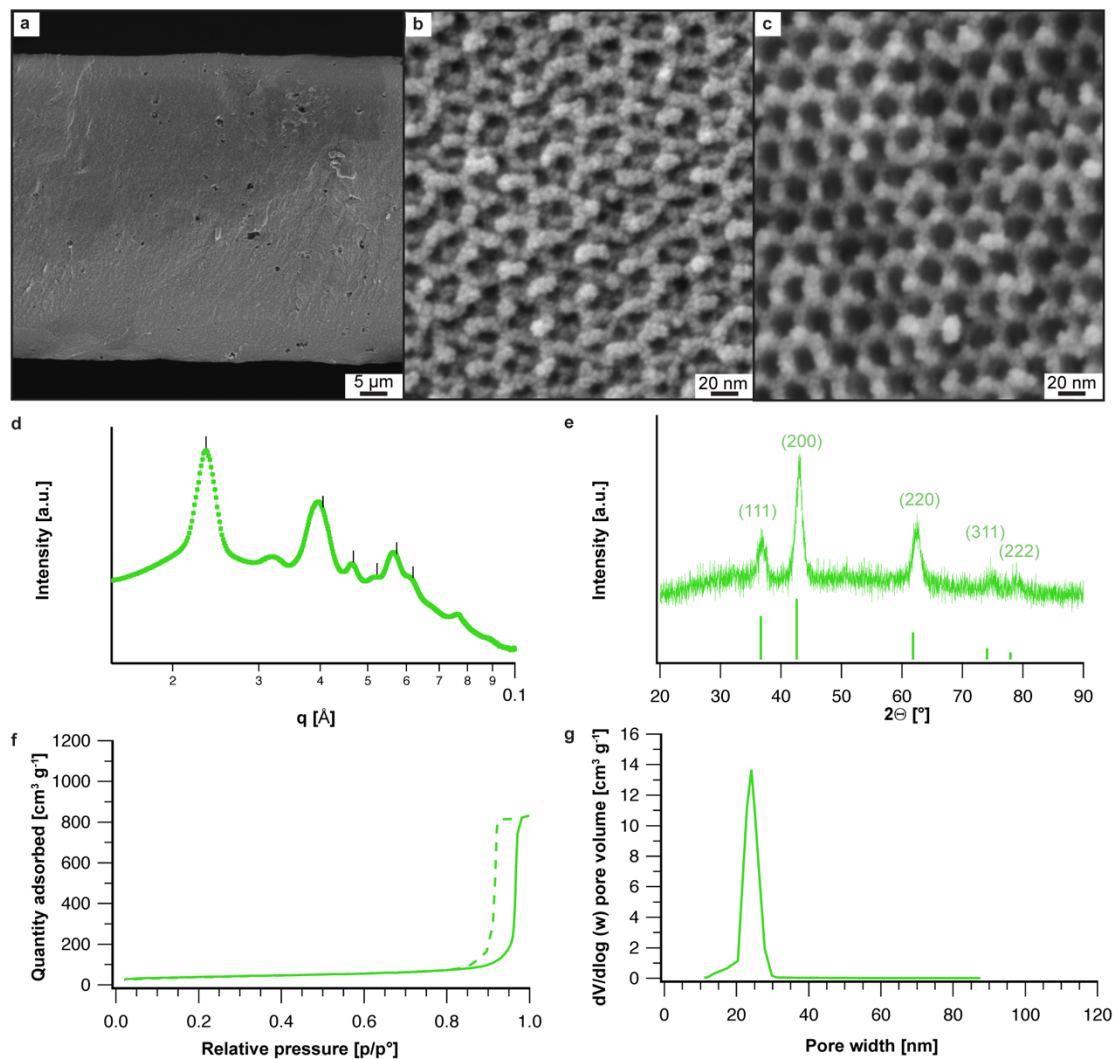


Figure S4.4. Characterization of BCP SA directed alternating gyroidal mesoporous TiN treated to 600 °C in ammonia. (a) Low magnification SEM of the cross-section. (b) Higher magnification SEM of the top surface. (c) High magnification SEM of the cross-section. (d) Small-angle x-ray scattering with tick marks indicating the expected peak positions for the q^{214} space group of the alternating gyroid structure. (e) XRD pattern with blue tick marks indicating expected peak positions and relative intensities for cubic TiN (ICSD #00-038-1420). (f) Nitrogen sorption isotherms. (g) BJH derived pore size distribution.

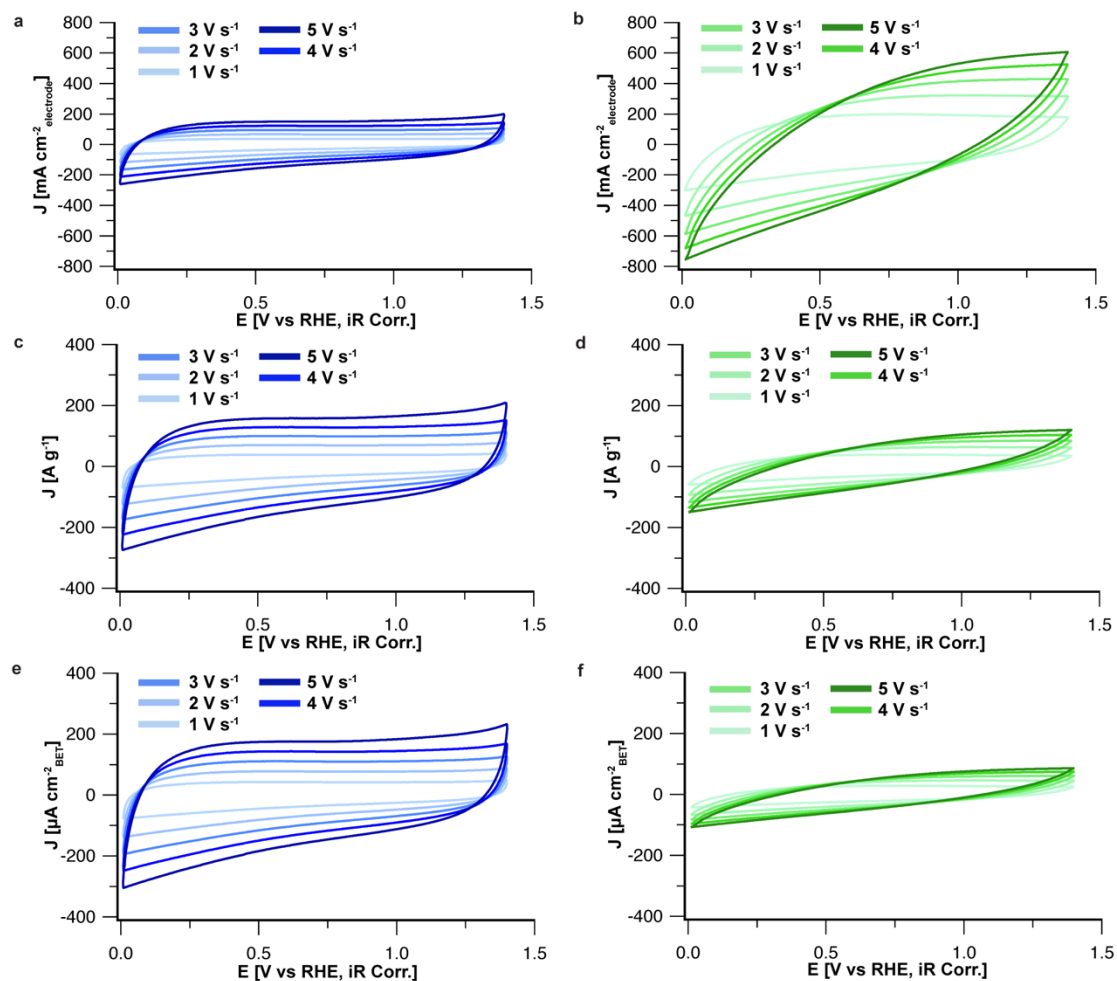


Figure S4.5. Asymmetric TiN (a,c,e) and alternating gyroidal mesoporous TiN (b,d,f) cyclic voltammograms normalized by (a,b) electrode area, (c,d) electrode mass, and (e,f) surface area. All results were collected in Ar-saturated 0.1 M HClO₄ electrolyte. Scan rates shown: 1 V s⁻¹, 2 V s⁻¹, 3 V s⁻¹, 4 V s⁻¹, and 5 V s⁻¹.

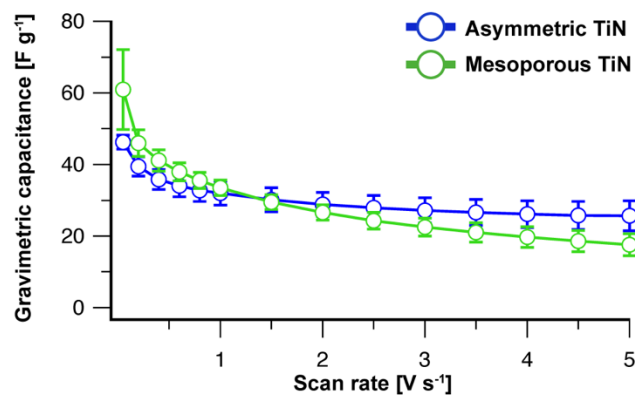


Figure S4.6. Scan rate dependence of gravimetric capacitance for asymmetric TiN (blue) and alternating gyroidal mesoporous TiN (green). Error bars represent the standard deviation of three independent measurements. All results were collected in Ar-saturated 0.1 M HClO₄ electrolyte.

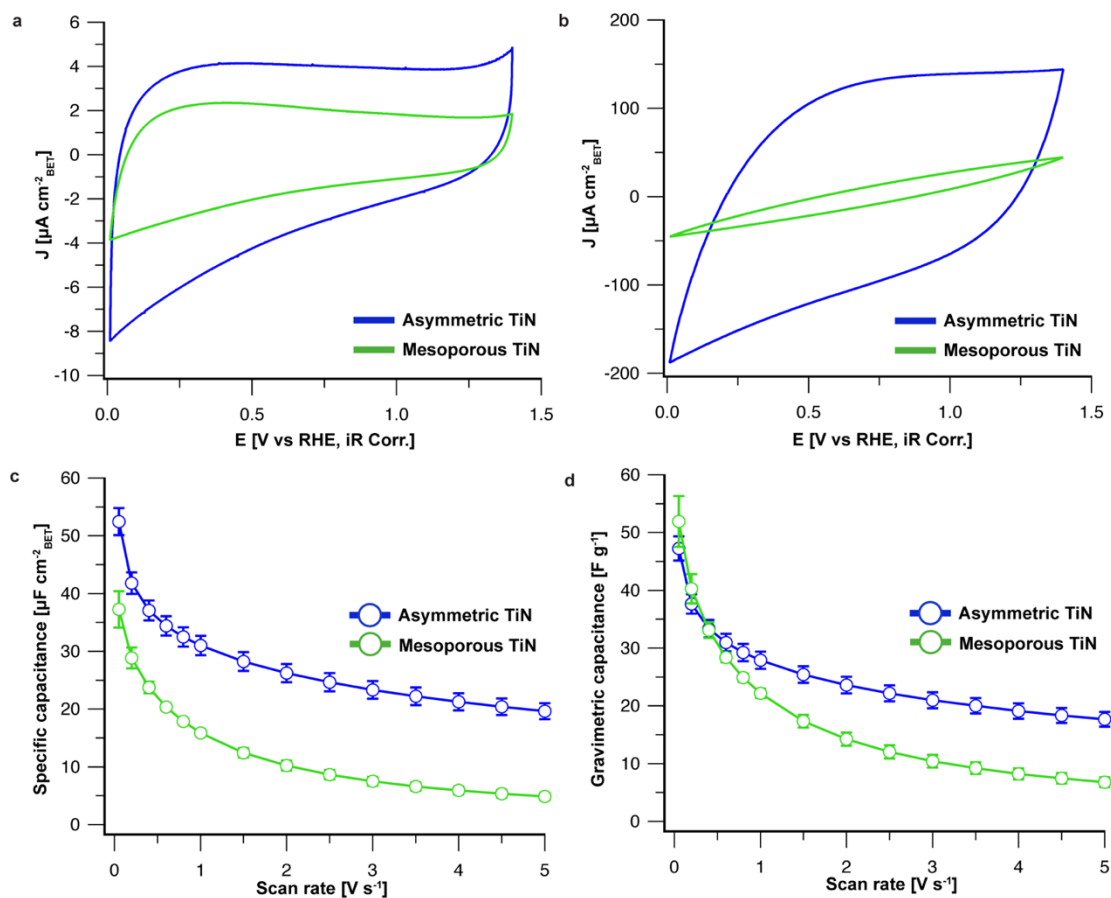


Figure S4.7. Electrochemical characterization of asymmetric TiN and alternating gyroidal mesoporous TiN without iR compensation. Cyclic voltammograms for asymmetric TiN (blue) and gyroidal mesoporous TiN (green) at (a) 50 mV s⁻¹ and (b) 5 V s⁻¹. (c) Scan rate dependence of specific capacitance for asymmetric TiN (blue) and gyroidal mesoporous TiN (green) showing improved surface accessibility for asymmetric TiN. (d) Scan rate dependence of gravimetric capacitance for asymmetric TiN (blue) and gyroidal mesoporous TiN (green). Error bars represent the standard deviation of three independent measurements. All results were collected in Ar-saturated 0.1 M HClO₄ electrolyte.

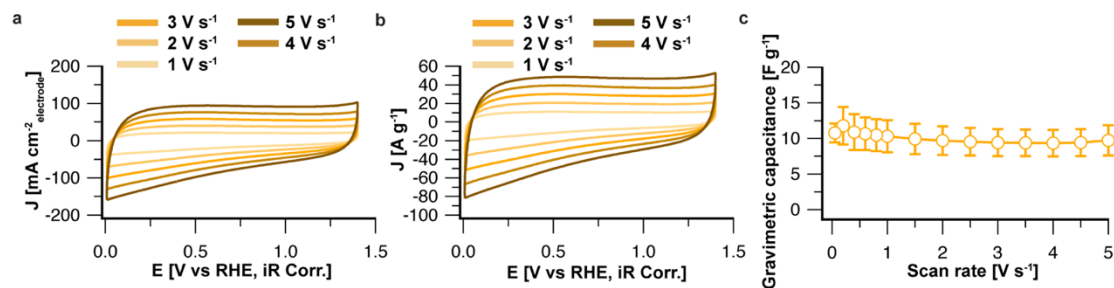


Figure S4.8. Superconducting TiN cyclic voltammograms normalized by (a) electrode area, and (b) electrode mass. (c) Scan rate dependence of gravimetric capacitance for superconducting TiN. Error bars represent the standard deviation of three independent measurements. All results were collected in Ar-saturated 0.1 M HClO_4 electrolyte.

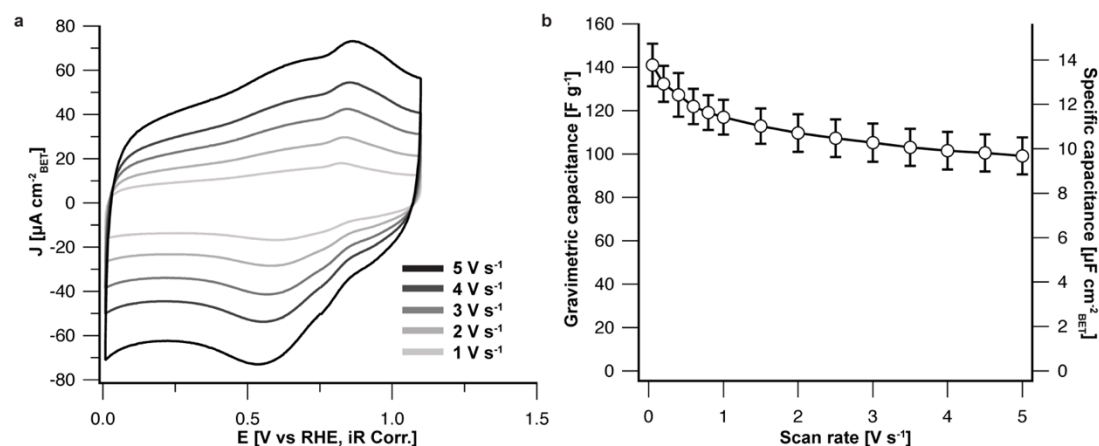


Figure S4.9. (a) Cyclic voltammograms for asymmetric carbon at 1 V s^{-1} , 2 V s^{-1} , 3 V s^{-1} , 4 V s^{-1} , and 5 V s^{-1} . (b) Scan rate dependent gravimetric and specific capacitance for asymmetric carbon. Error bars represent the standard deviation of three independent measurements. All results were collected in Ar-saturated 0.1 M HClO_4 electrolyte.

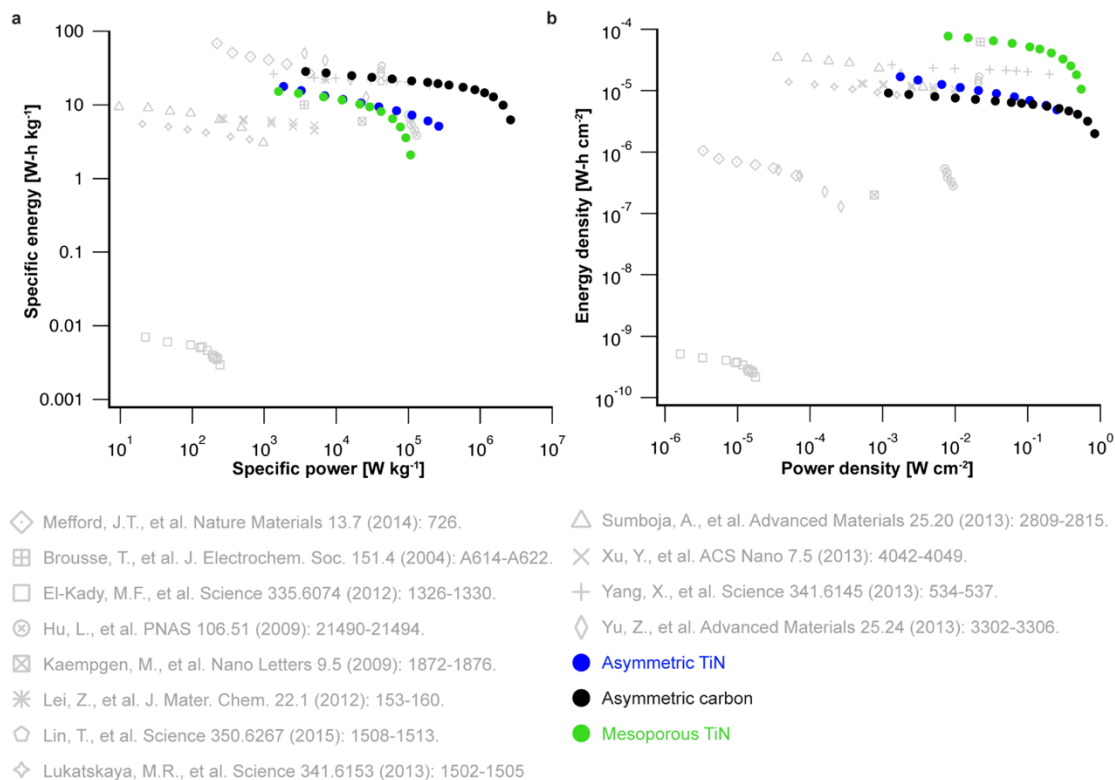


Figure S4.10. Ragonne Plot normalized by (a) mass and (b) electrode area comparing alternating gyroidal mesoporous TiN (green), asymmetric TiN (blue), and asymmetric carbon (black) with select literature results.

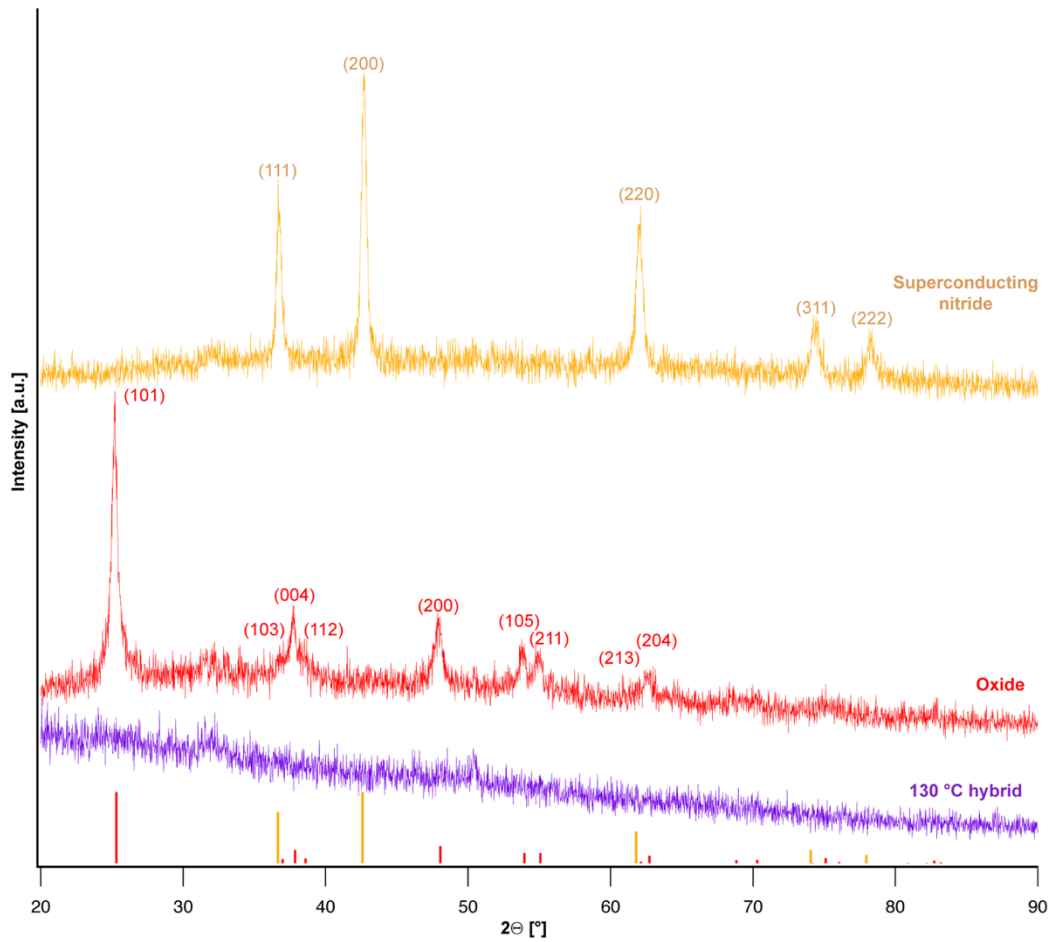


Figure S4.11. XRD patterns at various steps in the processing on the way to asymmetric TiN with superconducting properties. From bottom to top: (purple) amorphous ISV/oxide hybrid heat-treated to 130 °C. (red) Freestanding asymmetric oxide heat-treated to 400 °C in air. Red tick marks indicate the expected peak positions and relative intensities for tetragonal anatase (TiO₂) (ICSD 01-070-7348). (yellow) Freestanding asymmetric superconducting TiN heat-treated to 865 °C in ammonia. Blue tick marks indicate expected peak positions and relative intensities for cubic TiN (ICSD 00-038-1420).

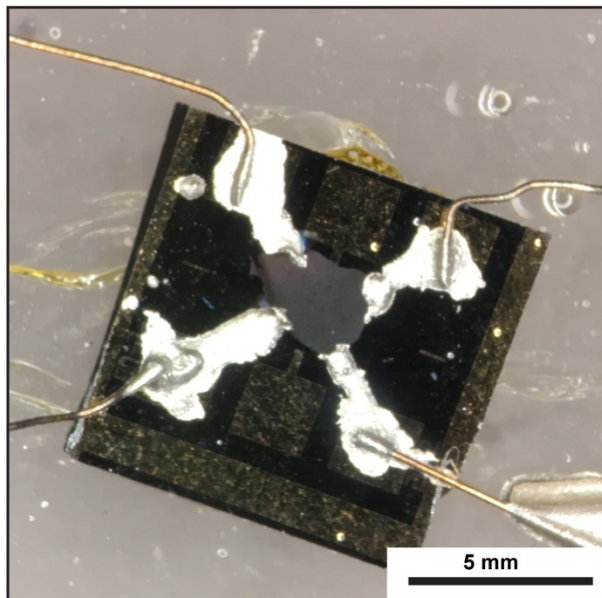


Figure S4.12. Photograph of bonded asymmetric TiN prior to conductivity measurement

Experimental Section

Materials Synthesis/Preparation

Materials.

Materials were used as received unless otherwise stated. Anhydrous (99.9 %) grades of tetrahydrofuran (THF) and 1,4-dioxane (DOX) were obtained from Sigma-Aldrich. The following chemicals were used for the sol-gel synthesis: Tetrahydrofuran (THF) (Sigma-Aldrich, anhydrous, $\geq 99.9\%$, inhibitor-free), titanium tetraisopropoxide (TTIP) (Sigma Aldrich, 99.999% trace metals basis or Alfa Aesar, 99.995% metals basis), and hydrochloric acid (HCl) (BDH, ACS Grade, 36.5-38%) obtained from VWR.

The materials used in the synthesis of the phenol formaldehyde resols additive were as follows: Phenol (Sigma-Aldrich, purified by redistillation, $\geq 99\%$), formalin solution (Sigma-Aldrich, ACS reagent, 37 wt% in water, 10-15% methanol as stabilizer), sodium hydroxide (Sigma-Aldrich, reagent grade, $\geq 98\%$ pellets anhydrous), para-toluene sulfonic acid monohydrate (Sigma-Aldrich, ACS reagent, $\geq 98.5\%$), and deionized (DI) water with a resistivity of 18.2 M Ω cm which was also used as the nonsolvent precipitation bath.

The following gases were used for thermal processing: Argon (high purity) and nitrogen obtained from Airgas; Either electronic grade ammonia (99.999% obtained from Praxair) or anhydrous ammonia (99.9%; premium grade) that was purified over an SAES MicroTorr MC400-702F to remove residual oxygen and moisture.

The following chemicals were used in the electrochemical measurements: Perchloric acid (GFS Chemicals, Veritas double-distilled) was used as received; Pelco

Colloidal Gold Paste was obtained from Ted Pella while Omegabond 101 epoxy was obtained from Omega Engineering; Argon (ultra-high purity) was obtained from Airgas; Deionized (DI) water with a resistivity of 18.2 M Ω cm was used for all electrochemical measurements.

Materials used in the resistivity measurement were silver wire (99.95%, 0.2mm) obtained from VWR and Epo-TEK H20E silver-filled epoxy obtained from Electron Microscopy Services.

Polymer Synthesis and Characterization.

ISV for preparation of asymmetric oxides, nitrides, and carbons

The poly(isoprene)-*b*-poly(styrene)-*b*-poly(4-vinylpyridine) (PI-*b*-PS-*b*-P4VP, or simply ISV) triblock terpolymers used to prepare the asymmetric materials in this study were synthesized *via* a previously reported sequential living anionic polymerization route.²¹ The ISV used for the asymmetric TiN syntheses had a molar mass of 113 kg mol⁻¹ with 29 vol% PI, 59 vol% PS, 12 vol% P4VP, and a polydispersity index of 1.3. The ISV used for the asymmetric carbon syntheses had a molar mass of 95 kg mol⁻¹ with 29 vol% PI, 57 vol% PS, 14 vol% P4VP and a polydispersity index of 1.2.

A Varian INOVA 400 MHz ¹H solution nuclear magnetic resonance (¹H NMR) spectrometer was used to determine the block fractions of each block using chloroform-d₆ as the solvent (D, 99.8%, Cambridge Isotope Laboratories). A Waters ambient-temperature gel permeation chromatograph (GPC) equipped with a Waters 410 differential refractive index (RI) detector (flow rate: 1 mL min⁻¹) was used to analyze the

ISV polydispersity using polystyrene standards for polydispersity (PDI) determination. Tetrahydrofuran (THF) was used as the solvent. Overall ISV molar mass was obtained using the molar mass of the PI block obtained from an aliquot removed from the reaction vessel after PI synthesis (determined with GPC using PI standards) combined with the NMR results of the molar ratios of the different blocks.

ISO for alternating gyroidal mesoporous oxides and nitrides

The poly(isoprene)-*b*-poly(styrene)-*b*-poly(ethylene oxide) (PI-*b*-PS-*b*-PEO, or simply ISO) triblock terpolymer used to make the BCP SA derived mesoporous materials with alternating gyroid morphology was synthesized using a sequential living anionic polymerization method reported elsewhere.^{18,27,49–52} The polymer had a molar mass of 83 kg mol⁻¹ with 29 vol% PI, 64 vol% PS, 6.5 vol% PEO, and a polydispersity index of 1.09. A Varian ¹H solution nuclear magnetic resonance (¹H NMR) spectrometer was used to determine the block fractions of each block using chloroform-d6 as the solvent (D, 99.8%, Cambridge Isotope Laboratories). A Waters ambient-temperature gel permeation chromatograph (GPC) equipped with a Waters 410 differential refractive index (RI) detector (flow rate: 1 mL min⁻¹) was used to analyze the ISO polydispersity using polystyrene standards for polydispersity (PDI) determination. Tetrahydrofuran (THF) was used as the solvent. Overall ISO molar mass was obtained using the molar mass of the PI block obtained from an aliquot removed from the reaction vessel after PI synthesis (determined with GPC using PI standards) combined with the NMR results of the molar ratios of the different blocks.

Polymer Dope Solution Preparation.

Asymmetric oxides and nitrides

The ISV solutions used to prepare the asymmetric TiN were prepared by dissolving ISV at 15 wt% in a solvent mixture of DOX:THF (7:3 by weight) and stirred to obtain homogeneous solutions. Typically, 0.1 g of ISV was used to prepare the initial solution. The TiO₂ sol was prepared separately *via* a hydrolytic sol-gel route, similar to that reported previously.^{18,27,49,50} The TiO₂+ISV vol% was 7.9 vol%.

Asymmetric carbons

The ISV solutions used to prepare asymmetric carbons were made by dissolving ISV in 7:3 DOX:THF (by weight), allowing for the solution to be fully homogeneous before adding the resols in a 2:1 ISV:resols (by weight) ratio. We call this method the consecutive method which was used for the preparation of materials with cross-sections as shown in Figure 3i. Alternatively, in what we call the simultaneous method, the undissolved ISV could also be mixed together with resols (which were predissolved in 7:3 DOX:THF) in a 2:1 ISV:resols ratio (by weight), immediately followed by immediately adding solvent consisting of 7:3 DOX:THF (by weight). For both methods stock solutions of 25 wt% resols in DOX:THF (7:3 by weight) were made. The final casting solution was 10 wt% ISV+resols (2:1 ISV:resols weight ratio) in 7:3 DOX:THF.

Alternating gyroidal mesoporous oxides and nitrides

The solutions used to make the alternating gyroidal mesoporous materials were prepared using a similar method to a previously reported process.^{18,27,49} 150 mg of ISO

were dissolved in 6 mL of THF. Thereafter, 497 μL of the sol solution, prepared as described above, was added to the ISO/THF solution such that the PEO plus TiO_2 together formed a 17 vol% solution (corresponding to 11.22 vol% TiO_2 relative to ISO).

Dope Solution Casting.

Asymmetric oxides and nitrides

Self-assembly/co-assembly and non-solvent induced phase separation (S/CNIPS) was used to prepare the asymmetric materials. The casting solution was pipetted onto a glass substrate, a thick film was cast with a doctor blade using a fixed gate height (height between the substrate and casting blade) adjusted using feeler blades of 305 and 381 μm . After 75 s evaporation time, to allow for the formation of a concentration gradient along the film-normal, the films were plunged into a non-solvent DI water bath to allow for precipitation, thereby producing the porous membranes with structural gradient.

Alternating gyroidal mesoporous oxides and nitrides

In order to make the gyroidal mesoporous materials, the solutions were cast in Teflon dishes of $\sim 1\text{cm}$ diameter, which were set on a glass dish and covered by a glass dome, and the solvent was allowed to slowly evaporate at room temperature enabling solvent evaporation induced self-assembly, until the films were fully dry.

Asymmetric carbon

Co-assembly and nonsolvent induced phase separation (CNIPS) was used to prepare the ISV+resols hybrid membranes. Films were cast onto substrates that were heated to 30 $^{\circ}\text{C}$ in an environment with relative humidity $<28\%$. A pipette was used to

dispense the casting solutions onto the glass substrates. Thereafter a doctor blade whose gate height was adjusted to between 203 and 229 μm was used to control the film thickness. After ~ 40 s evaporation time, the films were plunged into a non-solvent DI water bath to precipitate the polymer.

Thermal Processing.

All oxides and nitrides

The membranes/films were dried and then heated in a convection oven to 50 $^{\circ}\text{C}$ for 2 h, followed by 5 h at 130 $^{\circ}\text{C}$. In the case of the gyroidal mesoporous materials, the polymer/oxide hybrid films were etched to remove a dense overlayer formed in that case. The etching procedure consisted of a tetrafluoromethane plasma in an Oxford Plasmalab 80+ Reactive Ion Etcher system at 300W for 45 min on each side of the film. The asymmetric materials did not require etching. These steps were followed by a heat-treatment step in a flow furnace, which was open to air, in order to produce the freestanding oxides. The temperature profile for this step was 1 $^{\circ}\text{C min}^{-1}$ to 400 $^{\circ}\text{C}$. The temperature was held at 400 $^{\circ}\text{C}$ for 3 h before being allowed to cool back to room temperature. In order to produce titanium nitrides, the oxides were heated in a flow furnace under flowing ammonia gas (10 L h^{-1}) with a ramp rate of 5 $^{\circ}\text{C min}^{-1}$. The temperature was held at 600 $^{\circ}\text{C}$ for 6 h before being allowed to cool to room temperature. Before removing the samples from the furnace, the tube was purged with argon or nitrogen in order to remove any remaining ammonia gas.

To obtain superconducting titanium nitrides, a second heat-treatment in ammonia

at 5 °C min⁻¹ to 865 °C with a dwell time of 3 h at 865 °C and an ammonia flow rate of 10 L h⁻¹ was used. After the dwell time, the tube was cooled to room temperature under flowing ammonia and purged with argon or nitrogen before the samples were removed.

Carbons

After casting, the membranes were dried and heated for ~24 h in a convection oven to crosslink the resols at 130 °C. Thereafter, the membranes were subjected to an additional heat-treatment step under flowing nitrogen with the following temperature profile: 1 °C min⁻¹ to 600 °C with a dwell time of 3 h followed by further heating at a ramp rate of 5 °C min⁻¹ to 900 °C with a dwell time of 3 h. Thereafter, the materials were allowed to cool to room temperature at ambient rate.

Materials Characterization

SEM Analysis.

Scanning electron microscopy (SEM) micrographs were obtained using a ZEISS Gemini 500 scanning electron microscope (SEM) and voltage of 2 kV. Samples were either uncoated or coated with gold-palladium prior to imaging. SEM images were brightness/contrast adjusted.

X-ray Diffraction Characterization.

XRD data for the hybrids, oxides, and nitrides were collected on a Bruker D8 Advance ECO powder diffractometer equipped with a high-speed silicon strip detector,

using CuK α radiation ($\lambda = 1.54 \text{ \AA}$) and a step size of 0.019° (2θ) at 0.2 s step^{-1} , i.e. $5.7^\circ \text{ min}^{-1}$. MDI Jade was used for the analysis by fitting the peak profiles.

Lattice parameters for titanium nitride were calculated using the raw XRD data for the (200) reflection. The coherent scattering domain sizes were calculated using Debye-Scherrer analysis with shape factor $k=1$ and were the result of an average of the values for the first five peaks. Instrumental and other sources of peak broadening were not accounted for in this analysis, which represents the lower limit of the domain size. Peak markings correspond to the expected peak positions and relative intensities of cubic Fm-3m (space group #225) TiN (osbornite) (ICSD #00-038-1420) with a lattice parameter of 4.24 \AA .

Lattice parameters for titanium dioxide were calculated using the raw XRD data for the (200) and (105) reflections. The coherent scattering domain sizes were calculated using Debye-Scherrer analysis with a shape factor $k=1$ and were the result of the values obtained using the (101), (200), (105), and (211) reflections. Instrumental and other sources of peak broadening were not accounted for in this analysis, which represents the lower limit of the domain size. Peak markings correspond to the expected peak positions and relative intensities of a tetragonal crystal system of I41/amd (space group #141) for TiO₂ (anatase) (ICSD entry #01-070-7348) with lattice parameters of $a = b = 3.78 \text{ \AA}$ and $c = 9.50 \text{ \AA}$.

Nitrogen Sorption.

Nitrogen adsorption-desorption isotherms of the oxides, nitrides, and carbons were recorded using a Micromeritics ® ASAP 2020 surface area and porosity analyzer at -

196 °C. The specific surface areas were determined following the Brunauer-Emmett-Teller (BET) method.^{53,54} Barrett-Joyner-Halenda (BJH) analysis was used to determine the pore size distributions.⁵⁵ The reported errors result from the standard deviation from weighing each material several times. The standard deviation of the full-width at half-max (FWHM) is a result of fitting the pore size distribution with a least-squares fit using a gaussian function in Igor Pro.

Small-Angle X-Ray Scattering.

SAXS data in Figure S4d was collected at the Soft Matter Interfaces beamline at NSLS-II in in-vacuum mode using a Dectris Pilatus 1M detector operated at a sample-to-detector distance of 8.287 m and an incident photon energy of 11.50 keV.⁵⁶ The resulting images were radially integrated and plotted using the Nika and Irena packages for Igor Pro.^{57,58}

Electrochemical Measurements.

Electrodes were fabricated by adhering titanium wire to the nitride and carbon monoliths using a two-step procedure. First, the wires were affixed to the monoliths with conductive gold paint and allowed to cure for 2 h. After curing, an inert two-part epoxy was mixed and used to cover the back and sides of the monolith as well as the gold paint and approximately 1 inch of the wire to ensure that only the monolith generated an electrochemical response. The inert epoxy was allowed to cure for 12 h.

All electrochemical measurements were conducted using a three-electrode electrochemical cell with 0.1 M perchloric acid as the supporting electrolyte and a

platinum wire as the counter electrode. The applied potential was controlled using a Bio-Logic SP-300 potentiostat while an Ag/AgCl electrode was used as the reference electrode. The reference electrode was placed in a capillary filled with 0.1 M perchloric acid to further isolate it from the electrolyte and prevent chlorine evolution at high applied potentials. The reference electrode was calibrated against the reversible hydrogen electrode (RHE) scale by measuring the hydrogen evolution/oxidation currents on a polycrystalline Pt disk (Pine) in 0.1 M HClO₄ electrolyte. All potentials in this study were referenced to the RHE potential scale.

Capacitance measurements of all monoliths were obtained using cyclic voltammetry in an electrolyte saturated with argon (Airgas, ultra-high purity) prior to measurement. All cyclic voltammograms were measured both with iR-corrected potentials and without iR correction. The total resistance, R, was measured as the AC impedance at high frequency in the three-electrode system and corresponded to the sum of all electrolyte and contact resistances. This resistance value was subsequently used to manually compensate the applied potential using the Bio-Logic SP-300 hardware compensation mode during the measurements. The iR-corrected cyclic voltammograms were used to compare the intrinsic capacitance retention of each asymmetric and mesoporous morphology. Since literature results typically report performance without iR compensation, however, the uncompensated results were used to calculate all power and energy densities.

To introduce oxygen functional groups to the asymmetric graphitic carbon surface, each monolith was activated by cycling between 0.01 V vs RHE and 1.4 V vs RHE at 5 V s⁻¹ until the cyclic voltammogram reached an equilibrium where it did not

change with subsequent cycling. All TiN monoliths were measured between 0.01 V and 1.4 V vs RHE without a prior activation step. For all samples, data for the fastest scan rate were collected first, followed by incrementally slower rates.

Chronoamperometry measurements were conducted in the same Ar-saturated electrolyte. The effective time constants were calculated by fitting the chronoamperometry data over the exponential decay regime using:

$$\frac{I}{I_0} = e^{-t/RC} \quad (1)$$

The cutoff point for the data was defined as the point at which $R^2 = 0.99$ for the exponential fit.

Power and Energy Density Calculations.

To facilitate a comparison to literature results, cyclic voltammograms without iR compensation were used to calculate all power and energy densities reported herein. The average power delivered by each electrode at a given scan rate was calculated by integrating the area of each capacitive box. The energy density was calculated by first measuring the total capacitance, C, using:

$$C = \frac{\int_{V_1}^{V_2} I(V)dV}{2(V_2-V_1)\frac{dV}{dt}} \quad (2)$$

Subsequently, the total energy stored was calculated by multiplying the capacitance with the voltage range using:

$$Energy = \frac{1}{2}CV^2 \quad (3)$$

All power and energy values were normalized by either the electrode mass or the electrode area. The electrode area was extracted using image processing software. For

gyroidal mesoporous TiN, the total mass of each electrode was derived from the pore volume measured with nitrogen sorption and the electrode thickness measured using SEM. Specifically:

$$Electrode\ mass = \frac{(thickness)(electrode\ area)}{pore\ volume} \quad (4)$$

The pore volume only accounts for meso- and microporosity, however, so for the asymmetric morphologies, monoliths were weighed using a TA Instruments Q500 thermogravimetric analyzer (TGA) and normalized by the electrode area to obtain an areal density for each asymmetric morphology. This areal density was subsequently multiplied by the area of each electrode to obtain the electrode mass.

Conductivity Measurements.

Conductivity measurements were performed using samples prepared in a multistep procedure. Monoliths were mounted onto a carrier chip and electrically contacted using Epo-TEK H20E silver-filled epoxy. The carrier chip was fabricated by sputter depositing multiple gold contact pads onto a 100-nm thermal oxide layer on a (110) silicon substrate. These gold pads were in turn contacted using silver wire and Epo-TEK H20E, and a Keithley 2400 sourcemeter used for a four-point Van der Pauw conductivity measurement. The horizontal resistance was measured via the average voltage drop along the two horizontal edges using both polarities of the current source and voltage meter. An analogous method was used to calculate the vertical resistance. All measurements were performed with an excitation current of 100 μ A. The sheet resistance was calculated numerically from the horizontal and vertical resistance using the relation:

$$e^{-\pi R_{vertical}/R_{sheet}} + e^{-\pi R_{horizontal}/R_{sheet}} = 1 \quad (5)$$

Resistivity was determined by multiplying the sheet resistance by the thickness and the porosity fraction, while conductivity was calculated from the inverse of resistivity. The asymmetric TiN had a conductivity of 188 S cm^{-1} . These conductivity values are lower than bulk TiN ($>10^4 \text{ S cm}^{-1}$) likely due to residual oxygen resulting from the low ammonolysis temperature needed to maintain the porous structure but remain significantly higher than typical catalysis and catalyst support materials.^{27,32} The conductivity of asymmetric TiN is also comparable to block copolymer-derived porous TiN thin films.¹⁸

Magnetization Characterization.

Temperature-dependent magnetization measurements were conducted on a Quantum Design Physical Property Measurement System (PPMS) Vibrating Sample Magnetometer (VSM). A sample of the superconducting nitride after all heat treatments was placed in a polypropylene powder capsule and mounted in a brass half-tube on the VSM. The sample was zero-field cooled to 2.2 K, after which a field of 100 Oe was applied and the sample position determined by scanning for a negative magnetic moment. The moment was then measured while scanning temperature from 2.2 K to 5 K at 1 K min^{-1} , after which the sample was warmed to room temperature.

REFERENCES

1. Martinet, S. *Nanomaterials for rechargeable lithium batteries. NanoScience and Technology* (2016). doi:10.1007/978-3-319-32023-6_13
2. Sun, Y., Liu, N. & Cui, Y. Promises and challenges of nanomaterials for lithium-based rechargeable batteries. *Nature Energy* **1**, (2016).
3. Lin, T. *et al.* Nitrogen-doped mesoporous carbon of extraordinary capacitance for electrochemical energy storage. *Science (80-.)*. **350**, 1508–1513 (2015).
4. Miller, J. R. & Simon, P. Materials science: Electrochemical capacitors for energy management. *Science (80-.)*. **321**, 651–652 (2008).
5. Simon, P., Gogotsi, Y. & Dunn, B. Where do batteries end and supercapacitors begin? *Science* **343**, 1210–1211 (2014).
6. Rolison, D. R. *et al.* Multifunctional 3D nanoarchitectures for energy storage and conversion. *Chem. Soc. Rev.* **38**, 226–52 (2009).
7. Long, J. W., Dunn, B., Rolison, D. R. & White, H. S. Three-Dimensional Battery Architectures. *Chem. Rev.* **104**, 4463–4492 (2004).
8. Gogotsi, Y. & Simon, P. True performance metrics in electrochemical energy storage. *Science* **334**, 917–918 (2011).
9. Aricò, A. S., Bruce, P., Scrosati, B., Tarascon, J. M. & Van Schalkwijk, W. Nanostructured materials for advanced energy conversion and storage devices. *Nature Materials* **4**, 366–377 (2005).
10. Yang, P. D., Zhao, D. Y., Margolese, D. I., Chmelka, B. F. & Stucky, G. D. Generalized syntheses of large-pore mesoporous metal oxides with semicrystalline frameworks. *Nature* **396**, 152–155 (1998).

11. Zhao, D. *et al.* Triblock copolymer syntheses of mesoporous silica with periodic 50 to 300 angstrom pores. *Science* **279**, 548–52 (1998).
12. Gallagher, K. G. *et al.* Optimizing Areal Capacities through Understanding the Limitations of Lithium-Ion Electrodes. *J. Electrochem. Soc.* **163**, A138–A149 (2016).
13. Lee, J. *et al.* Direct access to thermally stable and highly crystalline mesoporous transition-metal oxides with uniform pores. *Nat. Mater.* **7**, 222–228 (2008).
14. Orilall, M. C. & Wiesner, U. Block copolymer based composition and morphology control in nanostructured hybrid materials for energy conversion and storage: solar cells, batteries, and fuel cells. *Chem. Soc. Rev.* **40**, 520–535 (2011).
15. Ulbricht, M. Advanced functional polymer membranes. *Polymer (Guildf)*. **47**, 2217–2262 (2006).
16. Peinemann, K. V., Abetz, V. & Simon, P. F. W. W. Asymmetric superstructure formed in a block copolymer via phase separation. *Nat. Mater.* **6**, 992–6 (2007).
17. Dorin, R. M. *et al.* Solution Small-Angle X-ray Scattering as a Screening and Predictive Tool in the Fabrication of Asymmetric Block Copolymer Membranes. *ACS Macro Lett.* **1**, 614–617 (2012).
18. Fritz, K. E., Beaucage, P. A., Matsuoka, F., Wiesner, U. & Suntivich, J. Mesoporous titanium and niobium nitrides as conductive and stable electrocatalyst supports in acid environments. *Chem. Commun.* **53**, 7250–7253 (2017).
19. Weng, C. C., Hsu, K. F. & Wei, K. H. Synthesis of arrayed, TiO₂ needlelike

- nanostructures via a polystyrene-block-poly(4-vinylpyridine) diblock copolymer template. *Chem. Mater.* **16**, 4080–4086 (2004).
20. Lou, Q., Chinthamanipeta, P. S. & Shipp, D. A. Mechanism of titania deposition into cylindrical poly(styrene- block -4 vinyl pyridine) block copolymer templates. *Langmuir* **27**, 15206–15212 (2011).
 21. Phillip, W. A. *et al.* Tuning structure and properties of graded triblock terpolymer-based mesoporous and hybrid films. *Nano Lett.* **11**, 2892–900 (2011).
 22. Werner, J. G., Hoheisel, T. N. & Wiesner, U. Synthesis and characterization of gyroidal mesoporous carbons and carbon monoliths with tunable ultralarge pore size. *ACS Nano* **8**, 731–43 (2014).
 23. Hesse, S. A., Werner, J. G. & Wiesner, U. One-pot synthesis of hierarchically macro- and mesoporous carbon materials with graded porosity. *ACS Macro Lett.* **4**, 477–482 (2015).
 24. Cromer, D. T. & Herrington, K. The Structures of Anatase and Rutile. *J. Am. Chem. Soc.* **77**, 4708–4709 (1955).
 25. Hardy, G. F. & Hulm, J. F. The Superconductivity of Some Transition Metal Compounds. *Phys. Rev.* **93**, 1004–1016 (1954).
 26. Kamiya, K., Nishijima, T. & Tanaka, K. Nitridation of the Sol–Gel-Derived Titanium Oxide Films by Heating in Ammonia Gas. *J. Am. Ceram. Soc.* **73**, 2750–2752 (1990).
 27. Robbins, S. W. *et al.* Block copolymer self-assembly-directed synthesis of mesoporous gyroidal superconductors. *Sci. Adv.* **2**, (2016).

28. Brauer, G. Nitrides, carbonitrides and oxynitrides of niobium. *J. Less-Common Met.* **2**, 131–137 (1960).
29. Werner, J. G., Rodríguez-Calero, G. G., Abruña, H. D. & Wiesner, U. Block copolymer derived 3-D interpenetrating multifunctional gyroidal nanohybrids for electrical energy storage. *Energy Environ. Sci.* **11**, 1261–1270 (2018).
30. Werner, J. G., Johnson, S. S., Vijay, V. & Wiesner, U. Carbon-sulfur composites from cylindrical and gyroidal mesoporous carbons with tunable properties in lithium-sulfur batteries. *Chem. Mater.* **27**, 3349–3357 (2015).
31. Baker, D. F. & Bragg, R. H. The electrical conductivity and Hall effect of glassy carbon. *J. Non. Cryst. Solids* **58**, 57–69 (1983).
32. Yang, M., Cui, Z. & Disalvo, F. J. Mesoporous titanium nitride supported Pt nanoparticles as high performance catalysts for methanol electrooxidation. *Phys. Chem. Chem. Phys.* **15**, 1088–1092 (2013).
33. Jang, E. S. *et al.* Asymmetric high-Tc superconducting gas separation membrane. *Chem. Mater.* **19**, 3840–3844 (2007).
34. Pessall, N., Gold, R. E. & Johansen, H. A. A study of superconductivity in interstitial compounds. *J. Phys. Chem. Solids* **29**, 19–38 (1968).
35. Münster, A. & Sagel, K. Über einige elektrische Eigenschaften von Titanitrid und Titancarbid. *Zeitschrift für Phys.* **144**, 139–151 (1956).
36. Meissner, W. & Franz, H. Messungen mit Hilfe von flüssigem Helium. IX. Supraleitfähigkeit von Carbiden and Nitriden. *Zeitschrift für Phys.* **65**, 30–54 (1930).
37. Meissner, W., Franz, H. & Westerhoff, H. Messungen mit Hilfe von flüssigem

- Helium. XVI - Untersuchungen über die Supraleitfähigkeit von Carbiden, Nitriden, Boriden und Siliciden. *Zeitschrift für Phys.* **75**, 521–530 (1932).
38. Choi, D. & Kumta, P. N. Synthesis and characterization of nanostructured niobium and molybdenum nitrides by a two-step transition metal halide approach. *J. Am. Ceram. Soc.* **94**, 2371–2378 (2011).
 39. Mefford, J. T., Hardin, W. G., Dai, S., Johnston, K. P. & Stevenson, K. J. Anion charge storage through oxygen intercalation in LaMnO₃ perovskite pseudocapacitor electrodes. *Nat. Mater.* **13**, 726–732 (2014).
 40. Brousse, T., Toupin, M. & Bélanger, D. A Hybrid Activated Carbon-Manganese Dioxide Capacitor using a Mild Aqueous Electrolyte. *J. Electrochem. Soc.* **151**, A614–A622 (2004).
 41. Lei, Z., Zhang, J. & Zhao, X. S. Ultrathin MnO₂ nanofibers grown on graphitic carbon spheres as high-performance asymmetric supercapacitor electrodes. *J. Mater. Chem.* **22**, 153–160 (2012).
 42. Sumboja, A., Foo, C. Y., Wang, X. & Lee, P. S. Large areal mass, flexible and free-standing reduced graphene oxide/manganese dioxide paper for asymmetric supercapacitor device. *Adv. Mater.* **25**, 2809–2815 (2013).
 43. Yu, Z., Duong, B., Abbitt, D. & Thomas, J. Highly ordered MnO₂ nanopillars for enhanced supercapacitor performance. *Adv. Mater.* **25**, 3302–3306 (2013).
 44. Hu, L. *et al.* Highly conductive paper for energy-storage devices. *Proc. Natl. Acad. Sci.* **106**, 21490–21494 (2009).
 45. Kaempgen, M., Chan, C. K., Ma, J., Cui, Y. & Gruner, G. Printable thin film supercapacitors using single-walled carbon nanotubes. *Nano Lett.* **9**, 1872–1876

- (2009).
46. Xu, Y. *et al.* Flexible solid-state supercapacitors based on three-dimensional graphene hydrogel films. *ACS Nano* **7**, 4042–4049 (2013).
 47. Yang, X., Cheng, C., Wang, Y., Qiu, L. & Li, D. Liquid-mediated dense integration of graphene materials for compact capacitive energy storage. *Science (80-.)*. **341**, 534–537 (2013).
 48. Lukatskaya, M. R. *et al.* Cation intercalation and high volumetric capacitance of two-dimensional titanium carbide. *Science (80-.)*. **341**, 1502–1505 (2013).
 49. Robbins, S. W., Sai, H., Disalvo, F. J., Gruner, S. M. & Wiesner, U. Monolithic gyroidal mesoporous mixed titanium-niobium nitrides. *ACS Nano* **8**, 8217–8223 (2014).
 50. Stefik, M. *et al.* Networked and chiral nanocomposites from ABC triblock terpolymer coassembly with transition metal oxide nanoparticles. *J. Mater. Chem.* **22**, 1078–1087 (2012).
 51. Allgaier, J., Poppe, A., Willner, L. & Richter, D. Synthesis and Characterization of Poly[1,4-isoprene- *b* -(ethylene oxide)] and Poly[ethylene- *co* -propylene- *b* -(ethylene oxide)] Block Copolymers. *Macromolecules* **30**, 1582–1586 (1997).
 52. Warren, S. C., Disalvo, F. J. & Wiesner, U. Nanoparticle-tuned assembly and disassembly of mesostructured silica hybrids. *Nat. Mater.* **6**, 156–161 (2007).
 53. Brunauer, S., Emmett, P. H. & Teller, E. Adsorption of Gases in Multimolecular Layers. *J. Am. Chem. Soc.* **60**, 309–319 (1938).
 54. Sing, K. S. W. *et al.* Reporting Physisorption Data for Gas/Solid Systems With Special Reference to the Determination of Surface Area and Porosity

- (Recommendations 1984). *Pure Appl. Chem.* **57**, 603–619 (1985).
55. Barrett, E. P., Joyner, L. G. & Halenda, P. P. The Determination of Pore Volume and Area Distributions in Porous Substances. I. Computations from Nitrogen Isotherms. *J. Am. Chem. Soc.* **73**, 373–380 (1951).
 56. Zhernenkov, M., Canestrari, N., Chubar, O. & DiMasi, E. Soft matter interfaces beamline at NSLS-II: geometrical ray-tracing vs. wavefront propagation simulations. in *Advances in Computational Methods for X-Ray Optics III* (2014). doi:10.1117/12.2060889
 57. Ilavsky, J. Nika: Software for two-dimensional data reduction. *J. Appl. Crystallogr.* **45**, 324–328 (2012).
 58. Ilavsky, J. & Jemian, P. R. Irena: Tool suite for modeling and analysis of small-angle scattering. *J. Appl. Crystallogr.* **42**, 347–353 (2009).

CHAPTER 5

CONCLUSION

The topic of this dissertation has been the synthesis, characterization, as well as performance of asymmetric porous materials derived from the SNIPS process – block copolymer (BCP) self-assembly (SA) and non-solvent induced phase separation (NIPS).

In the second and third chapters of this dissertation, I explored the early formation stages of the asymmetric hybrids using a combination of scattering and imaging techniques. I showed that variations in the solution preparation methods led to vastly different self-assembly behavior in solution. Further characterization of the hybrids and final asymmetric inorganic structures elucidated different, yet tunable properties with respect to both the top surface ordering and substructure porosity profile of the resulting membranes.

In the fourth chapter, asymmetric carbon and titanium nitrides were synthesized, characterized, and tested as electrochemical double-layer capacitors (EDLCs). While these materials were not specifically optimized for this application, interestingly they already possessed better than state-of-the-art power densities and competitive energy densities. These first encouraging results of asymmetric carbon and nitride structures in an energy application suggest that materials with asymmetric rather than homogeneous porosity may be advantageous not only in separations, but also in energy conversion and storage as well as catalysis applications.

Further studies into these asymmetric materials could lead to an improved understanding of their formation and resulting properties and performance. Fundamental studies into the early formation of these materials could prove useful to tuning properties.

Some efforts are currently underway involving neutron scattering and nuclear magnetic resonance spectroscopy, in order to probe the early formation mechanisms.¹ Fundamental modeling could also aid in understanding transport in these porous structures.

By exploring the characteristics resulting from the SNIPS process, materials properties could be tuned. As such, similar to their polymeric counterparts, it is expected that tailoring membrane cross-sections between sponge and finger-like structures in the resulting asymmetric inorganic materials could lead to tunable properties.² Similarly, changing the membrane thickness could affect the material performance.

Further studies into the chemistry of the materials could prove useful in tuning their properties. For example, it has previously been shown that activated carbon has a much higher surface area than its unactivated counterpart.³ This could thus lead to improved energy density. Nitrogen-doped carbons or incorporation of active catalysts such as metal nanoparticles (*e.g.* platinum) could make these materials viable for other catalytic applications. Studies into the nitride formation pathway have shown that the pathway by which the nitride is obtained can lead to different crystallinity in the final materials and result in performance variations.⁴ Further studies, especially into the nitriding steps are therefore expected to also lead to better control of the nitride crystallinity and composition. A technique, such as the combined assembly by soft and hard (CASH) chemistries, could aid in controlling the crystal overgrowth that resulted from a second heat-treatment of the titanium nitride.⁵

Not only can these materials themselves potentially find use in catalysis, energy conversion and storage, and separations, but they could potentially also be used as a

support to deposit materials, such as in the case of a three-dimensional (3D) integrate nanobattery as reported for a different morphology by Werner *et al.*^{3,6-8} For such applications, in particular, handling could be improved by casting or adhering the membranes onto a wafer or substrate. Initial experiments have shown promise for this approach.

The knowledge obtained from studying these first asymmetric inorganic materials can be used to further expand the library of functional materials that can undergo the SNIPS process thereby expanding their properties away from those resulting from more homogeneous structures. We expect that the advantages of these materials (high porosity and pore accessibility) as well as advantages associated with the NIPS-based fabrication process (tunability and roll-to-roll scalability as well as compatibility of the process with various chemistries) will allow the materials to find use in catalysis, energy conversion and storage, and separations.

REFERENCES

1. Hesse, S. A. *et al.* *Properties of ABC Triblock Terpolymer Solutions*. In Preparation.
2. Zhang, Q., Li, Y. M., Gu, Y., Dorin, R. M. & Wiesner, U. Tuning substructure and properties of supported asymmetric triblock terpolymer membranes. *Polymer (Guildf)*. **107**, 398–405 (2016).
3. Werner, J. G., Johnson, S. S., Vijay, V. & Wiesner, U. Carbon-sulfur composites from cylindrical and gyroidal mesoporous carbons with tunable properties in lithium-sulfur batteries. *Chem. Mater.* **27**, 3349–3357 (2015).
4. Hesse, S. A. *et al.* *Asymmetric Porous Oxides and Nitrides using Block Copolymers as Structure-Directing Agents for TiO₂ Nanoparticles*. (2019). In Preparation.
5. Lee, J. *et al.* Direct access to thermally stable and highly crystalline mesoporous transition-metal oxides with uniform pores. *Nat. Mater.* **7**, 222–228 (2008).
6. Werner, J. G., Scherer, M. R. J., Steiner, U. & Wiesner, U. Gyroidal mesoporous multifunctional nanocomposites via atomic layer deposition. *Nanoscale* **6**, 8736–8742 (2014).
7. Werner, J. G., Rodríguez-Calero, G. G., Abruña, H. D. & Wiesner, U. Block copolymer derived 3-D interpenetrating multifunctional gyroidal nanohybrids for electrical energy storage. *Energy Environ. Sci.* **11**, 1261–1270 (2018).
8. Werner, J. G., Rodríguez-calero, G. G., Abruña, H. D. & Wiesner, U. Block Copolymer Derived Multifunctional Gyroidal Monoliths for 3-D Electrical Energy

Storage Applications. *arXiv:1706.02134* [*physics.chem-ph*] (2017).
doi:10.1039/C7EE03571C